

USING IN SITU NEUTRON AND GAMMA-RAY SPECTROSCOPY
TO CHARACTERIZE ASTEROIDS

JULIA GATES BODNARIK

Dissertation under the direction of Professor Keivan G. Stassun and Dr. Ann M. Parsons

Asteroids are remnants of the formation of the Solar System and provide insight into its formation, evolution and how life may have begun. An important issue is determining which meteorite composition is representative of which asteroid class and type. *In situ* composition measurements would be one way to resolve this issue.

This dissertation contributes toward developing and testing of a neutron/gamma-ray spaceflight instrument for subsurface regolith composition measurements for landed asteroid missions. The Probing *In situ* with Neutrons and Gamma rays (PING) instrument was tested at an outdoor test facility on well-characterized granite, basalt, and asteroid simulant monuments with a variety of different layering configurations. PING utilizes a 14 MeV pulsed neutron generator to probe the subsurface, and uses neutron and gamma-ray spectrometers to detect the resulting moderated neutrons and gamma rays. The neutron and gamma-ray energy spectra are used to determine bulk properties and the material composition.

We compared our experimental spectra both to Monte Carlo simulations and to independently verified elemental assays in order to establish a benchmarked Monte Carlo

model. This comparison shows that PING can quantitatively determine bulk asteroid properties, but more sophisticated MCNPX models are needed to properly model PING experiments. The benchmarked Monte Carlo model can then simulate PING measurements on asteroids, which could be used to determine bulk asteroid properties, differentiate between asteroid types, and thus strengthen their connection to meteorite compositions.

This research firmly establishes that PING can obtain important geochemical information on asteroids from neutron transport and elemental analysis. A future asteroid mission with PING will have substantially increased science return providing a direct subsurface regolith description, without needing to drill or disrupt the surface. We have demonstrated that compositions for specific asteroid types can be fabricated in large volume structures on Earth permitting experiments, with a benchmarked Monte Carlo program, to predict mission responses to optimize the science return prior to launch.

Approved:

Keivan G. Stassun

Ann M. Parsons

USING IN SITU NEUTRON AND GAMMA-RAY SPECTROSCOPY TO
CHARACTERIZE AND DIFFERENTIATE ASTEROIDS

by

Julia Gates Bodnarik

Dissertation

Submitted to the Faculty of the
Graduate School of Vanderbilt University
in partial fulfillment of the requirements

for the degree of

DOCTOR OF PHILOSOPHY

in

Physics

May, 2013

Nashville, Tennessee

Approved:

Keivan G. Stassun

Ann M. Parsons

Jeffrey S. Schweitzer

Arnold Burger

Kelly Holley-Bockelmann

David J. Ernst

Copyright © 2013 by Julia Gates Bodnarik
All Rights Reserved

To my amazing parents and brother, Martha, Andy and Michael, providing me with the will, strength, perseverance and support to see this dissertation through to its completion

and

To my family, friends, mentors, colleagues, and mentees for their insight, mentorship and infinite support.

ACKNOWLEDGEMENTS

This work would not have been possible without the financial support of the VIDA fellowship, the NASA Goddard Space Flight Center Co-OP program, the NASA PIDDP program, the NASA IRAD program, the Tennessee Space Grant, and the National Science Foundation. I am especially indebted to Dr. Arnold Burger, Dr. Keivan Stassun, Dr. Ann Parsons, Dr. Jeffrey Schweitzer, and Dr. Jason Dworkin, who have been supportive of my career goals and who have worked actively to provide me with the protected academic and professional time to pursue those goals.

I am grateful to everyone whom I have had the pleasure to work with during this and other related projects, especially my NASA Goddard Space Flight Center Astrochemistry group members including, Suzanne Nowicki, Dr. Jacob Trombka, Dr. Ann Parsons, Dr. Jeffrey Schweitzer, Dr. Min Namkung, Dr. Richard Starr, Dr. Larry Evans, Dr. Timothy McClanahan, Dr. Lucy Lim, Samuel Floyd, Dr. Joseph Nuth, Dr. Jason Dworkin, and all of the interns I worked with and mentored including, Jessica Marbourgh, Dan Burger, Robert Forsythe, Amber Keske, Robert Jenkins, and Rose Perea, and all of my graduate student cohorts at Fisk and Vanderbilt University including, Ebonee Walker, Deatrick Foster, Desmond Campbell, and Brittany Kamai. Each member of my Dissertation Committee has provided me extensive personal and professional guidance and taught me a great deal about scientific research and life. I would especially like to thank Dr. Ann Parsons, Dr. Jeffrey Schweitzer, and Dr. Keivan Stassun. As my teachers, mentors, and friends, you have all taught me more than I could ever give any of you credit for here. You have all shown me through your actions what a

good scientist and person should be as well as provided me with a work environment in which I have been able to flourish both professionally and personally.

No one has been more important in my life to me in the pursuit of this project than my family. I would like to thank my ultimate role models, my parents and brother, whose love, guidance and strength are with me in whatever I chose to pursue. I would also like to thank my cousin and aunt, Kara and Lillian Kozla, who have always been there to cheer me up and help me see the forest through the trees.

TABLE OF CONTENTS

DEDICATION	iii
ACKNOWLEDGMENTS	iv
LIST OF TABLES	viii
LIST OF FIGURES	x
LIST OF ABBREVIATIONS.....	xiv
I. INTRODUCTION	1
What do we know about asteroids?	4
What is the state of the asteroid to meteorite connection?.....	4
What techniques have been used?	6
What do we want to know about asteroids and how can we get this information?.....	7
What do we not know about asteroids	7
What are the advantages of <i>in situ</i> vs. orbital neutron/gamma-ray measurements.....	8
What possible <i>in situ</i> measurement techniques can be used to obtain the C-complex asteroid bulk geochemistry?.....	10
<i>In situ</i> measurements.....	10
Neutron transport	13
Gamma-ray spectroscopy.....	15
Neutron data analysis	16
Studying the subsurface elemental composition of asteroids using PING	17
Testing PING on earth	17
Testing PING on an asteroid simulant.....	18
II. EXPERIMENT DESCRIPTION.....	20
Design of the Goddard Geophysical and Astronomical Observatory (GGAO) neutron/gamma-ray instrumentation test facility	20
Neutron/gamma-ray instrumentation test facility	20
Design of physical rock configurations	23
Meter-sized asteroid analog	24
Experimental Rock Configurations.....	27
PING experimental equipment set-up on rock configurations	29

PING experimental equipment description.....	30
Pulsed neutron generator.....	30
Acquisition electronics, gamma-ray and neutron detectors.....	32
Gamma-ray detector.....	32
Neutron detectors.....	34
Lynx DSA electronics and acquisition software.....	36
III. DATA ANALYSIS AND MCNPX CALCULATIONS	39
Experimental data analysis	39
Gamma-ray data analysis.....	40
The TLIST data acquisition technique.....	40
TLIST data analysis technique.....	42
Improved gamma-ray measurement precision.....	46
Identifying and removing sources of systematic error using TLIST data	50
Energy calibrating spectra using Igor Pro 6.2 software.....	53
Putting energy calibrated spectra on one energy scale using Igor Pro 6.2	66
Gamma-ray peak fitting using the fit gauss with tail Igor Pro function	68
Neutron data analysis.....	70
MCNPX data analysis.....	72
Geometry and VISED.....	73
Configurations modeled and approximations that were made.....	73
Analyzing MCNPX output	75
IV. RESULTS AND INTERPRETATION	76
Results and Interpretation	77
Gamma ray.....	77
Neutron	90
V. CONCLUSION.....	97
REFERENCES	100
APPENDIX I	105
APPENDIX II.....	107
APPENDIX III.....	124

LIST OF TABLES

TABLE.....	PAGE
1. Material Configurations for Each PING Experiment.	28
2. γ -ray lines to analyze for inelastic γ -ray spectra time window optimization.....	44
3. HPGe gamma-ray line intensities (I_γ) and uncertainties (σ) during different time windows for a 6.33-hr PING acquisition on the bare Columbia River basalt monument. For the 1779 and 6129 keV activation peaks, the half-lives are 2.3 min and 7.1 s, respectively. Note the Activation column includes data from all times that the neutron pulse was off. Neutron thermalization begins even before the fast neutron pulse turns off at 100 μ s and it reaches a peak at approximately 100 μ s and then slowly decays, therefore the $^1\text{H}(n,\gamma)$ 2223 keV gamma-ray line appears in both the inelastic scattering and thermal neutron capture windows due to the time windows selected for these processes.	48
4. Fast neutron induced count rate and uncertainty for the 6129 keV $^{16}\text{O}(n,n'\gamma)$ gamma-ray peak for ten time slices during the PNG pulse.....	51
5. Energy Calibrations for Summed Time-Sliced Granite, Basalt, and Asteroid Simulant Configurations Data using HPGe Bare and Boron-Wrapped Detector.	67
6. Granite, Basalt, CII chondrite meteorite element concentrations.	78
7. Gamma-ray line intensities and uncertainties for the PING granite monument data, with the HPGe detector wrapped in a boronated-rubber cap, for different timing windows during the PNG pulse period (total acquisition live time = 16.21 hrs). The “*” symbol means that it is the excited state of the isotope, i.e. $^{25}\text{Mg}^*$ means that it is the excited state of ^{25}Mg	81
8. Gamma-ray line intensities and uncertainties for the basalt monument data, with the HPGe detector wrapped in a boronated-rubber cap, for different timing windows during the PNG pulse period (total acquisition live time = 15.23 hrs). The “*” symbol means that it is the excited state of the isotope, i.e. $^{25}\text{Mg}^*$ means that it is the excited state of ^{25}Mg	82
9. Gamma-ray line intensities and uncertainties for the asteroid simulant data, with the HPGe detector wrapped in a boronated-rubber cap, for different timing windows during the PNG pulse period (total acquisition live time = 46.15 hrs) for the asteroid simulant experiment. The “*” symbol means that it is the excited state of the isotope, i.e. $^{25}\text{Mg}^*$ means that it is the excited state of ^{25}Mg	83

LIST OF TABLES (CONT.)

TABLE.....	PAGE
10. Gamma-ray line cleaning results and uncertainties for the granite monument.	84
11. Gamma-ray line cleaning results and uncertainties for the basalt monument.	84
12. Gamma-ray line cleaning results and uncertainties for the asteroid simulant.	85
13. Gamma-ray element/Si experimental and MCNPX ratios for the granite.	86
14. Gamma-ray element/Si experimental and MCNPX ratios for the basalt.	87
15. Gamma-ray element/Si experimental and MCNPX ratios for the asteroid simulant.....	89
16. The calculated macroscopic thermal neutron absorption cross-section calculations for the granite monument.	93
17. The calculated macroscopic thermal neutron absorption cross-section calculations for the basalt monument.	94
18. The calculated macroscopic thermal neutron absorption cross-section calculations for the asteroid simulant.	95
19. Granite, basalt and asteroid simulant calculated and experimental macroscopic thermal neutron absorption comparison. Note: the asteroid simulant calculated value is based upon CII carbonaceous chondrite calculations.....	96
20. ActLabs columbia river basalt elemental assay.	105
21. ActLabs concord grey granite elemental assay.	106
22. Raw TLIST gamma-ray, thermal and epithermal neutron data collection totals for data acquired with PING on the 10 experimental rock configurations. He1 and He2 refer to the ³ He thermal and epithermal neutron detectors. UT stands for the detectors borrowed from the University of Tennessee and Navy stands for the detector borrowed through Stan Hunter from the Navy.	107

LIST OF FIGURES

FIGURE	PAGE
1. Asteroid taxonomic classifications.	3
2. An illustration of the different types of space-weathering processes that alter the surface geochemistry of asteroids.	4
3. Illustration of PING mounted on a rover showing how it can be used to determine the bulk elemental composition over a 1 m ² surface area and down to 50 cm below the surface of an asteroid.	12
4. PING takes advantage of four different gamma ray-producing processes: inelastic scattering, neutron capture, neutron activation and natural radioactivity to determine the elemental abundance of the planetary material.	14
5. Aerial view of GGAO. This schematic of the outdoor gamma ray and neutron instrumentation testing facility shows the operations control building as well as the 47 m diameter safety perimeter surrounding the two existing 1.8 m x 1.8 m x 0.9 m granite and basalt monuments.	21
6. A drawing of the soil profile performed by Gunther Kletetschka and Julia Bodnarik on their shoveled out 0.9 m x 0.9 m x 0.6 m meter pit in the middle of the field at GGAO with 2.1 m tall grass on July 28, 2008.	22
7. Image of the test facility with the operations building (left), the basalt monument covered with the homogenous C-type asteroid layering simulant (right), and granite monument (far-right).	23
8. Image of PING components on the C-type asteroid simulant.	26
9. Graphs of the MCNPX computer modeling results of the epithermal and thermal neutron flux distribution as a function of neutron penetration depth for the C-type asteroid (blue) and the basalt layering asteroid simulant (red).	27
10. Drawing of the spacing of the PING components using for each experimental configuration.	29
11. A schematic of a PNG.	31
12. A picture of a Cockroft Walton neutron generator.	32

LIST OF FIGURES (CONT.)

FIGURE	PAGE
13. Schematic of the cross-section perpendicular to the cylindrical axis of the n-type HPGe detector crystal.	33
14. Schematic of a ³ He neutron gas detector.	36
15. Lynx DSA Images of a) the front and, b) the back (showing connection ports for HPGe) of the acquisition system.	37
16. Timing Windows and Sample Spectra. a) Placement of timing windows relative to each PNG pulse. b) Examples of different spectral shapes seen in different timing windows.	41
17. Spectra from Different Time Windows. Gamma-ray spectra from a 6.33-hr acquisition using a HPGe detector on top of Columbia River basalt.	43
18. Figure 18. Spectral Feature and Time Distribution. a) A portion of the non-time sliced 6.33-hr gamma ray energy histogram from PING data taken on the bare basalt monument. b) Time histogram showing how one can get better precision on the net peak area of each line, shown in Table 2, by analyzing their respective energy histograms during different time slices during the PNG pulse period.	46
19. Image of the Data and Load Waves menu files in Igor.	54
20. Image of the Load General Text window.	55
21. Image of the Loading General Text window.	55
22. Image of the Gamma menu.	56
23. Image of the Fit Gauss With Tail window.	57
24. Fit Gauss With Tail gamma-ray spectrum window.	58
25. Add Peak Type window.	58
26. Peak parameter values for the new peak added in the Fit Gauss With Tail panel.	59
27. Selecting the Fit All button the Fit Gauss With Tail spectrum graph.	60
28. Setting all of the peak parameters to Fixed.	60

LIST OF FIGURES (CONT.)

FIGURE	PAGE
29. Image of the Compact Parameter Report window.	61
30. Example of a MS Excel file with the copied report.	61
31. Image of Windows panel in Igor.	62
32. Image of the gamma-ray energy list in the new table.	62
33. Image of the Rename Objects window in Igor.	63
34. Image of the gamma-ray channel list in the new table.	63
35. Image of the New Graph panel.	64
36. Image of the Analysis menu.	64
37. Image of the Curve Fitting panel.	65
38. Image of the Curve Fitting graph.	65
39. Fitting four peaks on top of a Ge sawtooth peak. Note the better baseline fit (aqua blue lines) due to the exclusion of peaks (lime green) that are not currently being fit in the peak fit window (purple lines).	69
40. a) (Right) A triple-peak fit with an appropriate baseline. b) (Left) Zoomed in view of the Igor peak fitting report (outlined in red) showing that the Peak 2 area fit (outlined in aqua blue) has a large error and requires adjustments to improve the fit's accuracy.	69
41. Cartoon illustrating the comparison of the average macroscopic thermal neutron absorption cross-sections from experimental and calculated data.	71
42. Equations used to calculate the theoretical average macroscopic thermal neutron absorption cross-section for bulk materials.	71
43. Aerial view of MCNPX geometry and space of HPGe crystal and PNG source point on top of the granite, basalt, and asteroid layering simulants configurations.	74
44. Experimental thermal neutron dieaway results and fit for the granite.	91

LIST OF FIGURES (CONT.)

FIGURE	PAGE
45. Experimental thermal neutron dieaway results and fit for the basalt.	92
46. Experimental thermal neutron dieaway results and fit for the asteroid simulant	92
47. Image of the PING instrument prototype on top of the Concord Grey Granite monument.	120
48. Image of the PING instrument prototype on top of the Columbia River Basalt monuement taken on 08/21/2012.	121
49. Schematic of the Columbia River Basalt monument dimensions.	121
50. Sketch of the PING equipment spacing used for all experiments.	122
51. Notes from the basalt monument PING experiment.	122
52. Image of the PING instrument on the layered asteroid simulant.....	123

LIST OF ABBREVIATIONS

ACTLabs	Activation Laboratories located in Ontario, Canada
ASCII	American Standard Code for Information Interchange
C-complex	Carbonaceous asteroid spectral type C
CI1	Ivuna-like carbonaceous chondrite meteorite
CM	Mighei-like carbonaceous chondrite meteorite
CNF	Canberra file format
C-type	Carbonaceous asteroid spectral type C (a.k.a. C-complex)
DAN	Dynamic Albedo of Neutrons experiment on MSL
D-D	Deuterium-Deuterium
DSA	Digital Signal Analyzer
D-T	Deuterium-Tritium
FWHM	Full Width at Half Maximum
FWTM	Full Width at Tenth Maximum
GGAO	Goddards Geophysical and Astronomical Observatory
GRC	Galactic Cosmic Ray
GRS	Gamma-Ray Spectroscopy
GSFC	Goddard Space Flight Center
HDPE	High-Density PolyEthylene
HPGe	High Purity Germanium detector
LRO	Lunar Reconnaissance Orbiter
MESSENGER	Mercury Surface Space Environment GEOchemistry, and Ranging
MCNP	Monte Carlo N-Particle computer code
MCNPX	Monte Carlo N-Particle eXtended computer code
MPI	Message Passing Interface
MSL	Mars Science Laboratory
NASA	National Aeronautics and Space Administration
NCCS	NASA Center for Climate Simulation
NEAR	Near Earth Asteroid Rendezvous (a.k.a. NEAR-Shoemaker)
NEAR-Shoemaker	NASA Near Earth Asteroid Rendezvous – Shoemaker mission
NIR	Near Infrared light
NS	Neutron Spectroscopy
PHA	Pulse Height Analysis
PING	Probing <i>In situ</i> with Neutrons and Gamma rays
PNG	Pulsed Neutron Generator
PTC	Princeton Technology Center
Q-value	a difference in energies of parent and daughter nuclides
TLIST	Time-stamped LIST mode
UV	Ultraviolet light
VIS	Visible light
VISED	Visual Editor interactive graphical user interface tool for MCNPX
XRS	X-Ray Spectroscopy

CHAPTER I

INTRODUCTION

Asteroids are remnants from the formation of the Solar System about 4.6 billion years ago and thus contain the elemental building blocks from which the planets were formed. Studying the organic and inorganic geochemistry of these ancient bodies can provide a window into the formation and evolution of the planets and the origin of life itself. Ongoing geochemical studies of primitive asteroids have been a critical contributing factor governing present models of planetary formation and solar system evolution. Carbonaceous asteroids (spectral type C or C-complex) are of particular scientific interest since they are a possible source of Earth forming planetesimals and contain volatiles, water, and organic materials that could be biogenic precursors. This evidence primarily comes from two sources including carbonaceous chondrite meteoritic studies and telescopic observations of C-complex asteroids. However, these sources reflect observations from widely contrasting spatial scales presently yielding a void in the continuum of microscopic to macroscopic evidence. The link between the mineralogy and elemental composition of carbonaceous chondrite meteorites and C-complex asteroids is tenuous and unclear since one is comparing the measured composition of the bulk of these meteorites with micron-thick surface composition measurements of these asteroids and the asteroid surface measurements may not be representative of the bulk composition of the C-complex asteroid. Therefore it is very difficult to determine which

meteorite came from which type of asteroid, requiring deeper sensing bulk measurement techniques to discern the bulk composition and nature of C-complex asteroids.

The main source of elemental composition information for C-complex asteroids is from their optical, Ultraviolet (UV), Visible (VIS), Near Infrared (NIR) and Infrared (IR) properties, which include their spectral reflectance characteristics, albedo, polarization, and the comparison of optical spectroscopy with meteorite groups corresponding to asteroids of every spectral type. However, these spectral reflectance measurements, used for asteroid taxonomy, are not particularly informative due to the lack of strong spectral features. Figure 1 shows the asteroid taxonomy classifications, demonstrating our minimal understanding of asteroids from UV, VIS and IR measurements.

With two exceptions[1],[2] , there is no direct link between meteorites and their parent body asteroids. For example, a given meteorite may be determined to be from a C-complex family of asteroids, but we don't know which asteroid taxonomic type it belongs to. Finally, UV, VIS, and IR measurements are limited to probing the first few microns of the surface of asteroids. However, we know that these top microns are strongly space-weathered, from solar wind exposure, micrometeorites, etc., and are substantially different from the bulk material, as seen in Figure 2. Consequently, these sources of information reflect observations from widely contrasting spatial scales, a lack of *in situ* measurement confirmation, and require deeper sensing techniques to discern the bulk nature of these asteroids.

Given our limited understanding of asteroids, there is much that we need to know about them. We still need to understand asteroid orbits, the difference between the space-weathered surface and pristine subsurface chemistry of asteroids, the pristine organic and

inorganic composition and distribution of asteroids on an atomic and molecular level, and the internal structure density and porosity of asteroids that tells us about their impact and accretion history. In particular, making *in situ* bulk surface and subsurface elemental composition and water-ice depth measurements would solidify the connection between C-complex asteroids to carbonaceous chondrite meteorites, leading to a greater understanding of how the planets were formed.

ASTEROID TAXONOMIC CLASSIFICATIONS

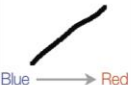
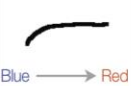
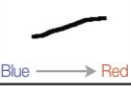
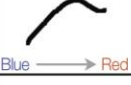

Major Taxonomic Types	Reflectance Spectrum (0.4-0.9 μm)	Spectral Features	Visible Albedo	Suspected Composition
D (D,T)		Relatively featureless spectrum Steep red slope	0.02-0.06	Primitive carbonaceous Organic-rich compounds Hydrated minerals
C (C,B,F,G)		Slight bluish to slight reddish slope Shallow to deep absorption blueward of 0.5 μm Hydrated asteroids with absorption at 0.7 and 3.0 μm	0.03-0.10	Hydrated minerals Silicates Organics
X (E,M,P)		Slightly reddish spectrum E: absorption features at 0.5 and 0.6 μm	E: 0.18-0.40 M: 0.10-0.18 P: 0.03-0.10	E: Enstatite-rich M: metallic, Nickel-Iron P: Carbonaceous, Organics
S (S,Q,A,K,L)		Moderately steep red slope ($\lambda < 0.7 \mu\text{m}$) Shallow to deep absorption at 1.0 and 2.0 μm	0.10-0.22	Stony composition Magnesium Iron silicates
V		Moderate to steep red slope ($\lambda < 0.7 \mu\text{m}$) Very deep absorption at 1.0 μm	0.20-0.60	Volcanic basalts Plutonic rocks

Figure 1. Asteroid taxonomic classifications[3].

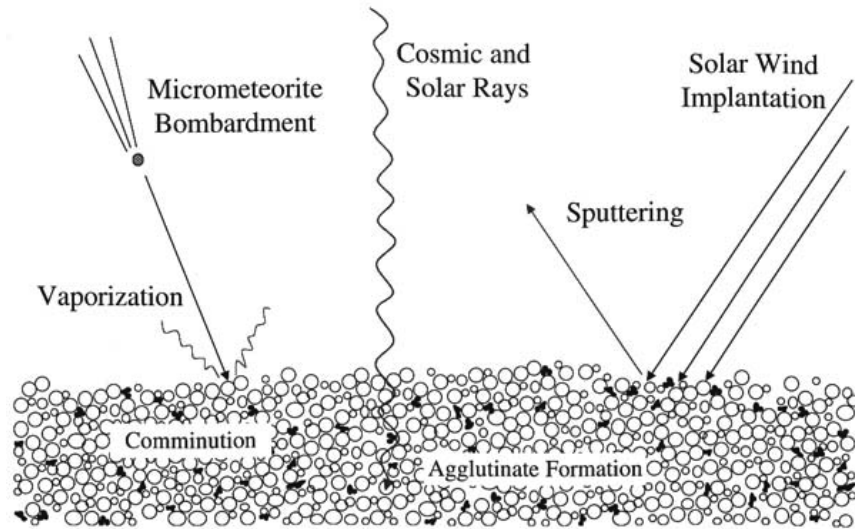


Figure 2. An illustration of the different types of space-weathering processes that alter the surface geochemistry of asteroids[4].

What Do We Know About Asteroids?

What is the State of the Asteroid to Meteorite Connection?

Carbonaceous chondrites, the most primitive and unaltered type of meteorites known, have an elemental composition that is likely similar to that of the nebula from which the Solar System formed. Carbonaceous chondrites are thus of particular interest to the scientific community since they are a possible source of Earth-forming planetesimals[5] and contain volatiles, water, and organic materials that could be biogenic precursors. Planetesimals formed in the outer portions of the asteroid main belt have been advocated by some workers as the major source of Earth's present water inventory[6], based in part on the similarity in isotopic composition between the hydrogen in the Earth's oceans and in the water in these carbonaceous chondrites.

Matching these primitive meteorites to their asteroid parent bodies is thus very important to the understanding of the origin and evolution of the planets in our solar system.

Currently, the best candidates for the parent bodies of carbonaceous chondrites are C-complex asteroids[7],[8], assigned by the Bus-DeMeo asteroid classification taxonomy[9],[10]. Unfortunately, VIS and NIR spectroscopy of C-complex asteroids provides limited compositional information, since their spectra are relatively featureless and the emission is very weak in this wavelength band. Perhaps the strongest evidence for a compositional relationship between C-complex asteroids and carbonaceous chondrites comes from reflectance spectroscopy of the OH absorption features in the 2.7-3.5 micron region[11],[12],[13]. Most, although not all, C-complex asteroids have a substantial water-of-hydration feature that is similar in spectral shape to that found in the spectra of CM (Mighei-like) carbonaceous chondrites and attributable to bound OH in phyllosilicates.

Ground-based spectroscopy in the 3-micron region has also recently provided evidence for water ice and organics on the surface of asteroid 24 Themis[14],[15]. Since the surface of this asteroid is too warm for ice to be stable on geologic time scales, the observed ice must have formed, been exposed or delivered very recently. Since ice is expected to be stable a few meters to a few tens of meters below the surface of 24 Themis[16], such an ice layer may serve as a reservoir, replenishing the exposed ice through slow sublimation and re-condensation on the surface and near-subsurface, as suggested by theoretical models of the main-belt comet 133P/Elst-Pizarro[17].

These recent observations coupled with ground-based meteorite analysis suggest that our current understanding of C-complex asteroids is very limited. Understanding

their elemental composition is a key component to understanding their formation and evolution, and can also provide information that will help scientists better understand the origin, formation and evolution of our Solar System, and possibly the biogenic precursors that may have sparked the life on Earth. Therefore a technique that is capable of making bulk surface and subsurface elemental composition and water-ice depth measurements would not only be well suited to testing this hypothesis, by evaluating the abundance and composition of ice and other volatiles in the near subsurface, but we can measure the properties of the meteorites on Earth to strengthen the connection between C-complex asteroids and carbonaceous chondrites, leading to a greater understanding of how the planets were formed, since asteroids are the most primitive bodies in the Solar System and strengthening and studying the meteorite to asteroid composition connection would then lead to understanding of the elements and materials present during the formation of the Solar System.

What Techniques Have Been Used?

Most of the research concerning the geochemistry of C-complex asteroids has been limited to either laboratory meteorite analog analysis or *in situ* and space-based remote sensing using VIS, NIR, IR, X-ray (XRS) and gamma-ray spectroscopy (GRS)[18],[19]. VIS, NIR, IR, and XRS measurements only probe a few microns to a few millimeters deep to reveal the surface geochemistry of an asteroid. However, space weather processes (Figure 2), as verified by laboratory measurements, significantly alter the chemistry of the surface materials so that they are not representative of the bulk material. In addition, laboratory geochemistry composition measurements of small-scale

C-complex meteorite analogs may not be representative of the overall bulk composition of C-complex asteroids as seen from analysis of the Almahata Sitta meteorites[1].

Passive remote-sensing orbital GRS, and/or neutron spectroscopy (NS) measurements can be used to probe the subsurface of asteroids to tens of centimeters below the surface and can yield information such as the overall bulk geochemistry and presence of hydrogen. However, orbital gamma-ray and neutron instruments depend on the Galactic Cosmic Ray (GCR) particle flux as the excitation source and have a spatial resolution proportional to the altitude of the spacecraft above the surface of the object being probed. Thus, remote sensing GRS and/or NS orbital and close-fly-by missions (e.g. Lunar Prospector[20], Mars Odyssey[21],[22], Dawn[23], MESSENGER[24], NEAR[25], and LRO[26],[27]) typically require long observation times (on the order of months to years), since they rely on GCR interactions with the regolith. Consequently, both the orbiting spacecraft's distance to the planet and the GCR flux greatly affect the probability of detecting gamma rays and neutrons emanating from the surface.

What Do We Want to Know About Asteroids and How Can We Get the Information?

What Do We Not Know About Asteroids?

The laundry list of what is not known about asteroids is lengthy. As mentioned previously, there is current lack of information on multiple spatial and depth scales that greatly hinder our understanding of primitive asteroids. To strengthen the connection between the geochemistry of carbonaceous meteorites to C-type asteroid parent bodies, as well as test current and future theories about subsurface H reservoirs, space weathering

effects, solar system formation and evolution, and possibly the origin of life, it is necessary to obtain *in situ* subsurface bulk elemental composition information about these asteroids to infer their subsurface mineralogy and compare it with other observations to create a more detailed picture that will aid in discerning the nature of these objects.

What are the Advantages of In Situ vs. Orbital Neutron/Gamma-Ray Measurements?

The key differences between ground-based *in situ* and orbital neutron/gamma-ray measurements are their excitation source and their spatial resolution. *In situ* neutron/gamma-ray instrumentation can utilize a pulsed neutron generator source, while orbital neutron/gamma-ray instruments utilize cosmic rays. In addition, the spatial resolution (or radius of the area probed) for *in situ* measurements is 1 m in radius as compared to orbital measurement spatial resolutions, proportional to the altitude of the spacecraft above the surface of the object being probed, on the order hundreds of kilometers in diameter.

The advantages of using a Pulsed Neutron Generator (PNG) on the surface are: 1) a known mono-energetic 14-MeV neutron source; 2) a flux of neutrons much greater than available from GCRs; and 3) the pulsed nature of the neutron flux. PNGs are superior to other neutron sources such as cosmic rays and radionuclides[28] for the excitation of subsurface materials. PNGs can produce neutron fluxes several orders of magnitude greater than that from cosmic rays and, unlike cosmic rays or radionuclides, provide a monoenergetic neutron source that makes measurements easier to model and interpret.

Most importantly, pulsing the neutrons permits discrimination between gamma-

rays produced promptly by inelastic scattering of the fast neutrons (observed during the neutron generator pulse), gamma-rays produced by thermal neutron capture (observed during the interpulse period), and gamma-rays from delayed activation and natural radioactivity (observed towards the end of an interpulse period), thus reducing background and line interference in these three separate spectra. In addition, a pulsed neutron source also allows for epithermal and thermal neutron die-away measurements where the build up and decay of the epithermal neutron signal during and immediately following the neutron pulse may be used to infer the hydrogen content of surface and subsurface materials, and the decay of the thermal neutron signal following each pulse may be used to infer the macroscopic thermal neutron absorption cross-section of the bulk material[29].

Orbital gamma-ray instruments must depend on the GCR particle flux as the excitation source for gamma rays. Using the GCR excitation source requires complex modeling of the interaction of the GCR high-energy protons (and higher Z elements) with the regolith to produce a cascade of particles and eventually a neutron flux of about 13 n/cm²-s rather than the isotropic ~3000 n/cm²-s available with a PNG. Variations of the temporal and energy spectral characteristics of the GCR are typically accounted for by normalizing the measurements over a large spatial area where the composition does not change with time, which is difficult on a planetary surface.

For example, the NASA Near Earth Asteroid Rendezvous - Shoemaker (NEAR-Shoemaker) Mission was the first mission to orbit an asteroid and included both an onboard XRS and GRS in its instrument suite. The XRS and GRS measured both naturally occurring radioactivity. X-rays and GCR-induced gamma rays were used to

determine the elemental composition and geochemistry of the surface and subsurface of the Eros asteroid. However many complications throughout the mission, including low GRC flux due to being at Solar maximum, and an incorrect radial distance orbital insertion distance around Eros, yielded little usable information about the bulk composition of the asteroid. The most useful XRS and GRS information was obtained when the NEAR-Shoemaker spacecraft made a soft “crash-landing” on the surface of Eros. Both the orbital and *in situ* measurements relied solely on GCRs as the excitation source to produce gamma rays used to infer the geochemistry of the Eros[30].

Although progress has been made in understanding the nature of primitive asteroids, it is clear that additional geochemical information is needed to link primitive meteorites with their associated asteroid parent bodies. One way to address this problem is to use *in situ* non-destructive neutron/gamma-ray analysis techniques that can measure the bulk subsurface elemental composition. These measurements can be used to infer mineralogy, H content and other properties, that can be compared with results from various other sensing techniques on the microscopic and macroscopic level.

What Possible *In Situ* Measurement Techniques Can Be Used to Obtain the C-complex Asteroid Bulk Geochemistry?

In Situ Measurements

Non-destructive *in situ* neutron/gamma-ray analysis techniques have been used for decades in both the oil industry and for earth science research to determine such things as the bulk elemental composition, porosity, and density of materials[31]. We

have developed and tested a prototype instrument named PING (Probing *In situ* with Neutrons and Gamma rays)[32] that leverages these well-established techniques to measure the bulk subsurface hydrogen content and elemental composition of an asteroid without the need to drill below the surface. These measurements can be used to transform the elemental concentration data into mineralogy data, which can then be used to derive the bulk physical properties of the asteroid material. PING can measure the abundance of nearly all important rock-forming elements and volatiles (e.g. C, H, O, P, S, Si, Na, Ca, Ti, Fe, Al, Cl, Mg, Mn, K, Th, and U) depending on their abundance in the planetary material, down to a depth of 50 cm, thus making it ideally suited to determine the subsurface bulk composition of C-complex asteroids.

The PING instrument (as shown in Figure 3) uses a PNG to irradiate an asteroid with fast neutrons that stimulate the nuclei of the asteroid material beneath the instrument down to 50 cm below the surface and over an area with a 1-m radius. PING also employs gamma-ray and neutron detectors to measure the energies and fluxes of the emitted gamma rays and scattered neutrons that reach the surface. Since each isotope emits gamma-ray lines at characteristic energies, the measurement of their count rates is used to determine how much of each element is present in the soil. The neutron detector count rates are used to determine hydrogen content (such as in hydrous minerals and water), the bulk thermal neutron absorption cross-section, and soil density distributions. Since high-energy neutrons and gamma rays travel far into the regolith, PING can make deep subsurface measurements over a large area without the need for any kind of mechanical penetration of the surface.

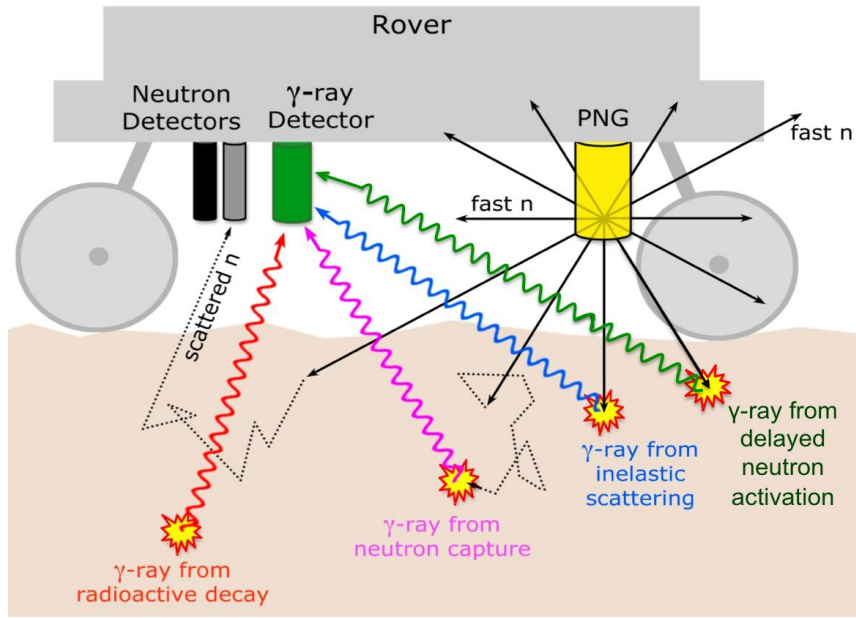


Figure 3. Illustration of PING mounted on a rover showing how it can be used to determine the bulk elemental composition over a 1 m^2 surface area and down to 50 cm below the surface of an asteroid.

PING is a landed instrument that consists of three basic components: 1) a PNG that emits intense pulses of fast (14 MeV) neutrons that are either scattered or captured by the nuclei in the planetary material below the instrument; 2) a gamma-ray spectrometer to measure the characteristic gamma rays emitted by the excited nuclei; and 3) neutron detectors to measure the count rates and energies of the neutrons that are scattered back up toward the surface. The combination of a PNG with gamma-ray and neutron detectors has been used to measure elemental composition in the oil well logging industry for many decades[33],[34]. While there is an extensive literature[33],[35],[36],[37],[38],[39],[40] about how to carefully map and quantify elemental compositions in the down-the-borehole geometry of an oil well, there have been limited efforts to apply this technology to measurements made from the surface[41],[42],[43],[44],[45],[46],[47].

We note that PING differs significantly from the Dynamic Albedo of Neutrons (DAN) experiment on the Mars Science Laboratory (MSL). DAN is an instrument designed to detect subsurface hydrogen (“water”), while PING is designed to determine the full bulk subsurface elemental composition of the regolith in addition to having better sensitivity to hydrogen as DAN, since DAN doesn’t produce enough neutrons to get to as low a level of uncertainty as can be done with a higher output PNG, where this is from the combination of the number of neutrons per pulse times the number of pulses that can be produced for a single measurement. The hardware configurations differ in two significant ways: while DAN consists of its PNG and a set of neutron detectors, PING includes a gamma-ray spectrometer in addition to its neutron detectors. PING also uses a PNG that can put out more neutrons per second and has the flexibility in pulse frequency and pulse width needed so that it can be tuned to work effectively with a gamma ray spectrometer as well as the neutron detectors. Thus PING may be seen as the crucial next step after MSL/DAN.

Neutron Transport

Figure 4 illustrates the different physical processes that occur when planetary surfaces are stimulated by high-energy neutrons. Characteristic gamma rays are emitted by the nuclei in the material as they participate in the resulting inelastic neutron scattering, thermal neutron capture and neutron activation processes. The gamma-ray energies and intensities measured by a spectrometer at the surface are used to determine elemental composition of the regolith. A gamma-ray spectrometer at the surface will also measure the characteristic gamma rays from the decay of naturally radioactive elements such as K, Th and U that are commonly found in planetary materials. No outside

stimulation of these elements is needed for gamma-ray line production (see Boynton et al., 1993[48]; Evans, et al., 1993[49]; Feldman, 2000[50]; and Grau, 1990[51] for a general overview of physics of neutron/gamma-ray techniques).

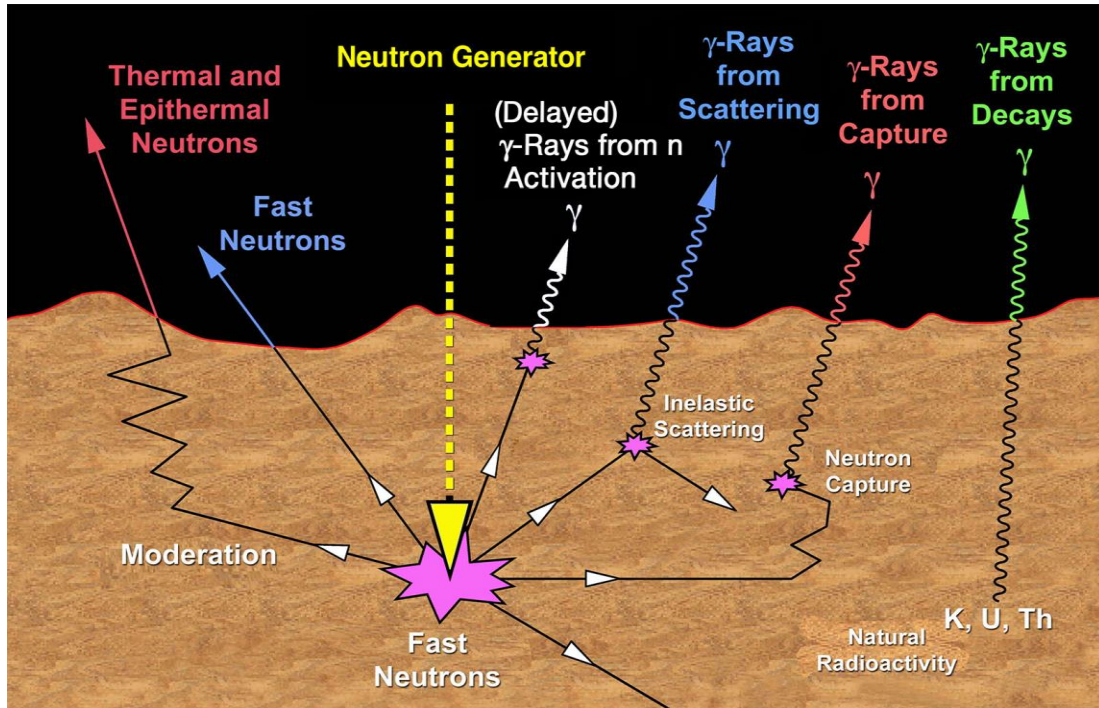


Figure 4. PING takes advantage of four different gamma ray-producing processes: inelastic scattering, neutron capture, neutron activation and natural radioactivity to determine the elemental abundance of the planetary material.

Since the energy spectrum of the gamma rays given off following excitation by fast or thermal neutrons is a superposition of the characteristic lines of the isotopes of the various elements present, all the major constituents of soil and rock can be identified by these neutron-induced gamma-ray emissions. In addition, measurements of the neutrons emerging from the surface will be particularly sensitive to the hydrogen, carbon, and oxygen content of the subsurface material, and thus neutron detectors make excellent instruments for the detection of H, water, ice or frozen CO₂ to depths of about 50 cm. It

is the union of all three components – PNG, gamma-ray spectrometer, and neutron detectors – that makes PING such a powerful approach.

Gamma-Ray Spectroscopy

Converting the measured gamma-ray spectral data to elemental abundances begins with evaluating the peak areas of the many gamma-ray lines of interest, although the actual analysis process may be spectrometer dependent. High Purity Germanium (HPGe) detectors provide the best energy resolution so that simple peak-fitting techniques may be used. However, even the HPGe spectral analysis process may become complicated due to the presence of interfering lines[52]. Peak fitting is also possible for scintillation spectrometers, but the broader energy resolution may make peak identification and analysis more difficult. To reproduce the measured spectra, it is frequently necessary to develop a library of spectrometer response functions for each element likely to contribute[53],[54].

While the strength of the gamma-ray lines depends on the concentration of the isotope of the element that produces the line, the line strength (except for the case of natural radioactivity) also depends on other factors such as the water content and the presence of other neutron-absorbing isotopes in the material. Monte Carlo modeling is needed to take into account the complex ways in which the neutrons interact in planetary surface materials and affect gamma-ray line production[55]. Converting gamma ray spectra to elemental abundances is thus an iterative process where the material composition is adjusted until the predicted line fluxes match the measurements. This forward modeling process is a standard technique and was used successfully to analyze gamma-ray spectra from Mars Odyssey's Gamma Ray Spectrometer[56].

A scientifically crucial capability of PING is its ability to detect subsurface carbon. Knowing the concentration of carbon in comparison to the other major elements in primitive asteroids can be the key to understanding the initial composition of planets in our solar system and the basis for their subsequent geochemical evolution. The gamma-ray line from carbon (4.439 MeV) is in a very accessible part of the gamma-ray spectrum. Since there are manageable spectroscopy challenges in reducing noise from interfering lines and analyzing the Doppler broadening of the carbon peak to get the best sensitivity for carbon, we have used techniques for detecting and optimizing the sensitivity to carbon to be able to distinguish carbonaceous asteroids from other classes of asteroids and this will aid in strengthening the connection between C-complex asteroids and their carbonaceous chondrite meteoritic analogs.

Neutron Data Analysis

Converting neutron count rates, by looking at the time dependence following the pulsed of neutrons at a single location, to geochemical information requires the use of the same type of Monte Carlo simulations as in the gamma-ray analysis. The transport of neutrons through soil depends on both scattering processes that reduce the neutron energies down to the thermal range (0.025 eV) and the diffusion of these thermal neutrons throughout the soil until they are captured. The most commonly used neutron detector is the He-3 proportional counter tube[57]. Separation of the thermal and epithermal neutron count rates in He-3 tubes is easily accomplished using a two-detector system, where a thin Cd shield covers one of the detectors. Since Cd has a very high cross section for neutrons below ~ 0.4 eV, the Cd-shielded detector cannot detect the

thermal neutrons and produces only the epithermal signal. The bare He-3 tube predominantly detects the thermal neutrons, since He-3 has a higher cross-section for thermal than for epithermal neutrons and provides a predominately thermal neutron signal. The neutron energy distribution and the time dependence of these signals produced by a pulsed neutron experiment like PING can be interpreted to provide information on layering configurations, hydrogen content, average atomic density, and soil porosity[58],[59].

Studying the Subsurface Elemental Composition of Asteroids Using PING

Testing PING on Earth

An earlier PING prototype was tested in 2006 by J. Trombka's Goddard Space Flight Center (GSFC) X-ray, Gamma Ray, and Neutron Instrumentation group indoors at Schlumberger's Princeton Technology Center (PTC). This first prototype consisted of Schlumberger's PNG, and NASA GSFC's HPGe and neutron detectors that were suspended using a wooden frame over a meter-sized plastic tub filled with crushed stone with varying amounts of water. Unfortunately these initial test results were ambiguous, due to many factors including neutron interaction with everything in the room including the samples being tested. The test took place in a small room that included a lot of high-Z and hydrogenous material so that there was a high probability of both neutrons and gamma rays scattering off the room walls and contents and back into the detectors.

This dissertation differs significantly from this previous work, due to the lessons learned after reviewing the PTC tests, as well as earlier work on calibrating the NEAR

detector performed in a geometry that was much closer to the approach taken here. This work was conducted using a new PING prototype constructed from off-the-shelf components, and tested outdoors at a facility that was constructed near NASA GSFC. This test site provides two known, well-characterized, meter-sized standard rock monuments, and various layering configurations on the top of the monument using rock and polyethylene tiles as explained in Chapter II.

Testing of PING on an Asteroid Simulant

In order to optimize PING for an asteroid lander, it needed to be tested on a known and well-characterized meter-sized asteroid sample or analog material simulant. Ideally, one would like to use 3 m³ of primitive carbonaceous chondrite meteorites, analogs to C-type asteroids. However, there are currently only 9 of the most primitive carbonaceous chondrite meteorites in existence on Earth (a total amount of approximately 21 kg), so a simulant was constructed.

An appropriate asteroid simulant must have nearly the same neutron response as the C-type asteroid to be studied. The asteroid simulant must have an equivalent neutron spatial distribution within the volume (similar neutron moderation properties) and equivalent neutron absorption processes (similar average macroscopic neutron absorption cross-section) as that of a C-type asteroid. In addition, the asteroid simulant must be located in a region free from any nearby structures; this can be achieved by using the outdoor, planetary neutron and gamma ray instrumentation testing facility described in Chapter II.

To meet these requirements, an asteroid simulant was constructed using alternating layers of basalt and polyethylene on top of a basalt monument located at the test facility at NASA GSFC based on Monte Carlo N-Particle eXtended (MCNPX) computer modeling results and Activation Laboratories (ACTLabs), located in Ontario, Canada, elemental assay information. PING experimental gamma ray and neutron data were collected on the granite and basalt monuments, the asteroid simulant and other various layering configurations. The experimental data taken on the two monuments and the asteroid simulant were analyzed and compared with MCNPX models to quantitatively determine and verify the elemental composition, sensitivity and precision of PING measurements for selected elements.

CHAPTER II

EXPERIMENT DESCRIPTION

Design of the Goddard Geophysical and Astronomical Observatory (GGAO)

Neutron/Gamma-Ray Instrumentation Test Facility

Neutron/Gamma-ray Instrumentation Test Facility

The work presented in this section is from J. Bodnarik, L. Evans, S. Floyd, L. Lim, T. McClanahan, M. Namkung, A. Parsons, J. Schweitzer, R. Starr, and J. Trombka, “A Unique Outside Neutron and Gamma Ray Instrumentation Development Test Facility at NASA’s Goddard Space Flight Center,” 41st Lunar and Planetary Science Conference, **41**, p. 2581 (2010). An outside neutron and gamma-ray instrumentation test facility was constructed at NASA GSFC to evaluate conceptual designs of gamma-ray and neutron systems that are intended to be proposed for future planetary lander and rover missions. We describe this test facility and its current capabilities for operation of planetary *in situ* instrumentation, utilizing a 14 MeV pulsed neutron generator as the gamma ray excitation source with gamma ray and neutron detectors, in an open field with the ability to remotely monitor and operate experiments from a safe distance at an on-site building. The advantage of a permanent test facility with the ability to operate a neutron generator outside and the flexibility to modify testing configurations is essential for efficient testing of this type of technology. Until now, there have been no outdoor test facilities for

realistically testing neutron and gamma-ray instruments planned for solar system exploration.

The test facility at GSFC, shown in Figure 5, consists of two 1.8 x 1.8 x 0.9 meter

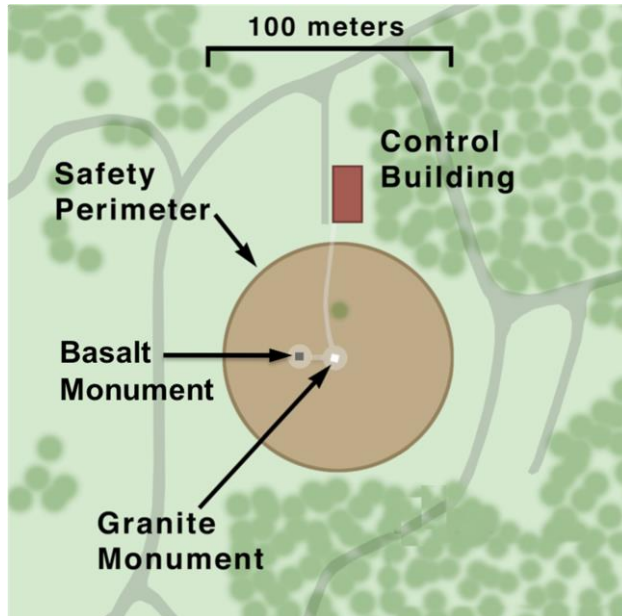


Figure 5. Aerial view of GGAO. This schematic of the outdoor gamma ray and neutron instrumentation testing facility shows the operations control building as well as the 47 m diameter safety perimeter surrounding the two existing 1.8 m x 1.8 m x 0.9 m granite and basalt monuments.

structures of granite and basalt in the middle of an open field with an approximately 50-m radius radiation safety perimeter. A soil profile was conducted, shown in Figure 6, to determine what the drainage would be like in the field and what kind of foundation was necessary support the granite and basalt monuments. The composition of the soil was predominately sand and clay, so it would provide good drainage. As a result of the soil profile and consultation with George Pellettieri, president of Pellettieri Associates Inc. landscape, architecture & construction in Warner, NH, it was decided that both the granite and basalt monuments would be supported on 2.4 x 1.2 m horizontally placed posts that are placed on top of a crushed stone circular area of 3.1 to 3.7 meters in diameter and 31 cm in depth.

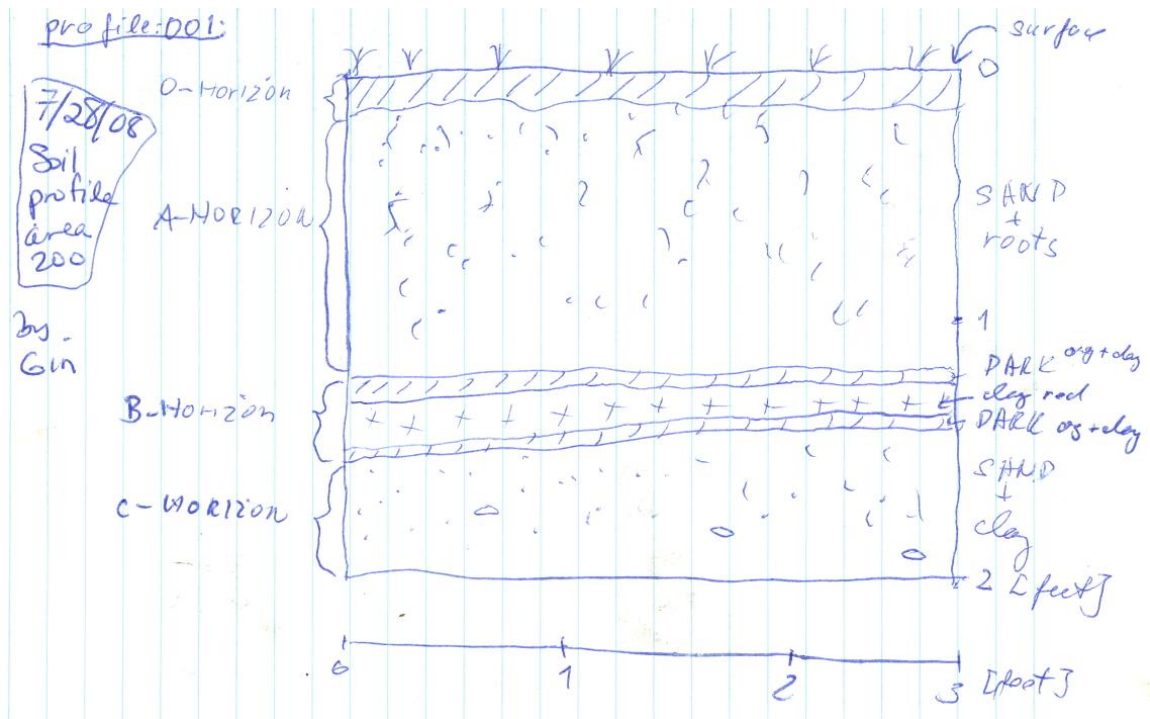


Figure 6. A drawing of the soil profile performed by Gunther Kletetschka and Julia Bodnarik on their shoveled out 0.9 m x 0.9 m x 0.6 m meter pit in the middle of the field at GGAO with 2.1 m tall grass on July 28, 2008.

We remotely operate PING on known samples, minimizing background signals from neutron and gamma-ray interactions with nearby structures, shown in Figure 7. The facility is equipped with an operations building that provides power and communications to the monuments, so users can operate and monitor their systems at a safe distance from the PNG. The radiation safety perimeter is visually monitored during operation, and a video and motion sensor surveillance system will be installed in the near future.



Figure 7. Image of the test facility with the operations building (left), the basalt monument covered with the homogenous C-type asteroid layering simulant (right), and granite monument (far-right).

A unique feature of our test facility is the ability to perform layering studies using granite, basalt and polyethylene tiles with dimensions of 0.31 x 0.31 x 0.013 meters, 0.31 x 0.31 x 0.025 meters, and 0.31 x 0.31 x 0.051 meters to simulate layers of water ice. These materials can be stacked to simulate a variety of layering scenarios, such as simulating the side of a crater or a homogenous C-type asteroid. In addition, we can introduce other materials to test sensitivities of numerous elements. Our large quantity of granite, basalt, and polyethylene tiles and the ability to use various other layering materials affords us great flexibility in constructing numerous configurations to simulate a wide variety of planetary surfaces, geological features and environments.

Design of Physical Rock Configurations

The work presented in these next two sections is from J. G. Bodnarik, J. S. Schweitzer, A. M. Parsons, L. G. Evans, and R.D. Starr, “PING Gamma Ray and Neutron Measurements of a Meter-Scale Carbonaceous Asteroid Analog Material,” 43rd Lunar and Planetary Science Conference, **No. 1544** (2012). The two meter-sized structures at the test

facility are constructed out of Concord Grey Granite from the Swenson Granite quarry in Concord, N. H. and Columbia River Basalt from the Corbett Station Quarry in Corbett, Oregon. These materials were chosen for various reasons, including the ability to acquire more of the same exact material directly from each quarry for additional layering configurations and the ability for others to reproduce the experiments with known, well-characterized materials. The granite structure was selected due to its uniform elemental composition, its density and the ability to control water content outdoors due to its low porosity. The basalt structure was selected due to its uniform elemental composition that was analogous to planetary bodies like Mars, as well as its density and low porosity. A sample of each monument was sent to ActLabs in Ontario, Canada for a detailed independent elemental assay measured to ppb levels, with the results in Appendix I. In addition, the size and placement of the structures in an open field was selected to insure that the neutrons from the PNG were only interacting with the granite or basalt itself.

Meter-sized Asteroid Analog

In order to optimize PING for an asteroid lander, we need to test PING on a known and well-characterized meter-sized test sample or simulant. Ideally, one would use 3 m³ of primitive carbonaceous chondrite meteorites, analogs to C-type asteroids. However, there are only 9 of the most primitive carbonaceous chondrite meteorites on Earth (a total amount of approximately 21 kg), so it was necessary to construct an asteroid simulant.

It was required that an appropriate asteroid simulant must have nearly the same neutron response as the C-type asteroid. The asteroid simulant must have an equivalent

neutron spatial distribution within the volume (similar neutron moderation properties) and equivalent neutron absorption processes (similar average macroscopic neutron absorption cross-section) as that of a C-type asteroid. In addition, the asteroid simulant must be isolated from human traffic to prevent interference from structures or even soil and flora, which can be achieved by using our outdoor, planetary neutron and gamma ray instrumentation testing facility.

To meet these requirements, an asteroid simulant was constructed using 16-alternating layers of Columbia River basalt and high-density polyethylene (HDPE) on top of a Columbia River basalt monument located at our testing facility. Figure 8 shows the set-up of the PING components on top of the basalt layering asteroid simulant.

The basalt layering asteroid simulant material selection and construction was based on MCNPX[60] computer modeling results and ACTLabs independent elemental assay information. MCNPX modeling was used to compare the neutron spatial distribution of a homogenous C-type asteroid and basalt layering asteroid simulant to insure that the simulant and C-type asteroid had similar neutron moderation properties. To insure that the neutron response for the basalt sample is like that of a C-type asteroid, the key elements are that the thermal and epithermal neutron fluxes, as a function of depth beneath the surface, need to closely approximate those of a C-type asteroid. Figure 9 shows the MCNPX modeling results for the epithermal and thermal neutron fluxes as a function of depth beneath the surface for both a C-type asteroid and the basalt layering asteroid simulant. The basalt layering asteroid simulant model is in good agreement with the C-type asteroid CI1 (Ivuna-like) carbonaceous chondrite composition model. The basalt layering asteroid simulant clearly mimics the neutron flux

distribution for the C-type asteroid composition, especially since the majority of the gamma rays produced through nuclear interaction processes will be coming from the surface down to ~30 to 35 cm. The fluctuations in position of the data points for the basalt layering simulant are due to the fact that the simulant is layered and the C-type asteroid is homogenous.

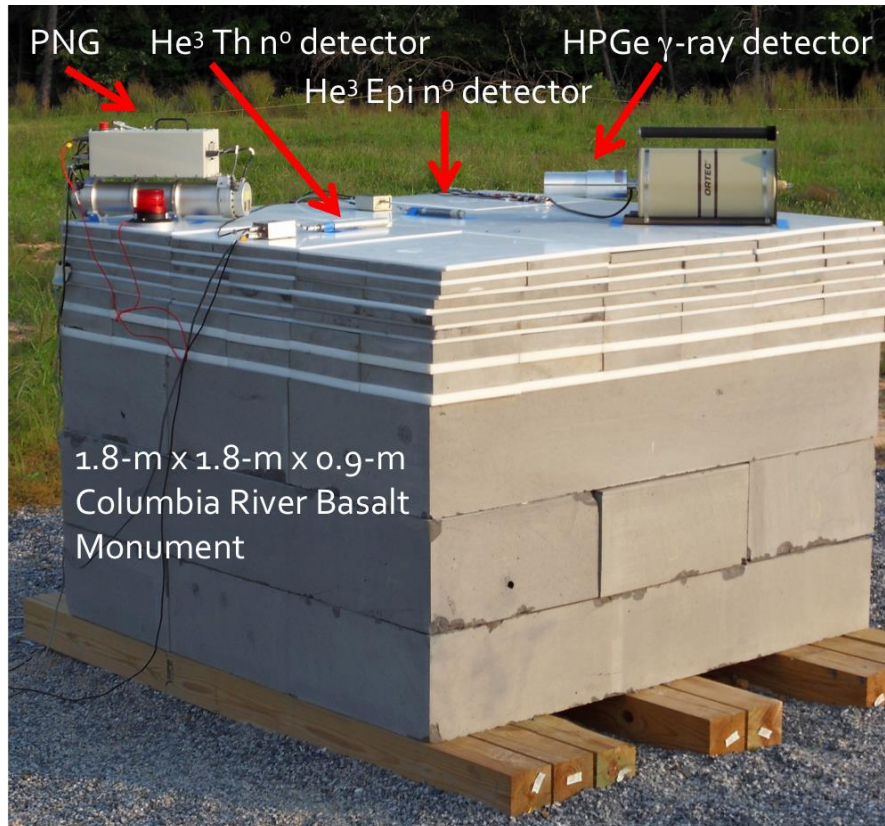


Figure 8. Image of PING components on the C-type asteroid simulant.

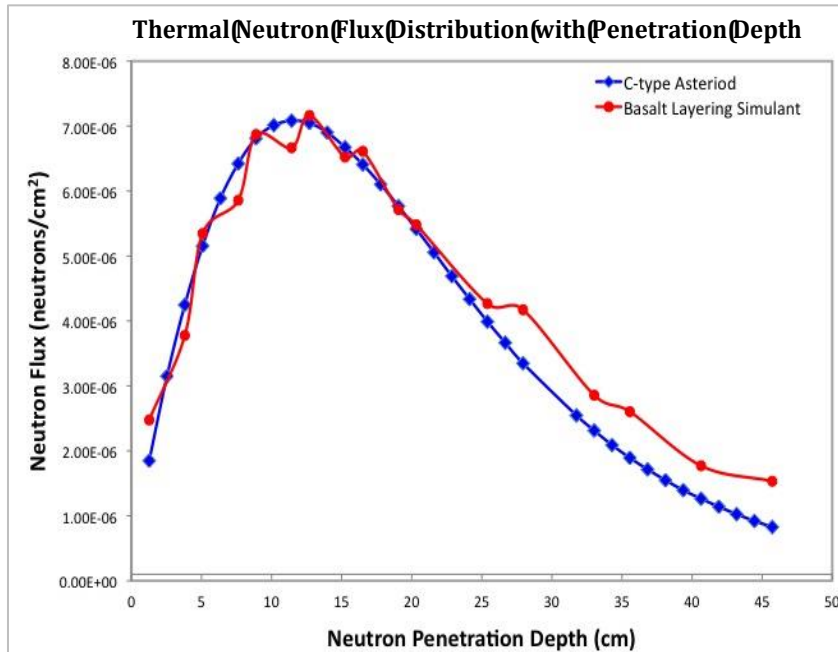
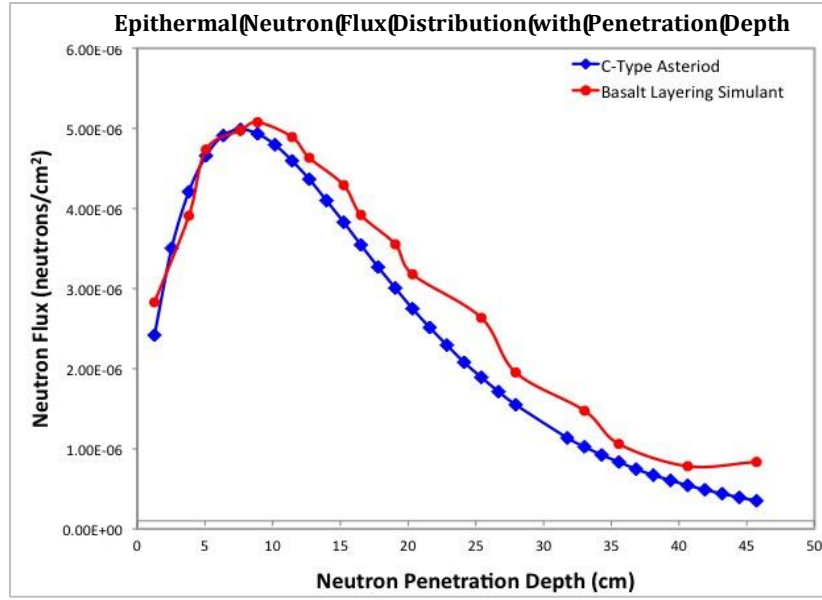



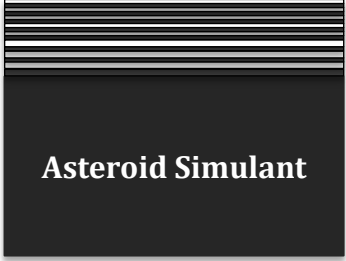
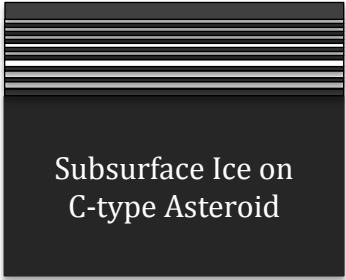
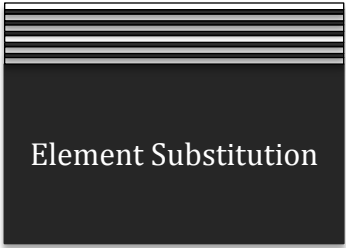
Figure 9. Graphs of the MCNPX computer modeling results of the epithermal and thermal neutron flux distribution as a function of neutron penetration depth for the C-type asteroid (blue) and the basalt layering asteroid simulant (red).

Experimental Rock Configurations

PING was tested on a total of 10 experimental rock configurations, summarized in Table 1 and described in detail in Appendix II, to determine the sensitivity to elements

necessary for biogenic precursors such as C, O, S, and H and for rock forming elements to unveil the volatile and organic nature as well as the basic geochemistry of C-type asteroids. Knowing the concentration of these elements as well as subsurface features in these most primitive asteroids will help answer important questions about the early history of the Solar System, its evolution and the formation of the Earth.

Table 1: Material Configurations for Each PING Experiment

Material Configuration	Description & Purpose	Figure
Concord Grey Granite and Columbia River Basalt Monuments	Monuments simulate planetary analogs with each having a total volume = 1.8-m x 1.8-m x 0.9-m	 Basalt or Granite Monument
C-type Asteroid Simulant	Layering configuration simulates a homogenous C-type asteroid meteoritic CI1 chondrite analog with a total volume = 1.8-m x 1.8-m x 1.4-m	 Asteroid Simulant
Subsurface Water Ice	3 configurations consisting of the C-type asteroid simulant covered with 2.54 cm, 3.08 cm, and finally 5.62 cm of basalt layers with volumes of 1.8-m x 1.8-m x 1.4-m, 1.8-m x 1.8-m x 1.7-m, and 1.8-m x 1.8-m x 2.0-m.	 Subsurface Ice on C-type Asteroid
Basalt & Granite Substitution Layering	3 configurations consisting of layers of basalt and polyethylene on top of basalt monument, where the top layer and then the top 2 layers of basalt are replaced with granite	 Element Substitution

PING Experimental Equipment Set-up on Rock Configurations

The spacing dimensions of the components of the PING instrument (HPGe, ³He epithermal and thermal neutron detectors, and the PNG) are shown in the Figure 10. The same PING component spacing was used for all experimental rock configurations. Appendix II has a more detailed description of both the experimental rock and PING instrument component spacing information.

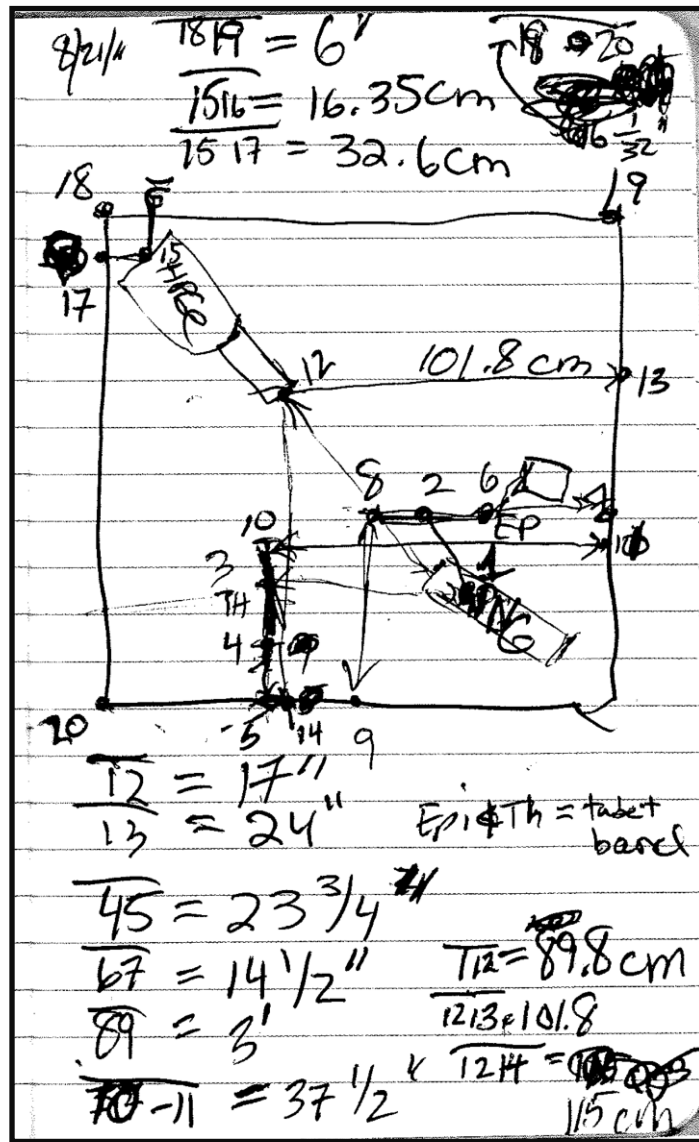


Figure 10. Drawing of the spacing of the PING components using for each experimental configuration.

PING Experimental Equipment Description

PING employs a pulsed neutron generator to excite materials at and below a planetary surface and utilizes the penetrating nature of these fast neutrons and gamma rays to probe the subsurface soil composition over a 1 m² area and down to depths of 10-100 cm. PING's gamma-ray spectrometer and neutron detectors measure the resulting gamma rays and neutrons that emerge from the planetary surface.

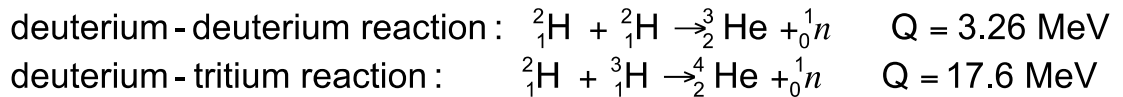
A gamma-ray spectrometer measures the resulting inelastic scattering, capture, and delayed activation gamma rays emitted by the excited elements as well as gamma rays emitted from natural radioactive decay; neutron detectors measure the number of the epithermal and thermal neutrons that reach the surface as a function of time relative to the initiation of each high-energy neutron pulse. PING gamma-ray and neutron data are acquired using custom software to control digital signal analyzer electronics. These data, coupled with MCNPX[60] computer simulations, let us quantitatively determine the bulk elemental composition of the subsurface material for any solid body in the Solar System, even bodies with a dense atmosphere. PING can measure a wide range of elements (e.g. C, H, O, P, S, Si, Na, Ca, Ti, Fe, Al, Cl, Mg, Mn, K, Th, and U) depending on their abundance in the planetary material.

Pulsed Neutron Generator

The PING instrument uses a Thermo Scientific MP320 14 MeV Deuterium-Tritium (D-T) PNG [19], shown in Figure 8. During the experiments, The PNG beam current, high voltage, frequency, and duty factor were set to 60 μ A, 50 kV, 1 kHz, and

10% respectively. At these settings, the PNG produced a neutron pulse width, pulse period, energy, and rate of 100 μs , 1000 μs , 14 MeV, and 3×10^7 n/s respectively.

One can think of neutron generators as compact particle accelerators, where the neutron generation process for the Deuterium-Deuterium (D-D) or D-T compact generators is as follows: The deuterons are accelerated toward a light target nucleus containing deuterium or tritium, an applied voltage difference of about 100-300 kV; and interact with either the deuterium or tritium in the target material causing fusion to occur in Helium isotopes and the production of neutrons:



where the resultant neutron beam energy is uniform, since the Q-values are significantly larger than the initial particle energy.

A PNG, containing 1.5 Ci (55.5 GBq) of tritium, works by having ions accelerated to a target and 14 MeV neutrons are produced through the reaction $\text{D} + \text{T} \rightarrow \text{n} + {}^4\text{He}$. The tube is pulsed electronically and consists of a source to generate positively charged ions. Figure 11 is an illustration of a PNG that consists of: one or more structures to accelerate the ions (usually up to ~ 80 kV); a metal hydride target loaded

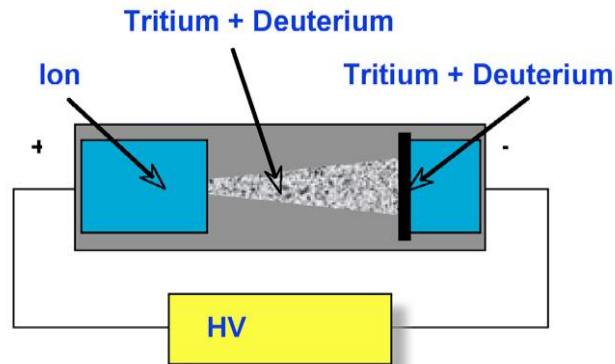


Figure 11: A schematic of a PNG.

with either deuterium, tritium, or a mixture of the two; and a gas-control reservoir, also made of a metal hydride material. Figure 12 is a photograph of a generator[61].

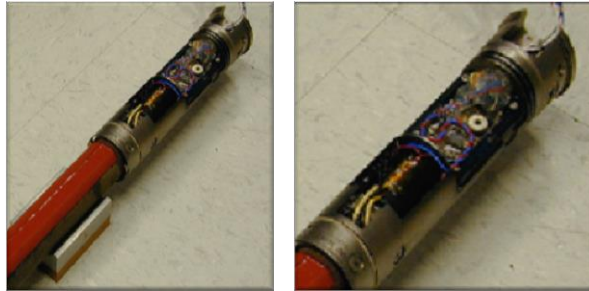


Figure 12: A picture of a Cockcroft Walton neutron generator.

Acquisition Electronics, Gamma-Ray and Neutron Detectors

During these experiments, we acquired event-by-event time-tagged channel/energy and time information or time-stamped list mode (TLIST) data using Lynx Digital Signal Analyzer (DSA) electronics connected to an n-type Ortec GMX Series HPGe portable coaxial detector system, University of Tennessee thermal bare ^3He and epithermal Cd-wrapped ^3He detectors, and a PNG positioned on top of various rock and layering configurations, shown in Figure 4. The Lynx DSA reading out the HPGe, and thermal and epithermal neutron detectors were connected directly to the PNG to synchronize the start of each data acquisition run with the start of a neutron pulse.

Gamma-Ray Detector

An n-type Ortec GMX Series HPGe portable coaxial detector system (crystal diameter=53.2 mm and crystal length=69.5 mm), in the bare and enclosed in a borated rubber cap (to reduce the effects of fast neutron damage of the Ge crystal) configurations,

was used to acquire gamma ray data. The HPGe semiconductor gamma-ray detector is attached to a portable liquid nitrogen dewar that cools the detector down to 77 K. The HPGe detector used has the following specifications as originally specified and/or measured by the Ortec manufacturer: 1) detector model number: GMX30-76-A-PL; 2) serial number: 49-N22577A; 3) cryostat configuration: CFC-GG-76; 4) dewar model: DWR-5.0G; 5) dewar capacity: 5 liters; 6) detector cool-down time: 6 hours; 7) static holding time: 3 days; 8) preamplifier model: A232N; 9) H. V. filter model: 138EMI; 10) H. V. filter serial number: 9198922; 11) high voltage bias: -3500 Volts (-3000 Volts after HPGe was repaired by the manufacturer and returned in August 2012); 12) resolution (Full Width at Half Maximum (FWHM)) at 1.33 MeV, ^{60}Co : 1.8 keV (amplifier shaping time of 6 μs); 13) peak-to-Compton ratio, ^{60}Co : 63:1 (amplifier shaping time of 6 μs); 14) relative efficiency at 1.33 MeV, ^{60}Co : 30% (amplifier shaping time of 6 μs); and 15) peak shape (FWHM/Full Width at Tenth Maximum (FWTM)), ^{60}Co : 2.4 (amplifier shaping time of 6 μs). Figure 13 shows a schematic cross-section of an n-type coaxial detector.

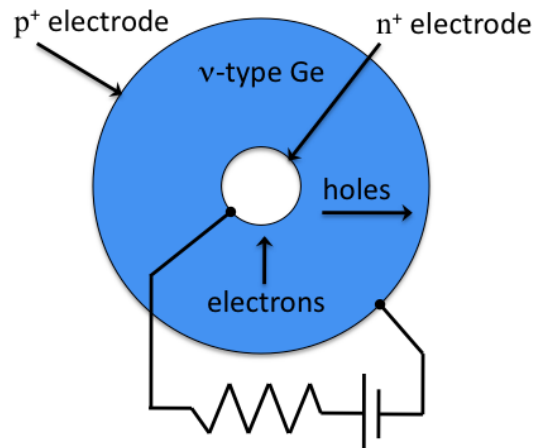


Figure 13. Schematic of the cross-section perpendicular to the cylindrical axis of the n-type HPGe detector crystal.

Radiation is measured by the detector according to the number of free charge carriers between the detector's two electrodes produced by ionizing radiation interacting with the crystal creating free electron-hole pairs[62]. The intensity of the detected radiation is proportional to the number of electron-hole pairs. The ionizing radiation creates a number of electrons that are transferred from the valence to the conduction bands and an equal number of holes are created in the valence band. When a potential is applied across the detector's two electrodes, the electrons and holes travel in opposite directions to the electrodes, resulting in a pulse that is measured by an outer circuit described by the Shockley-Ramo Theorem. Since the energy to create an electron-hole pair is known, the measurement of the number of electron-hole pairs is proportional to the intensity of the incident radiation on the detector.

Neutron Detectors

A Cd-wrapped ^3He epithermal neutron detector (aluminum cylinder length=15cm, aluminum cylinder radius=1.25cm, Cd-wrap thickness=0.02cm, ^3He gas pressure=0.035g/cm³ (200atm)) and a bare ^3He thermal neutron detector (aluminum cylinder length=15cm, aluminum cylinder radius=1.25cm, ^3He gas pressure=0.035g/cm³ (200atm)) from the University of Tennessee were used to collect neutron data for the PING instrument experiments*. The gas proportional epithermal and thermal neutron detectors were used to measure neutrons detected as a function of time during the PNG pulse period to observe the epithermal and thermal neutron dieaway to determine the H-content, and thermal macroscopic neutron absorption properties of the bulk material. The

* A ^3He detector borrowed from Stan Hunter through the Navy was also used to collect data for the PING experiments, but due to cable connection problems the data was deemed unreliable and therefore was not analyzed.

basic bare ^3He thermal neutron detector^{**} is a gas proportional counter consisting of a pressure vessel containing pressurized ^3He gas and electrodes with an applied potential used to move charge within the gas for detection. The detector includes a fine, high-voltage anode wire that has a strong electrostatic field that causes electrons to drift quickly to the anode and the positive heavy ions to drift to the cathode. As the accelerated electrons approach the anode they have energies sufficient enough to ionize more gas. This causes the electrons to participate in a “Townsend avalanche”, which multiplies the electron charge by a factor of 10^6 and remain localized along the wire near the event. This event causes the detector, which acts as a capacitor, to discharge slightly and the connected electronics record the resulting electrical pulse with a pulse amplitude that is proportional to the number of charged particle-produced electrons. As shown in the reaction[63] in Figure 14, a neutron colliding with a ^3He nucleus will produce a proton at 764 MeV, which will ionize the gas. Figure 14 also shows a schematic of a gas detector, where approximately 25,000 ions and electrons are produced per neutron ($\sim 4 \times 10^{-15}$ coulomb) and the cross-section for ^3He .

^{**} The only difference between the bare ^3He thermal neutron detector and the Cd-wrapped ^3He detector is that the bare ^3He detector predominately detects thermal neutron, due to the high cross-section of ^3He for n detection, and some epithermal neutrons, while the Cd on the Cd-wrapped epithermal neutron ^3He detector absorbs the thermal neutrons and hence mainly detects epithermal neutrons due to the high cross-section of Cd to absorb thermal neutrons.

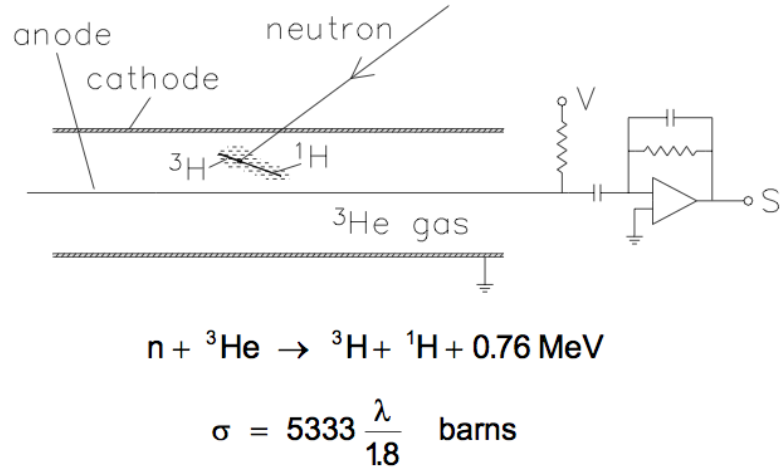


Figure 14. Schematic of a ${}^3\text{He}$ neutron gas detector.

Lynx DSA Electronics and Acquisition Software

A Canberra Lynx DSA is used to acquire data from each gamma ray and neutron detector used for a PING measurement. Figure 15 a and b are an images of the front and back of the Lynx DSA. A more detailed description of While the Lynx DSA hardware[64] features multiple data acquisition modes, including coincidence-gated Pulse Height Analysis (PHA) and event-by-event TLIST mode, operation of the Lynx DSAs in TLIST mode required the development of custom software.

Lynx DSA data acquisition can be performed using either the Lynx web-based interface or the Genie 2000 software package[64] both available from Canberra Industries. Although the Lynx DSA hardware offers the required TLIST mode, neither of these software options provides the flexibility and all of the capabilities we need for our specific instrument application. The MultiScan software, designed specifically for our project, allows us to 1) acquire data in TLIST mode while synchronized to the PNG pulse, 2) save data in ASCII format, 3) analyze TLIST data for an unlimited number of

time windows, and 4) perform multiple consecutive data acquisitions while maintaining the Lynx graphical analysis and configuration features.

a)



b)

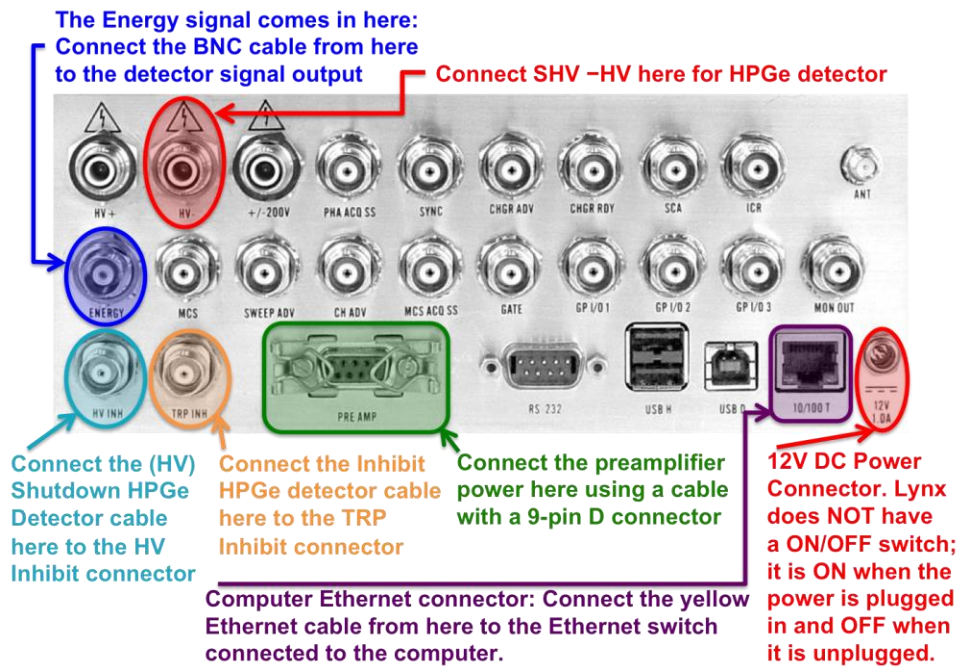


Figure 15. Lynx DSA Images of a) the front and, b) the back (showing connection ports for HPGe) of the acquisition system.

The MultiScan software was written in Java, since we needed to make the code cross-platform and easy to understand so that others can make changes to the code when

necessary. When starting a new data acquisition or scan, the user can specify which of the multiple Lynx DSAs to perform the scan, the acquisition mode (PHA or TLIST), the file format to save the data (Canberra CNF file, ASCII text file, or both), how many consecutive scans to perform, and the duration of each scan (in either live time or true time). Settings can be modified quickly and easily within the software. The data are both written to a file and presented in a large display window with multiple data visualization features. The program also provides basic data analysis tools for both PHA and TLIST scans, and off-line TLIST data post-processing time-slicing tools, as well as a diagnostic feature for monitoring the operating parameters within the Lynx DSA[65]. Details of the experiment operations manuals can be found in Appendix III.

CHAPTER III

DATA ANALYSIS AND MCNPX CALCULATIONS

Experimental Data Analysis

The following sections *Experimental Data Analysis through Identifying and Removing Sources of Systematic Error Using TLIST data* are all from the peer-reviewed publication in J. Bodnarik et al., (2013), “Time-Resolved Neutron/Gamma-Ray Data Acquisition for In Situ Subsurface Geochemistry,” *Nucl. Inst. and Methods in Phys. Research A*, v. 707, p. 135-142.

PING gamma-ray and neutron data are acquired using custom software to control the digital signal analyzer electronics and synchronize time-tagged event-by-event data acquisition with the start of each PNG burst. These data coupled with MCNPX[55] computer simulations allow us to quantitatively determine the bulk elemental composition of the subsurface material for any solid body in the solar system. The MCNPX calculations allow a statistical calculation of both the energy and the time of a gamma-ray event detected in a detector. The calculations take into account the primary factors involved in neutron production and transport and track most of the nuclear reactions on all elements present in the material, many of the gamma rays that can be produced as well as their transport and detection at a specific point in space by a particular detector. Thus, the Monte Carlo calculations provide a direct relationship

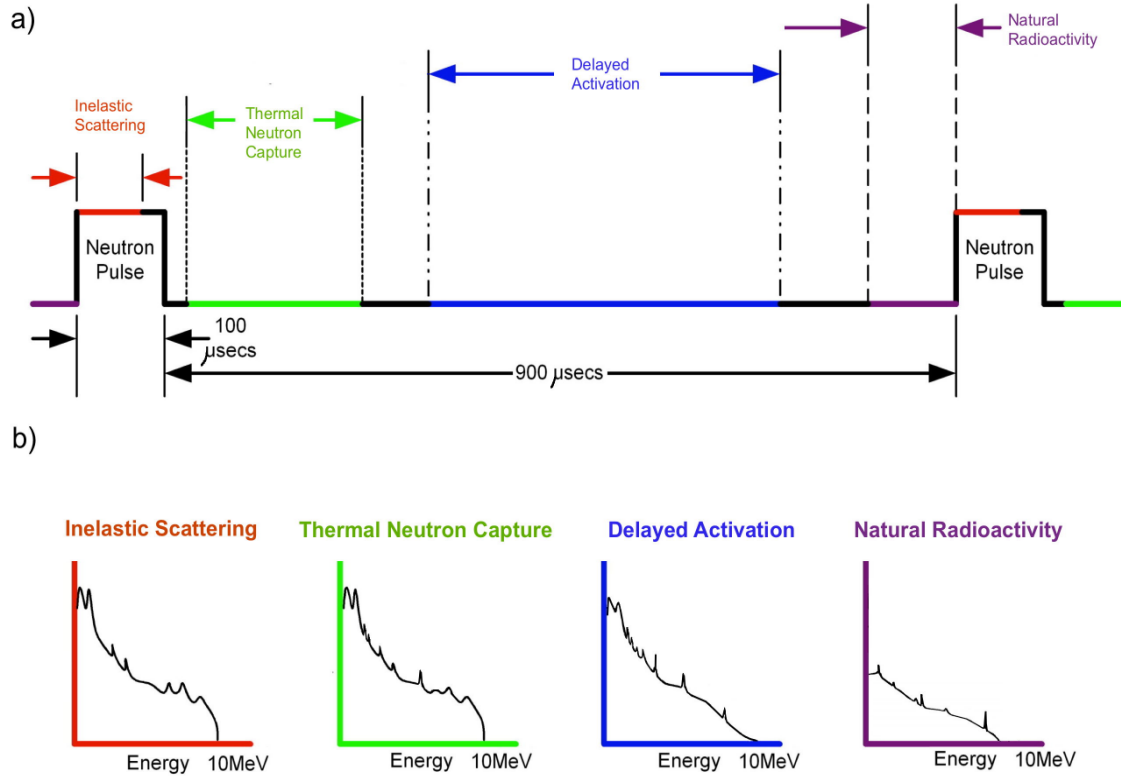
between peak counts and elemental concentrations, limited only by the count rate uncertainty and the calculation uncertainties (generally less than 1%).

Gamma-Ray Data Analysis

The TLIST Data Acquisition Technique[66]

Analyzing individual gamma-ray peaks in a traditional PHA energy spectrum can be challenging due to both interfering lines and the background continuum resulting from multiple processes. We reduce these effects and obtain higher gamma-ray line sensitivity with increased signal-to-noise by recording gamma-ray time and energy in an event-by-event mode synchronized to the start of each PNG pulse. We use our custom MultiScan software and the Canberra Lynx DSA in TLIST mode to record the energy and time (temporal resolution $0.1 \mu\text{s}$) of each event detected during a PNG pulse cycle. We obtain a master data set that is not limited to predetermined coincidence timing gates set for specific nuclear processes. This master data set can be sliced in many ways without loss of information or requiring additional measurements with different data acquisition window settings. Figures 1a and b illustrate the results of our post-processing of TLIST gamma-ray data for various timing windows. The sharp lines shown in this figure are merely used to demonstrate how one can take advantage of time-slicing gamma-ray data. An important benefit of this technique is that for specific gamma-ray peaks, different windows may be selected than those that apply to the bulk of the data. For example, a

delayed activation peak that does not interfere with a capture peak can have an analysis window that starts well before the bulk of the capture gamma rays have disappeared.



Figures 16. Timing Windows and Sample Spectra. a) Placement of timing windows relative to each PNG pulse. b) Examples of different spectral shapes seen in different timing windows.

Figure 16a is an illustration of the PNG fast neutron pulse train and the intra-pulse location of the different timing windows needed to separate the gamma rays that result from the inelastic scattering, thermal neutron capture, delayed activation and natural radioactivity processes. Figure 16b is an illustration of the differences in the resulting energy and intensity of the gamma ray lines and background for each of these separated spectra.

TLIST Data Analysis Technique

We use the MultiScan software with Lynx DSAs to acquire TLIST data for gamma-ray and neutron detectors with the start of a data acquisition synchronized with the start of a PNG pulse. Synchronization of the PNG and DSA clocks insures the accuracy of these event times over multi-hour data acquisition runs. Our basic post-processing procedure for the individual event-by-event data files is to take the modulus of the absolute times for the detected events with respect to the known PNG pulse period to derive the time of each event relative to the neutron pulse. The next step is to put all of the files for a given experiment on the same time base. The result is a master data set of energies and relative event times that can be “sliced” in any number of ways. Slicing the data in time means establishing the boundary between times where different nuclear processes dominate. The result is separate gamma-ray spectra for the specific processes that have the event statistics characteristic of the total acquisition time. Slicing the data in energy means establishing energy boundaries around spectral features whose time profile one wishes to study. After generating this master data set with energy and relative time values, we can analyze our gamma ray and neutron data to infer the bulk elemental composition, density, and subsurface layering of planetary bodies.

Gamma-ray line identification problems can be lessened with the PING instrument by taking advantage of the pulsed nature of the *in situ* neutron source synchronized with the data acquisition system, particularly if the neighboring energies originate from reactions having different time delays relative to the production of the neutron. Naturally, different reactions that occur at the same time, such as prompt (n,n'),

(n,p) and (n, α) reactions that all require high energy neutrons cannot be separated from each other by selecting different analysis times.

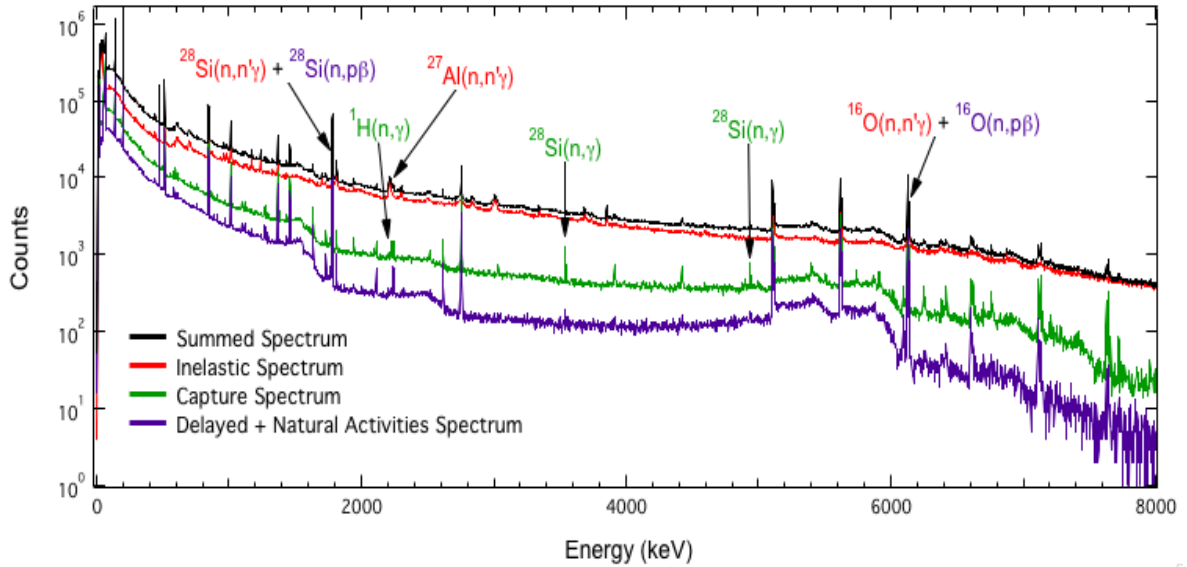


Figure 17. Spectra from Different Time Windows. Gamma-ray spectra from a 6.33-hr acquisition using a HPGe detector on top of Columbia River basalt.

Figure 17 is a plot of four different gamma-ray spectra for a 6.33-hr live time acquisition with the PING instrument using a HPGe detector on the basalt monument, consisting of: 1) a total gamma-ray spectrum (in black) including all neutron-nuclei gamma-ray processes; 2) an inelastic gamma-ray spectrum (in red) created by only selecting gamma-ray events during the PNG pulse for $t=20-100 \mu\text{s}$; 3) a neutron capture gamma-ray spectrum (in green) created by only selecting gamma-ray events after the PNG pulse for $t=150-650 \mu\text{s}$; and 4) a delayed activation and natural activity gamma-ray spectrum (in purple) created by only selecting gamma-ray events for $t=650-999 \mu\text{s}$. Note that, as expected, different gamma-ray lines appear in these spectra. Our technique thus allows us to isolate gamma-ray events for specific interactions from a single element without accumulating excessive background when the peaks are not actually present.

Even if a better energy resolution detector like HPGe is used, gamma-ray line identification can still be challenging, due to multi-element neutron-nuclei interactions that produce gamma rays at the same energy but from different elements. Table 2 lists examples of gamma-ray line energies and their possible sources from neutron-nuclei interactions with different elements, demonstrating how multiple elements can contribute to the same line energy. (Note that the first entry in Table 2 contains two gamma ray lines at slightly different energies. They are grouped together because under many circumstances, they cannot be separated.)

Table 2: γ -ray lines to analyze for inelastic γ -ray spectra time window optimization.

Gamma-Ray Lines (keV)	Possible Sources of Neutron Nuclei Interactions
844-847	A, B, C, D, E
1014	A, D
1779	F, G, H
1811	B, C, E
2211	A
6129	I, J
Key: A: $^{27}\text{Al} (n, n'\gamma) ^{27}\text{Al}$ B: $^{56}\text{Fe} (n, n'\gamma) ^{56}\text{Fe}$ C: $^{56}\text{Fe} (n, p) ^{56}\text{Mn} (\beta) ^{56}\text{Fe}$ D: $^{26}\text{Mg} (n, \gamma) ^{27}\text{Mg} (\beta) ^{27}\text{Al}$ E: $^{55}\text{Mn} (n, \gamma) ^{56}\text{Mn} (\beta) ^{56}\text{Fe}$ F: $^{28}\text{Si} (n, n'\gamma) ^{28}\text{Si}$ G: $^{28}\text{Si} (n, p) ^{28}\text{Al} (\beta) ^{28}\text{Si}$ H: $^{27}\text{Al} (n, \gamma) ^{28}\text{Al} (\beta) ^{28}\text{Si}$ I: $^{16}\text{O} (n, n'\gamma) ^{16}\text{O}$ J: $^{16}\text{O} (n, p) ^{16}\text{N} (\beta) ^{16}\text{O}$	

Problems with interfering lines can be dealt with by examining the time profile of the individual gamma ray lines. Figure 18a is an example of a 6.33-hr summed HPGe gamma ray spectrum taken with PING instrument on top of the basalt monument. In this spectrum there are many gamma ray lines that are clearly interfering with one another such as, the Doppler broadened $^{27}\text{Al}(n,n'\gamma)$, $^1\text{H}(n,\gamma)$, ^{24}Na (SE), the Doppler broadened $^{24}\text{Mg}(n,n'\gamma)$, and the $^{30}\text{Si}(n,n'\gamma)$. One way to distinguish $^{27}\text{Al}(n,n'\gamma)$ and the $^1\text{H}(n,\gamma)$ gamma ray lines is by plotting the net peak area of the unresolved spectral feature in Figure 18a as a function of time, as shown in Figure 18b, to distinguish which line is present. Figure 18b shows the time histograms of the net peak areas for the 2211 keV $^{27}\text{Al}(n,n'\gamma)$ and the 2223 keV $^1\text{H}(n,\gamma)$ gamma ray lines. The time histograms are the gamma-ray count rates per 10 μs time interval and demonstrate that one can distinguish between and separate interfering lines by nuclear process to improve both the peak identification and the measurement precision.

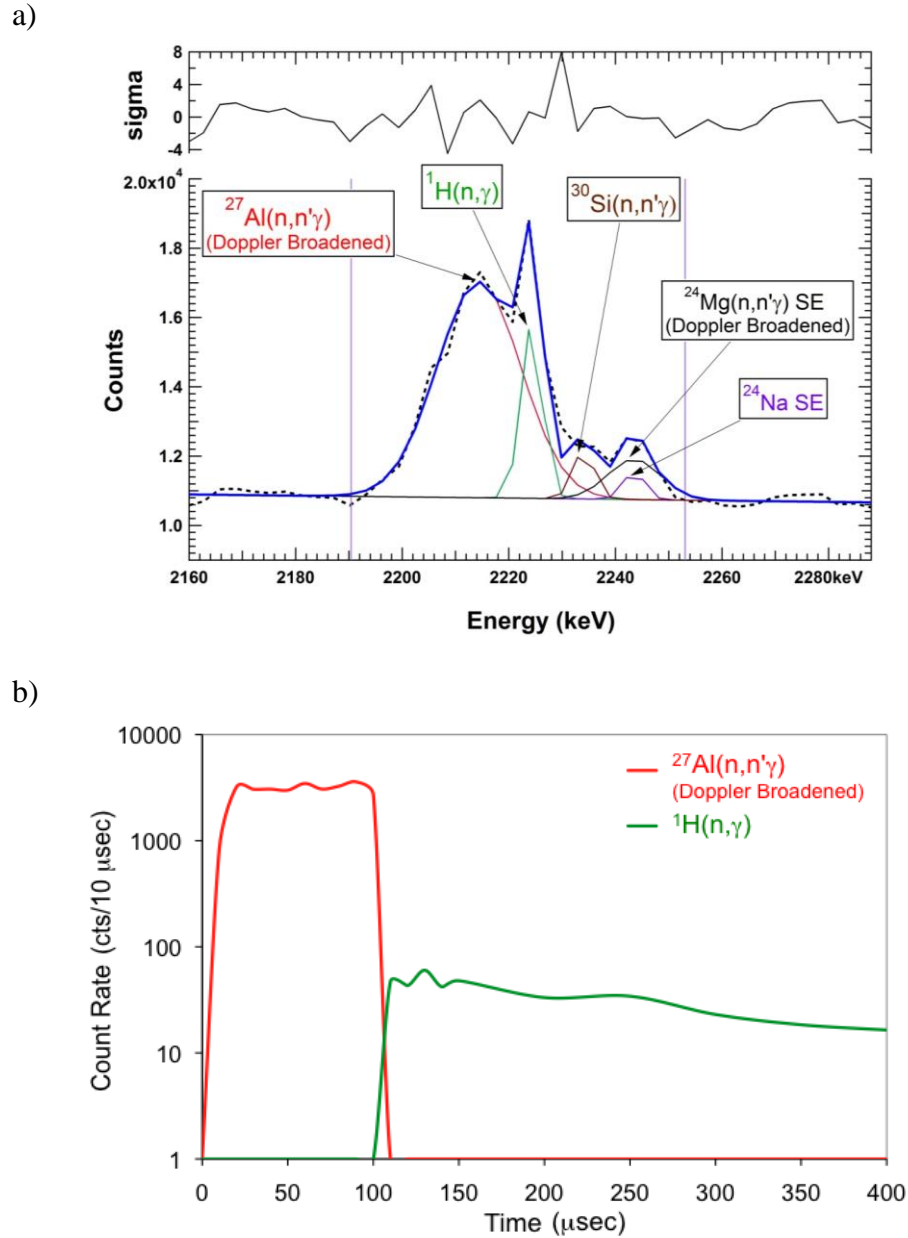


Figure 18. Spectral Feature and Time Distribution. a) A portion of the non-time sliced 6.33-hr gamma ray energy histogram from PING data taken on the bare basalt monument. b) Time histogram showing how one can get better precision on the net peak area of each line, shown in Table 2, by analyzing their respective energy histograms during different time slices during the PNG pulse period.

Improved Gamma-Ray Measurement Precision

By reducing the background, separating a gamma-ray spectrum by nuclear process improves the overall gamma-ray line measurement precision. As seen in Table 3,

listing the total number of peak counts in an energy peak for different time windows, many of the time-gated inelastic scattering and capture lines show improved precision as compared with the same lines in the summed spectrum. The 3539 and 4934 keV $^{28}\text{Si}(n,\gamma)$ capture lines show improved precision resulting from time-gated analysis. The precision of these Si lines in the summed spectrum, representing results without time slicing, is 8.3% and 16.9%. These same Si lines show improved precision (7.3% and 9.2%) in the thermal neutron capture spectrum obtained from the removal of the gamma-ray background due to inelastic scattering. A similar but somewhat smaller improvement is seen for the 2211 keV $^{27}\text{Al}(n,n'\gamma)$ inelastic line.

Table 3. HPGe gamma-ray line intensities (I_γ) and uncertainties (σ) during different time windows for a 6.33-hr PING acquisition on the bare Columbia River basalt monument. For the 1779 and 6129 keV activation peaks, the half-lives are 2.3 min and 7.1 s, respectively. Note the Activation column includes data from all times that the neutron pulse was off. Neutron thermalization begins even before the fast neutron pulse turns off at 100 μ s and it reaches a peak at approximately 100 μ s and then slowly decays, therefore the $^1\text{H}(n,\gamma)$ 2223 keV gamma-ray line appears in both the inelastic scattering and thermal neutron capture windows due to the time windows selected for these processes.

E (keV)	Summed Data		Inelastic Scattering Window			Thermal Neutron Capture Window			Activation		
	Ig (cts)	σ (%)	ID	Ig (cts)	σ (%)	ID	Ig (cts)	σ (%)	ID	Ig (cts)	σ (%)
1779	90480	0.48	$^{28}\text{Si}(n,n'\gamma)$	31730	1.0				$^{28}\text{Si}(n,p)$ $^{27}\text{Al}(n,\gamma)$	57980	0.52
2211	24310	1.55	$^{27}\text{Al}(n,n'\gamma)$	23760	1.5						
2223	1892	16.1	$^1\text{H}(n,\gamma)$	967	14.5	$^1\text{H}(n,\gamma)$	887	7.4			
3539	1154	8.3				$^{28}\text{Si}(n,\gamma)$	1158	7.3			
4934	1472	16.9				$^{28}\text{Si}(n,\gamma)$	1151	9.2			
6129	19920	1.1	$^{16}\text{O}(n,n'\gamma)$	10900	1.67				$^{16}\text{O}(n,p)$	9087	1.42

An interesting situation is observed for the 1779 keV $^{28}\text{Si}(n,n'\gamma)$ and 6129 keV $^{16}\text{O}(n,n'\gamma)$ inelastic lines shown in Table 3. These gamma rays are also produced in the other two spectra by delayed activation reactions (see Table 2). Therefore, the 1779 and 6129 keV gamma ray lines in the summed spectrum have a better statistical precision of 0.48% and 1.10% as compared to 1.00% and 1.67% (inelastic spectrum) and 0.52% and 1.42% (delayed activation spectrum), because there are more counts in the summed spectrum.

Gamma ray peaks will obviously have the best statistical precision if the counts recorded at all times are summed. However, when there are times where counts are produced by more than a single reaction on a single element, there is no longer a linear

relationship between the counts in the peak and the concentration of a single element. To get the most accurate result for an element's concentration, it is thus necessary to remove all of the counts measured at times when they can be produced by multiple reactions or by different elements (see Table 2).

While this procedure may reduce the statistical precision somewhat, it significantly improves the accuracy, which would otherwise be deteriorated by assigning counts to the wrong element. This problem can be seen when looking at the data for the 1779 keV peak in Table 3. One would like to have the 1779 keV peak that occurs during the high-energy neutron pulse be only due to silicon. However, there is also a peak at the same energy that is due to the delayed activity of aluminum. Since delayed activity peaks are present at all times, if these counts were not subtracted from the peak measured during the high-energy neutron pulse, the derived elemental concentration would be much too high. This effect can be seen in the data in Table 3.

If we did no time gating and assumed that the 1779 peak was only due to silicon, we would have 90480 +/- 0.48% counts and for oxygen at 6129 keV we would have 19920 +/- 1.1% counts. The Si/O ratio would then be about 4.5. Even rudimentary time gating changes the results to 31730 +/- 1% and 10900 +/- 1.67% counts respectively, by selecting only the counts in the inelastic window. The ratio of the 1779 to the 6129 is now ~ 3 rather than 4.5, much closer to the ratio expected from the elemental abundances. If we further correct the counts in the inelastic window by the contribution from the delayed activity, the areas become 26273 +/- 1.2% and 10045 +/- 1.8% counts for the 1779 and 6129 keV peaks respectively, and the ratio of Si to O is now further reduced to about 2.5. This improved accuracy is obtained with only minor deterioration

in the percent error that is purely the precision of the measurement. (Note: The actual Si/O ratio is approximately 0.5, however, the energies of the lines used to determine the Si and O content are of sufficiently different energies that the detector efficiency differs by a factor of four, thus increasing the measured value from ~0.5 to >2.)

The use of optimized time windows allows us to obtain the most statistically precise measure of the delayed activity so that we can retain the best possible precision for the net peak counts while substantially improving on the accuracy of the measured elemental concentration. Once the counts in a peak are known to only be due to a single element and type of reaction, MCNPX calculations can accurately relate the counts to elemental concentration. It is also worth noting that the half lives of the delayed activations are typically at least 1000 times longer than the neutron period, so they can be considered to be constant during the neutron generator pulse period, as assumed in the above analysis, eliminating the need to even correct for the half lives.

Identifying and Removing Sources of Systematic Error Using TLIST data

When working with a weak constant neutron source (e.g. from GCRs) there is no need to record event-by-event time and energy data if the data are transferred periodically with reasonable frequency, since each chunk of transferred data can be separately analyzed to identify a problem with the instrument, e.g. deteriorated resolution, and removed without compromising the entire concatenated data set. However, it is still difficult to determine if the collected data have been compromised due to other errors. These difficulties can be mitigated for the case of *in situ* gamma-ray and neutron spectroscopy measurements with the PING instrument, since it takes advantage of a

pulsed neutron generator synchronized with gamma ray and neutron detector data acquisition combined with the ability to post-process acquired time-tagged event-by-event data.

A unique benefit of incorporating a pulsed neutron generator with a time-tagged event-by-event data acquisition system is that regions in time containing suspicious data can be isolated and removed from the data set for further inspection without affecting the usefulness of the remaining data. Systematic errors in data are nearly impossible to anticipate but often can be identified when examining the post-processed data. Examples include systematic errors caused by equipment operating parameter changes, such as temperature effects on a detector response or, as illustrated in the data shown in Table 4 below, changes in the time-dependence of the turn on of neutron-induced gamma-ray flux that occurs during the PNG burst period.

Table 4. Fast neutron induced count rate and uncertainty for the 6129 keV $^{16}\text{O}(n,n'\gamma)$ gamma-ray peak for ten time slices during the PNG pulse.

Time Slice	Time Range (μs)	Count Rate (cts/μs)	Uncertainty (cts/μs)
1	0 – 10	9	± 1
2	10 – 20	55	± 4
3	20 – 30	41	± 3
4	30 – 40	42	± 3
5	40 – 50	39	± 3
6	50 – 60	42	± 3
7	60 – 70	41	± 3
8	70 – 80	41	± 3
9	80 – 90	46	± 3
10	90 - 100	45	± 3

We demonstrate the merit of saving event-by-event time and energy data with our analysis of the gamma-ray count rate of the 6129 keV peak from neutron inelastic scattering on ^{16}O for a 2-hr live time gamma-ray acquisition by the PING instrument set-

up on the basalt monument. Since the neutron inelastic scattering gamma-ray production rate is proportional to the fast neutron flux, we assume that a stable gamma-ray count rate can be obtained from the time the “pulse start” signal is given to the PNG ion source ($t = 0 \mu\text{s}$). We can examine the time dependence of the fast neutron-induced gamma-ray flux from the time of the “pulse start” signal to the end of the PNG pulse ($t = 0$ to $100 \mu\text{sec}$) to look for anomalies.

In this example, we generated gamma-ray energy spectra for each of ten time slices (time slice width = $10 \mu\text{s}$) of the gamma-ray data during the PNG pulse and determined the 6129 keV net gamma-ray peak count rate and its associated uncertainty for each time slice. Table 3 lists the time range for each time slice, the 6129 keV peak count rates and the uncertainty in the count rates for each of the ten time slices. Note that the count rates in the first and second time slices are inconsistent with the count rates in the 8 other time slices and that the count rate for these later 8 time slices is constant as expected.

The low 6129 keV gamma-ray count rate during the first time slice ($t = 0\text{-}10 \mu\text{s}$) indicates that the PNG has not begun producing fast neutrons yet, since there is a delay between the time that the PNG is sent the “burst on” command signal and the time when fast neutrons are actually being generated by the PNG. The higher 6129 keV gamma-ray count rate in the second time slice ($t = 10\text{-}20 \mu\text{s}$) is also inconsistent with the average value for the other slices and may be due to a systematic error induced by the gamma-ray detector electronics. In both cases, we can choose to exclude these data points from further analysis, since they are not representative of the constant inelastic gamma-ray flux during the PNG pulse. The number of neutrons produced between bursts is negligible.

The PNG is designed to have a well-defined, repeatable neutron burst shape with a sharp 14.1 MeV neutron cutoff between bursts that enables optimum timing of the inelastic and capture measurements and a capture measurement uncontaminated by inelastic gamma rays[67],[68].

To be sure, we would investigate the origin of the systematic errors that prompt us to remove the data from the main analysis. Without this event-by-event time and energy data, however, these points would have been unexamined and included in the data, skewing the results. Excluding the data from the first 20 μs will increase the statistical error on the mean value of the 6129 keV gamma-ray production rate, but will result in more accurate data that we can use to infer the bulk elemental composition of planetary material. This is clearly seen by comparing the 6129 keV weighted mean count rate and uncertainty for time slices 3 through 10 ($t = 20 - 100 \mu\text{s}$) which is $42.1 \text{ cts}/\mu\text{s} \pm 1.10 \text{ cts}/\mu\text{s}$ versus the 6129 keV weighted mean count rate and uncertainty for time slices 1 through 10 ($t = 0 - 100 \mu\text{s}$) which is $40.1 \text{ cts}/\mu\text{s} \pm 0.82 \text{ cts}/\mu\text{s}$. The difference between these two averages is two times the statistical uncertainty, resulting in a systematic error that would compromise the accuracy of derived elemental concentrations.

Energy Calibrating Spectra Using Igor Pro 6.2 Software

PING time-sliced TLIST data are analyzed by using the Igor Pro 6.2 Software and procedures created by Dave Hamara at the University of Arizona in Tucson, Arizona. The raw TLIST data are initially processed to obtain γ -ray spectra in different time regimes, e.g. inelastic scattering, capture, delayed activation and natural activity time-windows, relative to the neutron pulse to minimize spectral interferences. This is done,

because some spectral interference can be eliminated by subtracting peaks in one region from the same peak in other regions to eliminate contributions when the same energy peak can be created from a different element. Each set of data for a defined time-window acquired on a physical rock configuration with the same PING prototype set-up, is then individually energy calibrated and interpolated to put all spectra on the same energy scale using Igor. Each spectrum is individually calibrated, because of the different outdoor conditions that occur due to variations in temperature, humidity during different times of day and time of year that data were collected. The basic energy calibration for each spectrum for a particular PING experiment and time window is done as follows (specific command line details can be found in Appendix III):

- 1) The counts column in each time-slice spectrum is loaded into an Igor profile table and assigned a wave name that refers to the spectrum's date and file number (i.e. s_name1, s_name2, etc.)
 - Under the "Data" menu, select Load Waves > Load General Text...

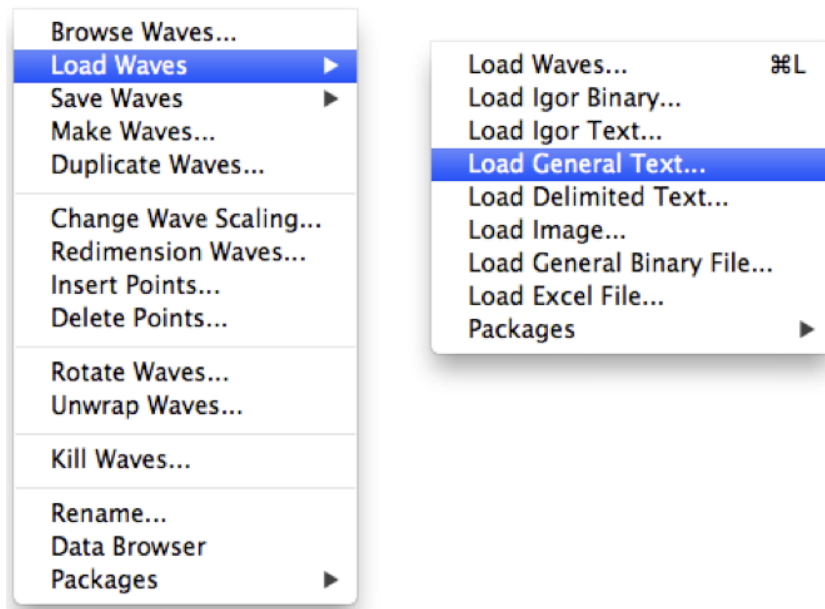


Figure 19. Image of the Data and Load Waves menu files in Igor.

- Load a new filtered gamma-ray spectrum file from your computer.

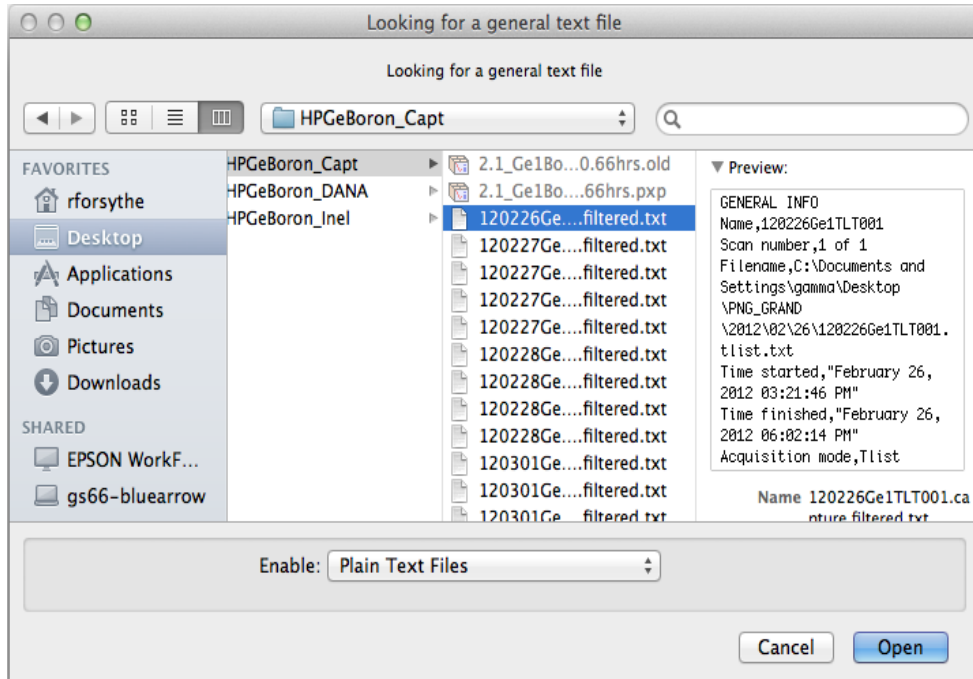


Figure 20. Image of the Load General Text window.

- Skip the first two columns and name the last column as seen above.

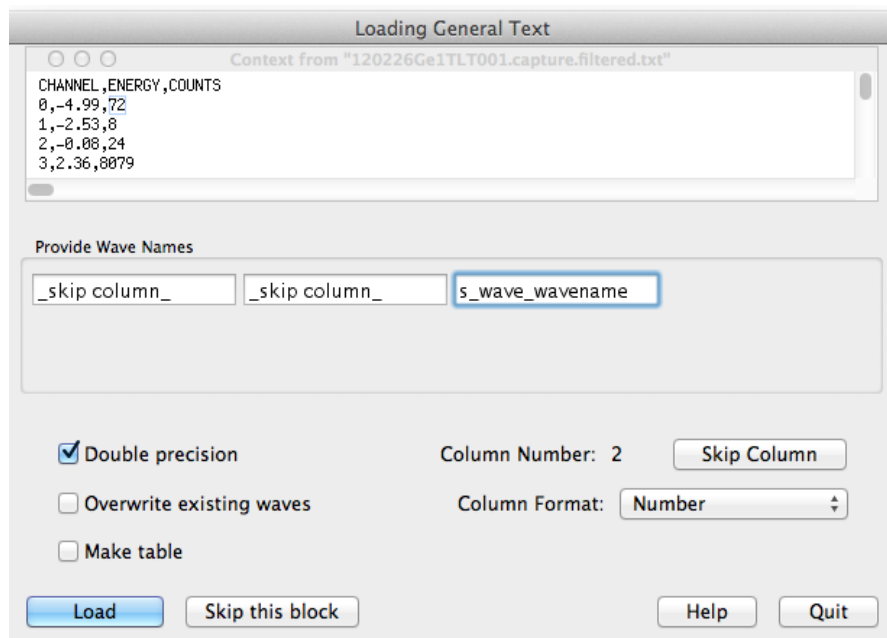


Figure 21. Image of the Loading General Text window.

2) Four gamma ray peaks, the 1779, 5107, 5618, and 6129 keV lines, are fit using Hamara's Fit Gauss with Tail Igor routine to determine the centroid channel for each energy peak.

- Under the "Gamma" menu, select "Fit Gauss With Tail".

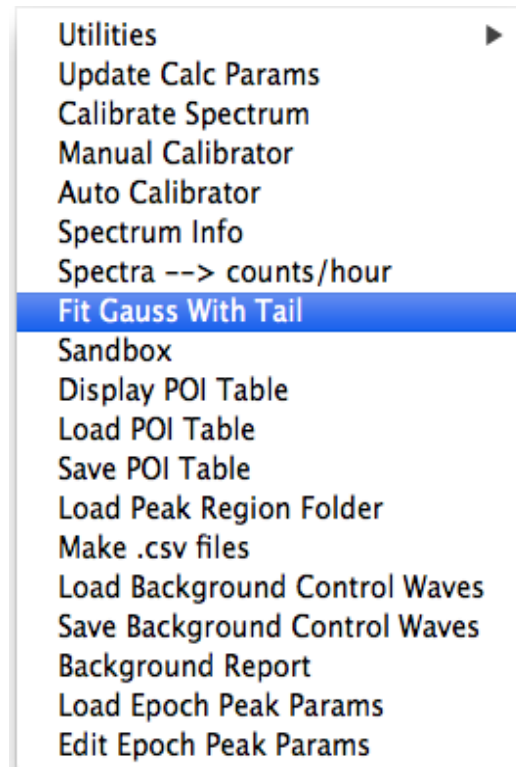


Figure 22. Image of the Gamma menu.

- Under the “Spectrum” menu, select your wave.

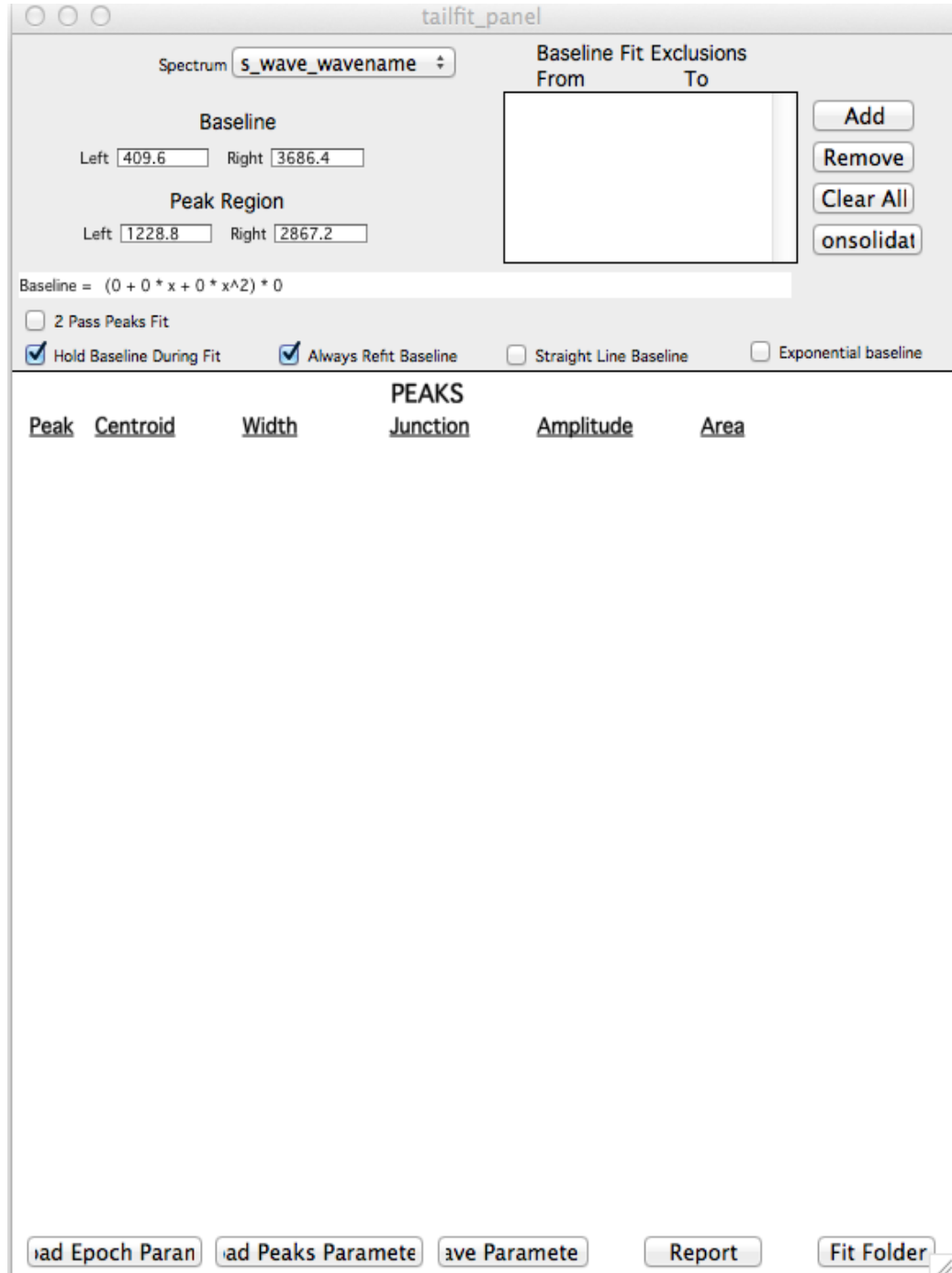


Figure 23. Image of the Fit Gauss With Tail window.

- On the graph, zoom in close to desired peak, with purple cursors as close to peak as possible, and blue cursors fitting the trend of the background. If cursors are not visible on screen, click “Get Cursor”. Then, select the round cursor at the bottom left of the screen, and drag it to the peak, so your window resembles the above image

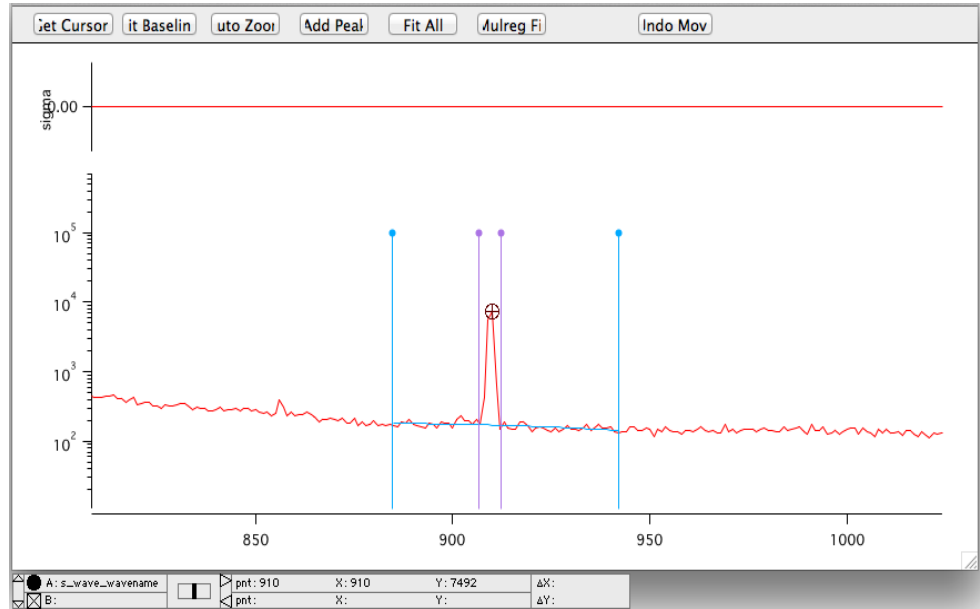


Figure 24. Fit Gauss With Tail gamma-ray spectrum window.

- Click “Add Peak”; if a different peak type is desired, select it here. Additionally, if the user wishes to account for a Doppler-broadened peak, select the checkbox. If not, click OK.

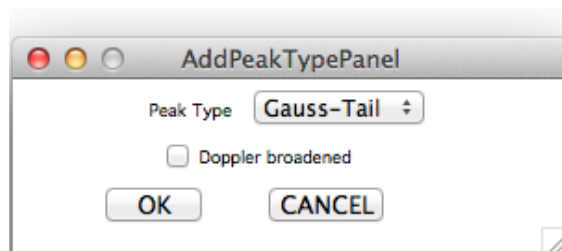


Figure 25. Add Peak Type window.

- Under “Centroid” and “Width”, set both options to “Free” and set “Junction” to “Fixed” and enter in a value of -100.

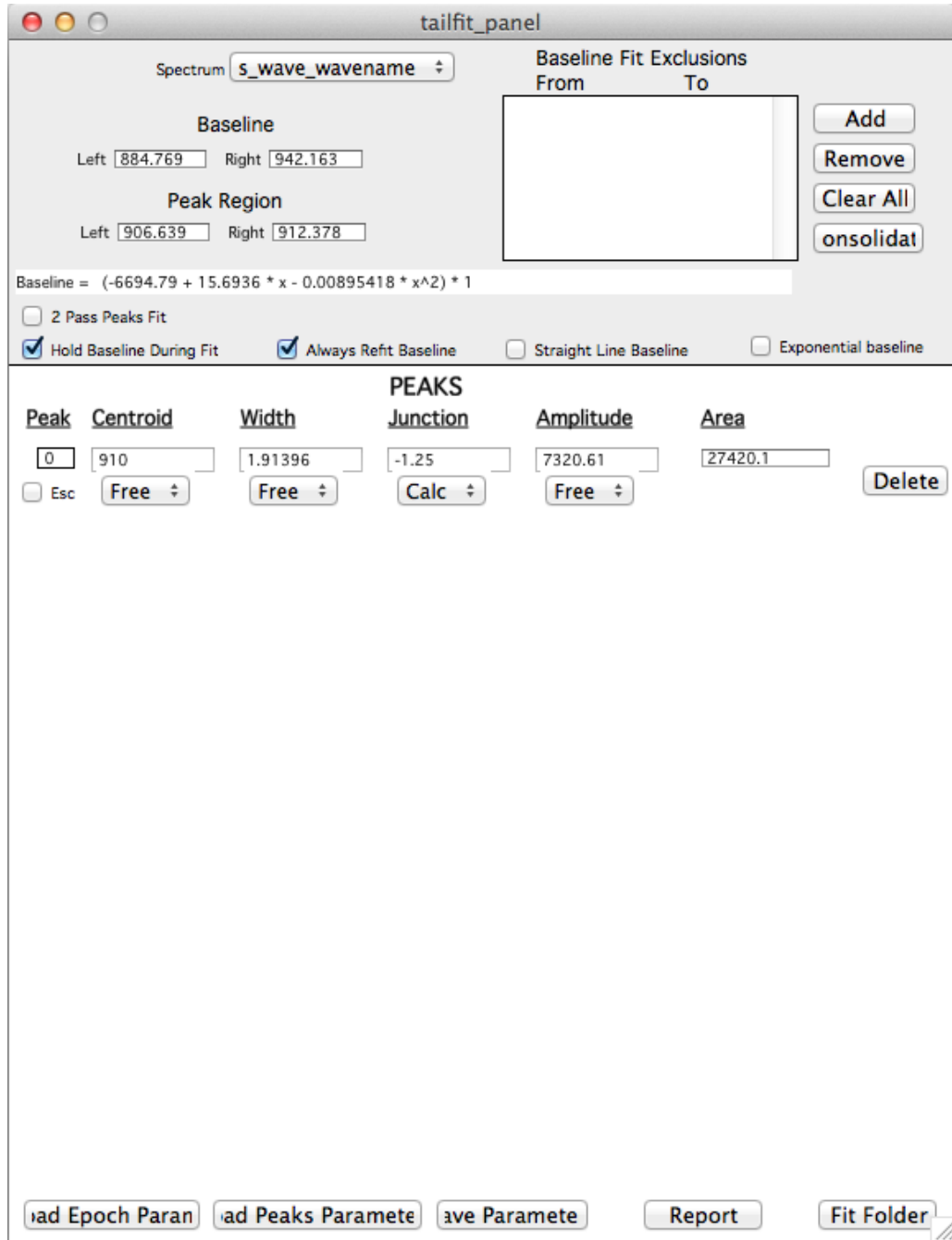


Figure 26. Peak parameter values for the new peak added in the Fit Gauss With Tail panel.

- On the graph, click “Fit All”.

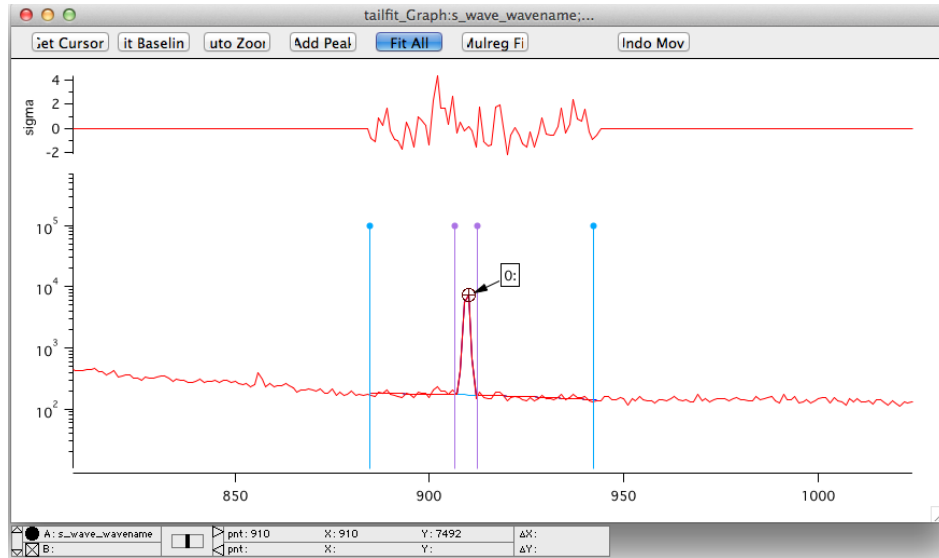


Figure 27. Selecting the Fit All button the Fit Gauss With Tail spectrum graph.

- Under each option, set status to “Fixed”.

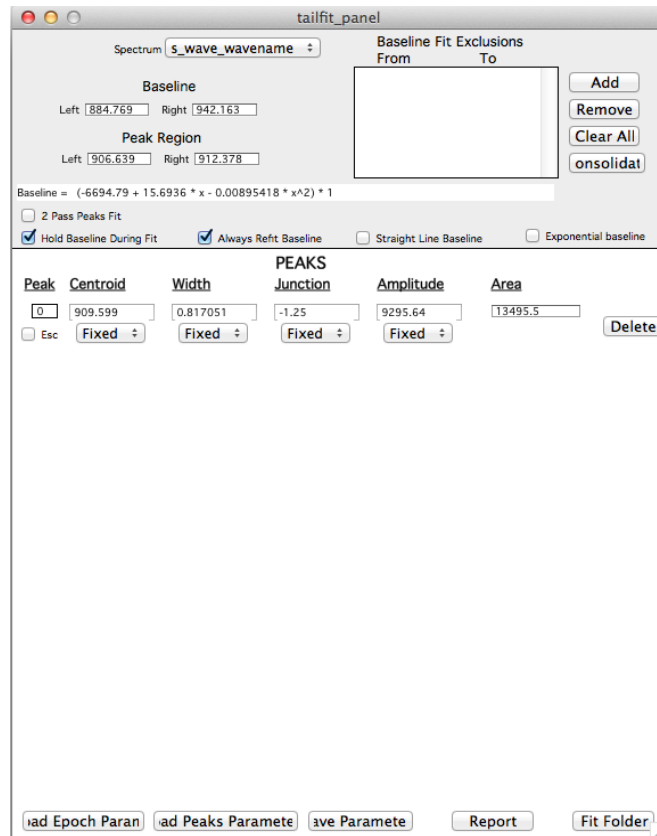


Figure 28. Setting all of the peak parameters to Fixed.

- Repeat for all four energies (eg 1779, 5107, 5618, 6129). When finished, select “Report” at the bottom of the tail_fit window.

The screenshot shows a window titled "Compact_Param_Report" with a table of peak data. The table has columns for Peak, Source, Centroid, Centroid Sigma, Area, Area Sigma, and Width. The data is as follows:

Peak	Source	Centroid	Centroid Sigma	Area	Area Sigma	Width
12/20/2012 15:31:01		-1.000	s_wave_wavename			Rob was here!
Peak 0	909.5991	Fixed	13495.525	Fixed	0.8170512	
Peak 1	2089.0000	Fixed	1032.84878	Fixed	2.470864	
Peak 2	2298.0000	Fixed	1298.37902	Fixed	2.569585	
Peak 3	2507.0000	Fixed	1388.98895	Fixed	2.668306	

Figure 29. Image of the Compact Parameter Report window.

- Copy the data from the Compact_Param_Report window and put it into an Excel file. Copy the information in the third column (under “Centroid”).

The screenshot shows an MS Excel spreadsheet with the following data in the first four rows:

	A	B	C	D	E	F	G	H	I	J	K	L	M	N	O
1	Peak 0	909.5991	Fixed	13495.525	Fixed	0.8170512	Fixed	-1.25	Fixed	1.36048	1.3605	2.4796	Gauss-Tail		
2	Peak 1	2089	Fixed	1032.84878	Fixed	2.470864	Fixed	-1.25	Fixed	4.114259	4.3748	9.9974	Gauss-Tail		
3	Peak 2	2298	Fixed	1298.37902	Fixed	2.569585	Fixed	-1.25	Fixed	4.27864	4.595	10.606	Gauss-Tail		
4	Peak 3	2507	Fixed	1388.98895	Fixed	2.668306	Fixed	-1.25	Fixed	4.443022	4.8206	11.232	Gauss-Tail		

Figure 30. Example of a MS Excel file with the copied report.

3) The energy and corresponding centroid channel are entered into a new Igor table, an XY graph is created of channel vs. energy, and a straight line ($y = mx + b$) is fit to the points, where m = gain and b = offset.

- Under “Windows”, select “New Table”.

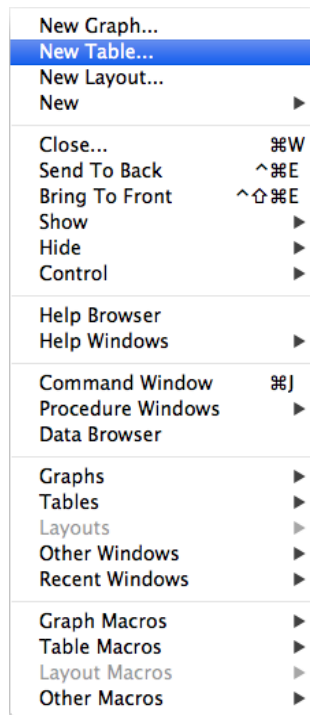


Figure 31. Image of Windows panel in Igor.

- Under the first column, enter the relevant energies. This will be your Y-Axis.

Point	wave0
0	1779
1	5107
2	5618
3	6129
4	

Figure 32. Image of the gamma-ray energy list in the new table.

- After the energy values are entered, right-click on “wave0” and Rename the wave to “Energy”.

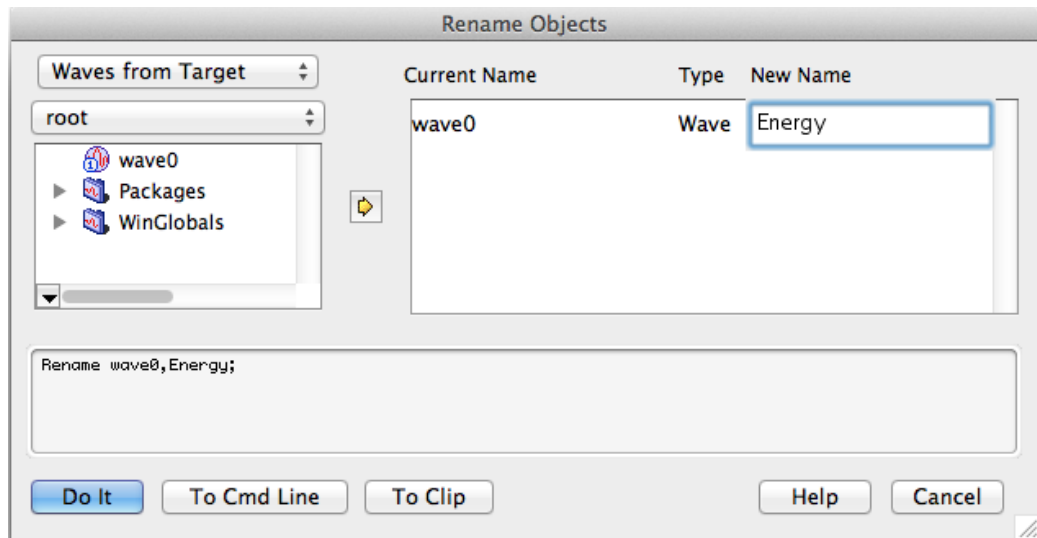


Figure 33. Image of the Rename Objects window in Igor.

- In the second column, paste the values copied from the excel file - these will be your “Channels”; rename the column appropriately.

Point	Energy	wave0		
0	1779	909.599		
1	5107	2089		
2	5618	2298		
3	6129	2507		
4				

Figure 34. Image of the gamma-ray channel list in the new table.

- After both columns are named, create a new Graph by selecting “New Graph” under the “Windows” menu. Under the Y Wave(s) column, select “Energy”. Under the X Wave column, select “Channel”.

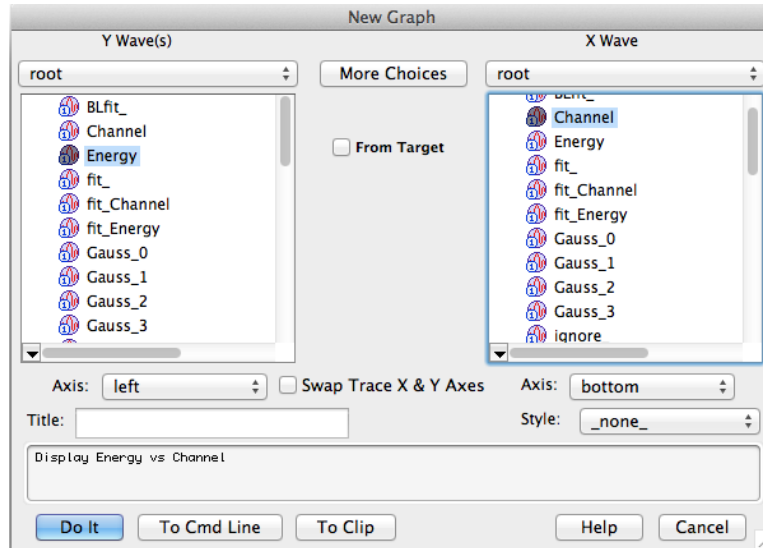


Figure 35. Image of the New Graph panel.

- 4) A new energy-scaled spectrum (wave) is created with the applied energy calibration.
 - Under the “Analysis” menu, select “Curve Fitting...”.

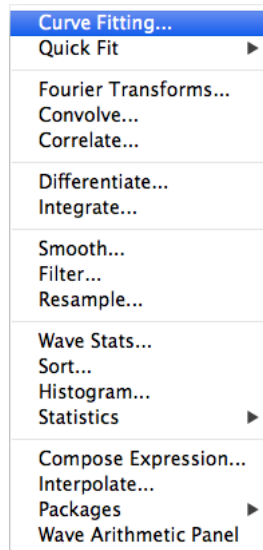


Figure 36. Image of the Analysis menu.

- Set “Function” to “line”, “Y Data” to “Energy”, and “X Data” to “Channel”. The resulting graph(s) are your original line and the curve that fits your data!

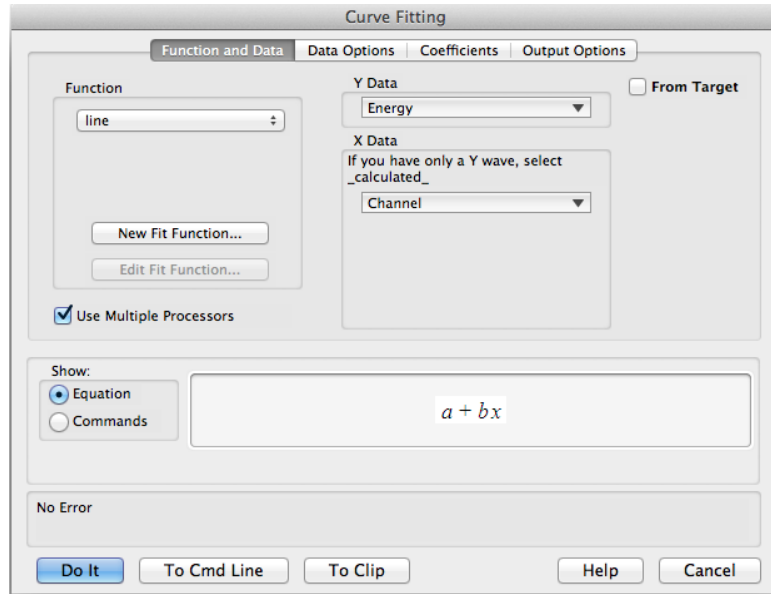


Figure 37. Image of the Curve Fitting panel.

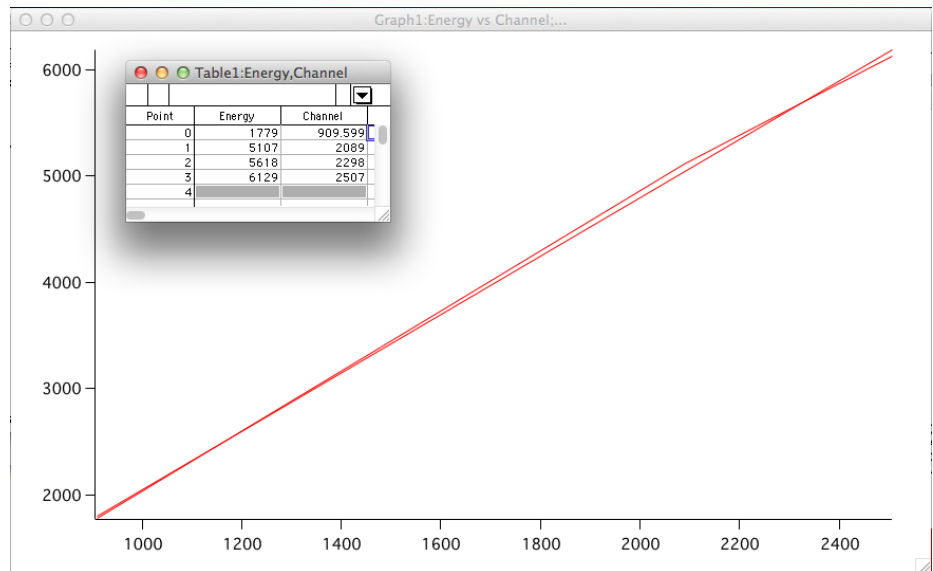


Figure 38. Image of the Curve Fitting graph.

- 5) The preceding steps are repeated for all spectra for each particular time window for each PING experiment configuration.

Putting Energy Calibrated Spectra on One Energy Scale Using Igor Pro 6.2

Each set of spectra for a given configuration and time window is put on one energy scale, using a linear calibration that worked well for the data sets considered so there was not need to consider higher-order polynomials, and then summed together to increase the total number of counts and precision of the gamma-ray lines. This is accomplished by using the Igor interpolate2 function. Let ywave1, ywave2, ywave3, etc. represent the 1-D spectral arrays (waves) that were individually calibrated for one configuration and time window and xwave1, xwave2, xwave3, etc. represent the waves that contain the energy scale for their corresponding spectra counts. We use the interpolate2 Igor Pro routine to create ywave2_interp so that it has the same number of bins (points) as ywave1, and corresponds to the spectral counts in xwave1. In other words, the ywave_interp waves are shifted to a specified energy scale.

In this use of Interpolate2 the destination XY pair is ywave2_interp vs xwave1. So xwave1 is the destination X wave. By setting /I=3, we specify that the interpolation be done at the X values specified by the destination X wave. The destination X wave is therefore not changed. The destination X wave must already exist. The destination Y wave will be set by Interpolate2 to the same number of points as the destination X wave. Table 5 shows the single energy calibration for the Basalt, Granite, and Asteroid Simulant configurations below.

Table 5. Energy Calibrations for Summed Time-Sliced Granite, Basalt, and Asteroid Simulant Configurations Data using HPGe Bare and Boron-Wrapped Detector.

Bare Asteroid Inelastic	<i>Energy Scale: 120329Ge1TLT001.2.inelastic.filtered.txt</i> <i>Equation:</i> -0.9513+2.4441*p
Bare Asteroid Capture	<i>Energy Scale: 120329Ge1TLT001.2.capture.filtered.txt</i> <i>Equation:</i> -0.45904+2.4441*p
Bare Asteroid Delayed Activation & Natural Activity	<i>Energy Scale: 120329Ge1TLT001.2.DANA.filtered.txt</i> <i>Equation:</i> -0.52955+2.4439*p
Boron Asteroid Inelastic	<i>Energy Scale: 110824Ge1TLT003.inelastic.filtered.txt</i> <i>Equation:</i> -0.20147+3.0533*p
Boron Asteroid Capture	<i>Energy Scale: 110824Ge1TLT003.capture.filtered.txt</i> <i>Equation:</i> 0.25758+3.0531*p
Boron Asteroid Delayed Activation & Natural Activity	<i>Energy Scale: 110824Ge1TLT003.DANA.filtered.txt</i> <i>Equation:</i> 0.03963+3.0534*p
Granite Inelastic	<i>Energy Scale: 121102Ge1TLT001.1.inelastic.filtered.txt</i> <i>Equation:</i> -0.5414+2.4542*p
Granite Capture	<i>Energy Scale:</i> 121102Ge1TLT001.1.capture.filtered.txt <i>Equation:</i> -0.41936+2.4542*p
Granite Delayed Activation & Natural Activity	<i>Energy Scale:</i> 121102Ge1TLT001.1.DA.filtered.txt <i>Equation:</i> -0.43537+2.4542*p
Basalt Inelastic	<i>Energy Scale:</i> 110821Ge1TLT005.1.inelastic.filtered.txt <i>Equation:</i> 0.84505+3.0542*p
Basalt Capture	<i>Energy Scale:</i> 110821Ge1TLT005.1.capture.filtered.txt <i>Equation:</i> -0.7496+3.0546*p
Basalt Delayed Activation & Natural Activity	<i>Energy Scale:</i> 110821Ge1TLT005.1.DA.filtered.txt <i>Equation:</i> 0.0073299+3.0539*p

Gamma Ray Peak Fitting Using the Fit Gauss with Tail Igor Pro Function

Each peak in the gamma-ray spectra represents a unique isotope. The area of the peak represents the number of gamma rays detected, which is used to determine how much of that isotope is present. The peaks are fitted using Igor Pro fitting tools to measure the area of each peak and minimize the reduced X^2 and % error of each peak fit.

To perform a peak fitting: Select “Fit Gauss With Tail” (Gamma > Fit Gauss With Tail), and select the wave to fit from the dropdown menu initially labeled “Spectrum”; a graph should then appear. Using the instructions described above, the user should be able to find, add, and fit a peak.

If a user wants to add multiple peaks, they can do so. In order to add multiple peaks, the user should place the purple markers around the edges of all of the peaks they would like to fit, as opposed to just a single peak as described above. Then, place the circle marker on each of the peaks that are to be added, and add them each individually. The user may then fit the peaks to the spectrum one at a time, or all at once – it is at the user’s discretion.

If, at any point, the user needs to ignore a section of the graph in order to more accurately fit a peak – or for any other reason – they can drag the two cursors (the circle and square) from the bottom left section of the graph to the section(s) that they would like to ignore (Circle marks the beginning, square marks the end). Then, moving back to the “tailfit_panel” window, click “Add” under “Baseline Fit Exclusions”. To remove exclusions, simply select the exclusion in question and click “Remove”. For a more detailed view of multiple peak inclusion and baseline inclusion, see Figures 4 and 5

below for visual examples. In order to add, fit, and analyze peaks, see the section entitled “Energy Calibrating Spectra Using Igor Pro 6.2 Software” for more detail.

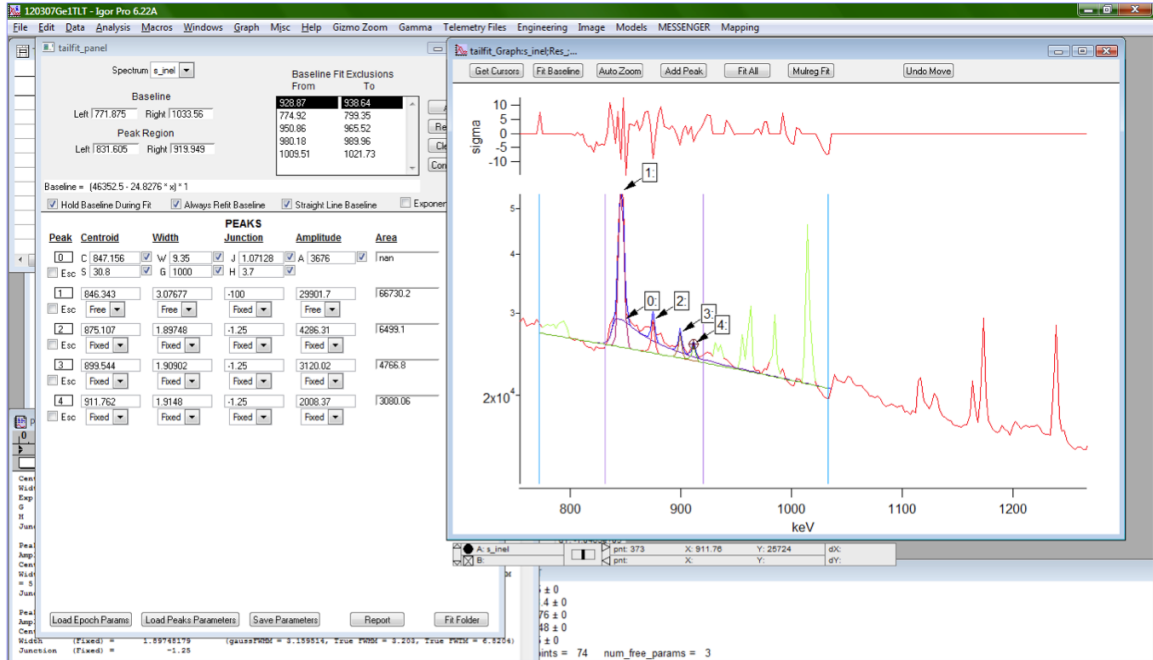


Figure 39. Fitting four peaks on top of a Ge sawtooth peak. Note the better baseline fit (aqua blue lines) due to the exclusion of peaks (lime green) that are not currently being fit in the peak fit window (purple lines).

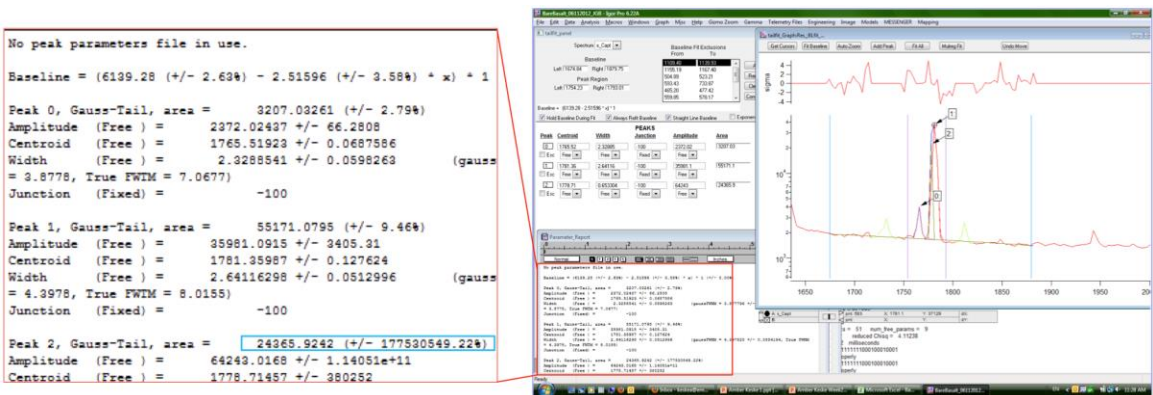


Figure 40. a) (Right) A triple-peak fit with an appropriate baseline. b) (Left) Zoomed in view of the Igor peak fitting report (outlined in red) showing that the Peak 2 area fit (outlined in aqua blue) has a large error and requires adjustments to improve the fit’s accuracy.

Neutron Data Analysis

The work presented in these next two sections is from J. G. Bodnarik, J. S. Schweitzer, A. M. Parsons, L. G. Evans, and R.D. Starr, "PING Gamma Ray and Neutron Measurements of a Meter-Scale Carbonaceous Asteroid Analog Material," 43rd Lunar and Planetary Science Conference, **No. 1544** (2012).

The epithermal and thermal neutron dieaway data can be analyzed to determine the H-content and macroscopic thermal neutron absorption cross-section of the bulk material. The H-content was not determined from the epithermal neutron experimental and MCNPX data due to time constraints, but it will be determined and presented in a publication in the foreseeable future.

We experimentally tested and verified the absorption properties of the granite monument, the basalt monument, and basalt layering asteroid simulant (neutron properties analogous to a CI1 carbonaceous chondrite meteorite) by studying the time profile of thermal neutron absorption between PNG pulses using ^3He thermal neutron detectors at the surface. Figure 6 is a cartoon demonstrating how we can compare the average macroscopic thermal neutron absorption cross-sections of the fitted experiment data to that of the calculated data (from known elemental composition, density, and cross-section information) for the bulk material.

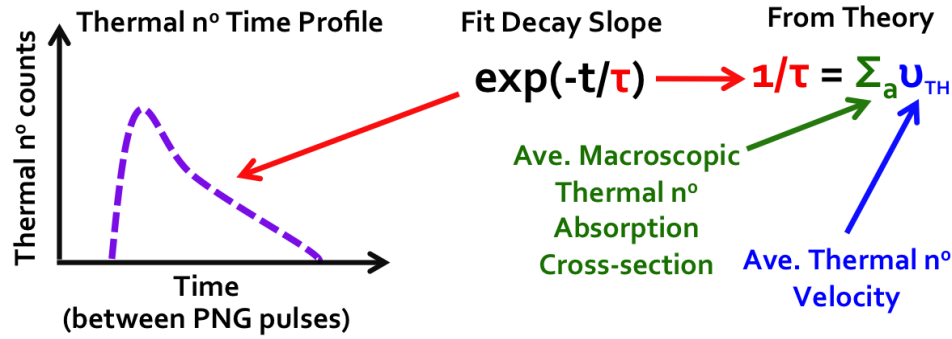


Figure 41. Cartoon illustrating the comparison of the average macroscopic thermal neutron absorption cross-sections from experimental and calculated data.

We calculated the theoretical average macroscopic thermal neutron absorption cross-section (Σ_a) from ACTLabs elemental assay composition of samples of the granite, the basalt, and the CI1 carbonaceous chondrite meteorite, the known material bulk density, and known thermal neutron microscopic absorption cross-sections using the equations in Figure 7.

$$\Sigma_a = \sum_{i=1}^{total \# \text{ elems}} N_i \sigma_i \quad \text{and} \quad N_i = \frac{C_{i^{th} \text{ elem}} \rho_{bulk} N_A}{M_{i^{th} \text{ elem}}}$$

Figure 42. Equations used to calculate the theoretical average macroscopic thermal neutron absorption cross-section for bulk materials[69].

The macroscopic thermal neutron absorption cross-section was determined from the elemental assays of the granite, basalt and CI1 carbonaceous chondrite (analogous to the asteroid simulant) and compared with the results obtained from the fitting of the thermal neutron dieaway data.

The experimental results are compared with the MCNPX results to benchmark the Monte Carlo model, used to obtain the efficiency of the HPGe detector, used to obtain the

absolute elemental weight percent concentrations, used to model the epithermal and thermal neutron dieaway to obtain the H-content and the macroscopic thermal neutron absorption cross-section of the bulk material, and provide a model that can be used to calculate the results for situations where it would be difficult to build an experimental configuration.

MCNPX Data Analysis

MCNPX is a general use Monte Carlo radiation transport code used to track 34 different types of particles (e.g. n, p, e, ...) and 2205 heavy ions for continuous energies from 0-1000 GeV using data libraries below ~150 MeV (n, p, e, and h) and models otherwise. The user can specify the following in the input file: 1) 3-D object geometries using 1st and 2nd degree surfaces, tori, ten macrobodies and lattices; 2) material definitions or vacuum (void) for all defined objects; and 3) interdependent source variables including both time-dependent and time-independent (continuous) sources, 7 output tally types and many modifiers. The computer code can be run on many computer platforms including Linux, Unix, Windows, and OS X (parallel with MPI).

MCNPX is the next evolution in a series of Monte Carlo radiation transport codes, based as a superset of MCNP4C, developed nearly sixty years ago and still maintained at Los Alamos National Laboratory. The Monte Carlo Neutral Particles code (MCNP), the precursor to MCNPX, is the internationally recognized Monte Carlo code for analyzing the transport of neutrons, gamma rays, electrons, both primary source electrons and

gamma-ray interactions producing secondary electrons, and coupled transport, e.g. secondary gamma ray transport resulting from neutron interactions^[2].

Geometry and VISED

MCNPX is a three-dimensional Monte Carlo computer model in which the user can model neutron, gamma-ray, and X-ray transport, using defined cross-sections libraries provided in the code, in a virtually defined environment. The user can specify, in an input deck, a source, detector, objects and their geometries, material specifications, and elemental compositions as well as the desired flux tally outputs for defined objects. Input decks were created using the Visual Editor (VISED)[70], created by Randy Schwarz is an interactive graphical user interface tool that makes it easier to create and display objects, geometries, materials, transformation, sources, and tally plots, and the input deck to run using MCNPX.

Configurations Modeled and Approximations That Were Made

I used the MCNPX Visual Editor Version X_24E to create the two input scripts each for the granite monument, basalt monument and asteroid simulant configuration input files. The first input script for each of the three configurations described the geometries (physical dimensions of the objects in the model including the PNG, HPGe detector and the basalt, granite or asteroid monuments), material definitions (e.g. ActLabs elemental assay of basalt, granite, or asteroid simulant composition, HPGe detector crystal, and other objects), importances (e.g. neutron and/or photon importance for each object in the computer simulation), the PNG neutron source, HPGe detector, and the F2

output surface tally (units=particle/cm² normalized to one input particle, e.g. photons/cm²/neutron) for the HPGe detector crystal surface. These models simulated 14 MeV neutrons generated from the PNG (which was set a point source without any housing) from 0-100 μs, neutron transport from the PNG and resultant generation of gamma rays produced from neutron-nuclei interactions in the probed material configuration (e.g. basalt monument, granite monument, or asteroid simulant layered configuration) and air, and the resulting gamma rays that reached the surface of the HPGe detector (HPGe bare crystal only, no housing). Figures 8 shows the geometry and spacing of the PNG point source and HPGe crystal on each of the material configurations.

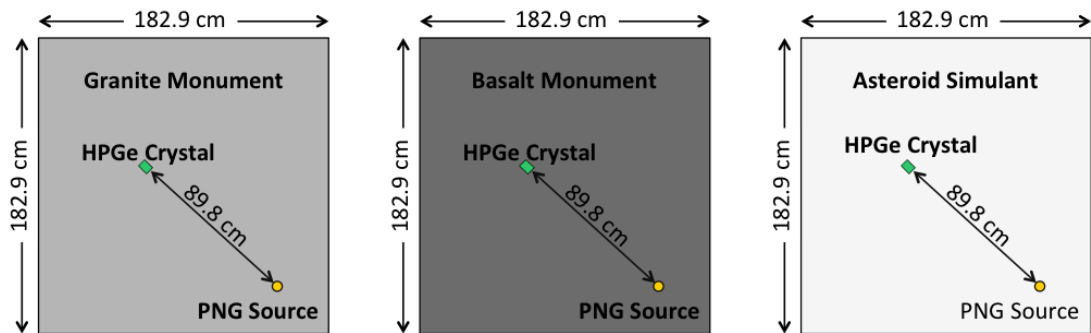


Figure 43. Aerial view of MCNPX geometry and space of HPGe crystal and PNG source point on top of the granite, basalt, and asteroid layering simulant configurations.

The second input script used the F2 tally surface tally of the HPGe detector crystal surface to define the input gamma-ray energies and intensities for the cylindrical, gamma-ray beam source that is aimed axially at the HPGe detector crystal to determine the gamma ray efficiency of the detector for different gamma-ray line energies by providing a F8 pulse height tally (units=energy/volume normalized to one input particle,

e.g. MeV/cm³/photon) for the gamma rays detected in the volume of the HPGe detector crystal.

The first input scripts were run for ~50 hrs each on 128 processors on the NASA Center for Climate Simulation (NCCS) Discover cluster Westmere for a total number of particles of 2×10^{10} neutrons per script using MCNPX version 2.6F (March, 2008) and the associated data and cross-section libraries. The second input scripts were run for ~15 minutes each on 1 processor on an HP Pavillion Elite HPE with an AMD Phenom™ II X6 1060T 3.20 GHz processor, 16.0 GB RAM and a 64-bit operating system running Windows 7 Ultimate Service Pack 1.

Analyzing MCNPX Output

The gamma-ray net peak areas and uncertainties for F2 and F8 tallies are determined by analyzing the data in the same way that experimental gamma-ray data is analyzed in the *Gamma Ray Peak Fitting Using the Fit Gauss with Tail Igor Pro Function* section of this chapter. Once the net peak areas and uncertainties are determined for the F2 and F8 tallies, the detector efficiency for a gamma-ray peak energy is calculated by taking the ratio of the F8 tally/F2 tally net peak areas and the uncertainty is calculated by taking the square root of the sum of the square of the uncertainties. It is useful to note that the F8 tally gamma-ray spectra only include inelastic scattering and thermal neutron capture gamma rays, since MCNPX does not calculate gamma rays from natural radioactivity or delayed activation.

CHAPTER IV

RESULTS AND INTERPRETATION

Some of the gamma-ray results presented in this chapter will appear in the peer-reviewed publication Parsons, A., Bodnarik, J., Evans, L., Nowicki, S., Schweitzer, J., Starr, R., “Subsurface *In Situ* Elemental Composition Measurements with PING,” Proceedings of the 2013 IEEE Aerospace Conference, in press. Some of the neutron results presented in this chapter are from the peer-reviewed publication J. G. Bodnarik, J. S. Schweitzer, A. M. Parsons, L. G. Evans, and R.D. Starr, “PING Gamma Ray and Neutron Measurements of a Meter-Scale Carbonaceous Asteroid Analog Material,” 43rd Lunar and Planetary Science Conference, **No. 1544** (2012).

PING was tested on a total of 10 experimental rock configurations, summarized in Table 1 of Chapter II and provided in more detail in Appendix II, to determine the sensitivity to biogenic precursor elements (e.g. C, O, and H) and rock forming elements (e.g. C, H, O, Si, Ca, Fe, Al, Mg, K, Th, and U) necessary to unveil the volatile and organic nature, and basic geochemistry of C-type asteroids. Determining the elemental concentrations as well as subsurface features in these most primitive asteroids will aid in answering important questions about the early history, formation and evolution of the Solar System and Earth.

While not all of the experimental data collected with PING for these 10 configurations have been analyzed in this thesis, the data are summarized in Appendix II. Instead, only the granite monument, basalt monument, and asteroid simulant configurations were selected for analysis. These configurations were strategically

selected, because one must understand the bulk properties of our selected granite and basalt standards before one can interpret results from more complex layering configurations using basalt, granite and polyethylene materials. The additional data collected for the remaining 7 configurations will be presented in future journal article publications.

The gamma-ray and neutron experimental and MCNPX data were analyzed to determine the ratios of H, C, O, Mg, Na, Al, Fe, and Ca to Si from the gamma-ray data, and determine the macroscopic thermal neutron absorption cross-section from the thermal neutron dieway. The H-content was not determined from the epithermal neutron experimental and MCNPX data, but it will be determined and presented in a publication in the foreseeable future.

Results and Interpretation

Gamma Ray

H, C, O, Mg, Na, Al, Si, Fe, Ca, K, Th, and U gamma-ray lines were analyzed in the experimental and MCNPX data for all three configurations. These elements were chosen, because they are major rock forming elements. Due to their difference in concentration between both the granite and basalt monuments, they are useful in differentiating between different types of asteroids. Table 6 shows the selected, independently assayed, element concentrations (wt%) for the granite, the basalt, and the C11 carbonaceous chondrite meteorite, analogous to a C-type asteroid and used to determine and construct the asteroid simulant-layering configuration that has the same neutron transport properties as this meteorite.

Table 6: Granite, basalt, CII chondrite meteorite element concentrations.

Element	Granite (wt%)	Basalt (wt%)	CII chondrite (wt%)
H	0.09	0.03	2.02
C	0.03	0.03	3.45
O	48.33	44.97	46.40
Na	2.27	2.45	0.50
Mg	0.17	4.79	9.70
Al	7.40	8.64	0.87
Si	34.23	23.18	10.64
Ca	0.63	6.62	0.96
Fe	1.14	7.34	18.20
K	4.32	1.15	0.06
Th	2.43E-03	5.00E-06	2.90E-06
U	1.39E-03	7.20E-05	8.00E-07

H, C, O, Mg, Na, Al, Si, Fe, Ca, K, Th, and U gamma-ray lines were analyzed in the experimental data for the granite, basalt and asteroid simulant and are presented in Tables 7, 8 and 9. Tables 7, 8, and 9 are divided into four major sections: the gamma-ray line energy, E in units of keV, and three time windows during the 1000 μ s PNG pulse period. Each time window section lists the corresponding gamma-ray line identification, gamma-ray line intensity, I_g in units of counts, and the relative gamma-ray line uncertainty, σ in units of percent, for time windows that contain gamma-rays predominately produced by neutron inelastic scattering (window = 10-100 μ s), thermal neutron capture (window = 150-650 μ s), and delayed activation and natural activity (window = 650-1000 μ s). Delayed activation and natural activity gamma-rays are present in all of these time windows over the 1000 μ s neutron pulse period and in some cases gamma-ray capture lines may be present in the inelastic scattering window. A word of caution to the reader about the gamma-ray line identifications: since all possible

gamma ray-producing nuclear reactions have not been explored, some of the gamma-ray line energies in the different time windows may be misidentified.

The 440, 585, 847, 1014, 1460, 1779, 1811, 1942, 2203, 2211, 2223, 2614, 4438, and 6129 keV gamma-ray lines were analyzed for each of the three configurations in Tables 7, 8, and 9. The 440 keV gamma-ray line is most likely produced in the inelastic window by the $^{23}\text{Na}(n,n'\gamma)$ reaction and the delayed activation of $^{69\text{m}}\text{Zn}$, in the capture window by the delayed activation of $^{69\text{m}}\text{Zn}$, and in the delayed activation and natural activity window by the delayed activation of $^{69\text{m}}\text{Zn}$. The 585 keV gamma-ray line is most likely produced in the inelastic window from the excited state of ^{25}Mg ($^{25}\text{Mg}^*$) through the $^{28}\text{Si}(n,\alpha)^{25}\text{Mg}$ reaction, the delayed activation of $^{69}\text{Ge}+\text{K X-ray}$, and the natural activity of ^{228}Th - ^{208}Tl , in the capture window by $^{25}\text{Mg}(n,\gamma)$, the delayed activation of $^{69}\text{Ge}+\text{K X-ray}$, and the natural activity of ^{228}Th - ^{208}Tl , and in the delayed activation and natural activity window by the delayed activation of $^{69}\text{Ge}+\text{K X-ray}$ and the natural activity of ^{228}Th - ^{208}Tl . The 847 keV gamma-ray line is most likely produced in the inelastic window by $^{27}\text{Al}(n,n'\gamma)$ and $^{56}\text{Fe}(n,n'\gamma)$, and the delayed activation of $^{56}\text{Fe}(n,p\beta)^{56}\text{Fe}$, $^{26}\text{Mg}(n,\gamma\beta)^{27}\text{Al}$, and $^{55}\text{Mn}(n,\gamma\beta)^{56}\text{Fe}$, in the capture window by the delayed activation of $^{56}\text{Fe}(n,p\beta)^{56}\text{Fe}$, $^{26}\text{Mg}(n,\gamma\beta)^{27}\text{Al}$, and $^{55}\text{Mn}(n,\gamma\beta)^{56}\text{Fe}$, and in the delayed activation window by the delayed activation of $^{56}\text{Fe}(n,p\beta)^{56}\text{Fe}$, $^{26}\text{Mg}(n,\gamma\beta)^{27}\text{Al}$, and $^{55}\text{Mn}(n,\gamma\beta)^{56}\text{Fe}$. The 1014 keV gamma-ray line is produced in the inelastic window by $^{27}\text{Al}(n,n'\gamma)$ and the delayed activation of $^{26}\text{Mg}(n,\gamma\beta)^{27}\text{Al}$, in the capture window by the delayed activation of $^{26}\text{Mg}(n,\gamma\beta)^{27}\text{Al}$, and in the delayed activation and natural activity window by the delayed activation of $^{26}\text{Mg}(n,\gamma\beta)^{27}\text{Al}$. The 1460 keV gamma-ray line is produced in all three windows by the natural activity of ^{40}K . The 1779 keV gamma-ray

line is produced in the inelastic window by $^{28}\text{Si}(n,n'\gamma)$ and the delayed activation of $^{28}\text{Si}(n,p\beta)^{28}\text{Si}$ and $^{27}\text{Al}(n,\gamma\beta)^{28}\text{Si}$, in the capture window from the delayed activation of $^{28}\text{Si}(n,p\beta)^{28}\text{Si}$ and $^{27}\text{Al}(n,\gamma\beta)^{28}\text{Si}$, and in the delayed activation and natural activity window by the delayed activation of $^{28}\text{Si}(n,p\beta)^{28}\text{Si}$ and $^{27}\text{Al}(n,\gamma\beta)^{28}\text{Si}$. The 1811 keV gamma-ray line is produced in the inelastic window by $^{56}\text{Fe}(n,n'\gamma)$ and the delayed activation of $^{56}\text{Fe}(n,p\beta)^{56}\text{Fe}$ and $^{55}\text{Mn}(n,\gamma\beta)^{56}\text{Fe}$, in the capture window by the delayed activation of $^{56}\text{Fe}(n,p\beta)^{56}\text{Fe}$ and $^{55}\text{Mn}(n,\gamma\beta)^{56}\text{Fe}$, and in the delayed activation and natural activity window by the delayed activation of $^{56}\text{Fe}(n,p\beta)^{56}\text{Fe}$ and $^{55}\text{Mn}(n,\gamma\beta)^{56}\text{Fe}$. The 1942 keV gamma ray line is produced in the inelastic scattering window by $^{41}\text{Ca}(n,n'\gamma)$, and in the capture window by $^{40}\text{Ca}(n,\gamma)$. The 2203 keV gamma-ray line is produced in the capture window and the delayed activation and natural activity window by the delayed activation of ^{238}U - ^{214}Bi . The 2211 keV gamma-ray line is produced in the inelastic window by $^{27}\text{Al}(n,n'\gamma)$. The 2223 keV gamma-ray line is produced in all three windows by $^1\text{H}(n,\gamma)$. The 4438 keV gamma-ray line is produced in the inelastic window by $^{12}\text{C}(n,n'\gamma)$ and $^{16}\text{O}(n,n'\alpha)^{12}\text{C}$. Finally, the 6129 keV gamma-ray line is produced in the inelastic window by $^{16}\text{O}(n,n'\gamma)$ and $^{16}\text{O}(n,p\beta)^{16}\text{O}$, and in the capture window and the delayed activation and natural activity window by the delayed activation of $^{16}\text{O}(n,p\beta)^{16}\text{O}$.

Table 7 lists the intensities and uncertainties of the gamma-ray lines analyzed and their selected timing windows during the PNG 1000 μs period (inelastic window = 10-100 μs , capture window = 150-650 μs , and delayed activation and natural activity = 650-1000 μs) for the PING granite monument experiment that was run for a total acquisition live time of 16.21 hours. Table 8 lists the intensities and uncertainties of the gamma-ray

lines analyzed and their selected timing windows during the PNG 1000 μ s period for the PING basalt monument experiment that was run for a total acquisition live time of 15.23 hrs. Table 9 lists the intensities, and uncertainties of the gamma-ray lines analyzed and their selected timing windows during the PNG 1000 μ s period for the PING asteroid simulant experiment that was run for a total acquisition live time of 46.15 hrs.

Table 7: Gamma-ray line intensities and uncertainties for the PING granite monument data, with the HPGe detector wrapped in a borated-rubber cap, for different timing windows during the PNG pulse period (total acquisition live time = 16.21 hrs). The “*” symbol means that it is the excited state of the isotope, i.e. $^{25}\text{Mg}^*$ means that it is the excited state of ^{25}Mg through the $^{28}\text{Si}(n,\alpha)^{25}\text{Mg}$ reaction.

E (keV)	Inelastic Scattering Window			Thermal Neutron Capture Window			Delayed Activation & Natural Activity		
	ID	Ig (cts)	σ (%)	ID	Ig (cts)	σ (%)	ID	Ig (cts)	σ (%)
440	$^{23}\text{Na}(n,n'\gamma)$ ^{69m}Zn	17456	18.7				^{69m}Zn	1213	16.5
585	$^{25}\text{Mg}^*$ $^{69}\text{Ge}+\text{K}$ $^{228}\text{Th}-^{208}\text{Tl}$	19472	6.30	$^{24}\text{Mg}(n,\gamma)$ $^{69}\text{Ge}+\text{K}$ $^{228}\text{Th}-^{208}\text{Tl}$	38891	0.93	$^{69}\text{Ge}+\text{K}$ $^{228}\text{Th}-^{208}\text{Tl}$	26812	1.18
847	$^{27}\text{Al}(n,n'\gamma)$ $^{56}\text{Fe}(n,n'\gamma)$ $^{56}\text{Fe}(n,p\beta)$ $^{26}\text{Mg}(n,\gamma\beta)$ $^{55}\text{Mn}(n,\gamma\beta)$	99535	0.60	$^{56}\text{Fe}(n,p\beta)$ $^{26}\text{Mg}(n,\gamma\beta)$ $^{55}\text{Mn}(n,\gamma\beta)$	25880	0.89	$^{56}\text{Fe}(n,p\beta)$ $^{26}\text{Mg}(n,\gamma\beta)$ $^{55}\text{Mn}(n,\gamma\beta)$	18158	1.07
1014	$^{27}\text{Al}(n,n'\gamma)$ $^{26}\text{Mg}(n,\gamma\beta)$	56458	0.83	$^{26}\text{Mg}(n,\gamma\beta)$	8519	8.68	$^{26}\text{Mg}(n,\gamma\beta)$	5882	7.87
1460	^{40}K	14574	5.15	^{40}K	135102	0.37	^{40}K	93885	0.44
1779	$^{28}\text{Si}(n,n'\gamma)$ $^{28}\text{Si}(n,p\beta)$ $^{27}\text{Al}(n,\gamma\beta)$	80811	0.56	$^{28}\text{Si}(n,p\beta)$ $^{27}\text{Al}(n,\gamma\beta)$	40554	0.62	$^{28}\text{Si}(n,p\beta)$ $^{27}\text{Al}(n,\gamma\beta)$	28668	0.73
1811	$^{56}\text{Fe}(n,n'\gamma)$ $^{56}\text{Fe}(n,p\beta)$ $^{55}\text{Mn}(n,\gamma\beta)$	41355	0.97	$^{56}\text{Fe}(n,p\beta)$ $^{55}\text{Mn}(n,\gamma\beta)$	723	8.30	$^{56}\text{Fe}(n,p\beta)$ $^{55}\text{Mn}(n,\gamma\beta)$	550	8.81
1942	$^{40}\text{Ca}(n,n'\gamma)$	4179	7.31						
2203				$^{238}\text{U}-^{214}\text{Bi}$	6002	1.85	$^{238}\text{U}-^{214}\text{Bi}$	3987	2.27
2211	$^{27}\text{Al}(n,n'\gamma)$	54186	0.96						
2223	$^1\text{H}(n,\gamma)$	45029	1.27	$^1\text{H}(n,\gamma)$	511	10.7			
2614	$^{228}\text{Th}-^{208}\text{Tl}$	2783	7.94	$^{228}\text{Th}-^{208}\text{Tl}$	26797	0.78	$^{228}\text{Th}-^{208}\text{Tl}$	18979	0.92
4438	$^{16}\text{O}(n,n'\alpha)$	13265	3.77						
6129	$^{16}\text{O}(n,n'\gamma)$ $^{16}\text{O}(n,p\beta)$	23470	0.98	$^{16}\text{O}(n,p\beta)$	5019	1.81	$^{16}\text{O}(n,p\beta)$	3450	2.17

Table 8: Gamma-ray line intensities and uncertainties for the basalt monument data, with the HPGe detector wrapped in a borated-rubber cap, for different timing windows during the PNG pulse period (total acquisition live time = 15.23 hrs). The “*” symbol means that it is the excited state of the isotope, i.e. $^{25}\text{Mg}^*$ means that it is the excited state of ^{25}Mg through the $^{28}\text{Si}(n,\alpha)^{25}\text{Mg}$ reaction.

E (keV)	Inelastic Scattering Window			Thermal Neutron Capture Window			Delayed Activation & Natural Activity		
	ID	Ig (cts)	σ (%)	ID	ID	Ig (cts)	σ (%)	Ig (cts)	ID
440	$^{23}\text{Na}(n,n'\gamma)$ ^{69m}Zn	18392	5.53	^{69m}Zn	2089	7.24	^{69m}Zn	1190	9.46
585	$^{25}\text{Mg}^*$ $^{69}\text{Ge}+\text{K}$ $^{228}\text{Th}-^{208}\text{Tl}$	12322	2.87	$^{24}\text{Mg}(n,\gamma)$ $^{69}\text{Ge}+\text{K}$ $^{228}\text{Th}-^{208}\text{Tl}$	5893	2.24	$^{69}\text{Ge}+\text{K}$ $^{228}\text{Th}-^{208}\text{Tl}$	4300	2.52
847	$^{27}\text{Al}(n,n'\gamma)$ $^{56}\text{Fe}(n,n'\gamma)$ $^{56}\text{Fe}(n,p\beta)$ $^{26}\text{Mg}(n,\gamma\beta)$ $^{55}\text{Mn}(n,\gamma\beta)$	117895	0.51	$^{56}\text{Fe}(n,p\beta)$ $^{26}\text{Mg}(n,\gamma\beta)$ $^{55}\text{Mn}(n,\gamma\beta)$	24065	0.89	$^{56}\text{Fe}(n,p\beta)$ $^{26}\text{Mg}(n,\gamma\beta)$ $^{55}\text{Mn}(n,\gamma\beta)$	16994	1.06
1014	$^{27}\text{Al}(n,n'\gamma)$ $^{26}\text{Mg}(n,\gamma\beta)$	53470	0.81	$^{26}\text{Mg}(n,\gamma\beta)$	7483	2.96	$^{26}\text{Mg}(n,\gamma\beta)$	5399	4.97
1460	^{40}K			^{40}K	28250	0.86	^{40}K	19637	1.00
1779	$^{28}\text{Si}(n,n'\gamma)$ $^{28}\text{Si}(n,p\beta)$ $^{27}\text{Al}(n,\gamma\beta)$	58050	0.68	$^{28}\text{Si}(n,p\beta)$ $^{27}\text{Al}(n,\gamma\beta)$	27212	0.78	$^{28}\text{Si}(n,p\beta)$ $^{27}\text{Al}(n,\gamma\beta)$	19156	0.92
1811	$^{56}\text{Fe}(n,n'\gamma)$ $^{56}\text{Fe}(n,p\beta)$ $^{55}\text{Mn}(n,\gamma\beta)$	43720	0.90	$^{56}\text{Fe}(n,p\beta)$ $^{55}\text{Mn}(n,\gamma\beta)$	826	6.37	$^{56}\text{Fe}(n,p\beta)$ $^{55}\text{Mn}(n,\gamma\beta)$	649	6.63
1942	$^{40}\text{Ca}(n,n'\gamma)$	3623	7.40		361	11.8			
2203				$^{238}\text{U}-^{214}\text{Bi}$	360	14.5	$^{238}\text{U}-^{214}\text{Bi}$	305	12.2
2211	$^{27}\text{Al}(n,n'\gamma)$	53265	0.95						
2223	$^1\text{H}(n,\gamma)$	43443	1.26	$^1\text{H}(n,\gamma)$	748	8.60			
2614	$^{228}\text{Th}-^{208}\text{Tl}$			$^{228}\text{Th}-^{208}\text{Tl}$	3298	2.45	$^{228}\text{Th}-^{208}\text{Tl}$	2311	2.84
4438	$^{16}\text{O}(n,n'\alpha)$	11089	4.15						
6129	$^{16}\text{O}(n,n'\gamma)$ $^{16}\text{O}(n,p\beta)$	22465	0.99	$^{16}\text{O}(n,p\beta)$	4427	1.96	$^{16}\text{O}(n,p\beta)$	3060	2.31

Table 9: Gamma-ray line intensities and uncertainties for the asteroid simulant data, with the HPGe detector wrapped in a boronated-rubber cap, for different timing windows during the PNG pulse period (total acquisition live time = 46.15 hrs) for the asteroid simulant experiment. The “*” symbol means that it is the excited state of the isotope, i.e. $^{25}\text{Mg}^*$ means that it is the excited state of ^{25}Mg through the $^{28}\text{Si}(n,\alpha)^{25}\text{Mg}$ reaction.

E (keV)	Inelastic Scattering Window			Thermal Neutron Capture Window			Delayed Activation & Natural Activity		
	ID	Ig (cts)	σ (%)	ID	ID	Ig (cts)	σ (%)	Ig (cts)	ID
440	$^{23}\text{Na}(n,n'\gamma)$ ^{69m}Zn	9344	5.16	^{69m}Zn	3009	10.5	^{69m}Zn	13073	10.3
585	$^{25}\text{Mg}^*$ $^{69}\text{Ge}+\text{K}$ $^{228}\text{Th}-^{208}\text{Tl}$	33521	0.83	$^{24}\text{Mg}(n,\gamma)$ $^{69}\text{Ge}+\text{K}$ $^{228}\text{Th}-^{208}\text{Tl}$	9323	2.73	$^{69}\text{Ge}+\text{K}$ $^{228}\text{Th}-^{208}\text{Tl}$	6376	2.66
847	$^{27}\text{Al}(n,n'\gamma)$ $^{56}\text{Fe}(n,n'\gamma)$ $^{56}\text{Fe}(n,p\beta)$ $^{26}\text{Mg}(n,\gamma\beta)$ $^{55}\text{Mn}(n,\gamma\beta)$	10899	1.40	$^{56}\text{Fe}(n,p\beta)$ $^{26}\text{Mg}(n,\gamma\beta)$ $^{55}\text{Mn}(n,\gamma\beta)$	47839	0.73	$^{56}\text{Fe}(n,p\beta)$ $^{26}\text{Mg}(n,\gamma\beta)$ $^{55}\text{Mn}(n,\gamma\beta)$	182841	0.43
1014	$^{27}\text{Al}(n,n'\gamma)$ $^{26}\text{Mg}(n,\gamma\beta)$	5096	5.78	$^{26}\text{Mg}(n,\gamma\beta)$	15459	1.27	$^{26}\text{Mg}(n,\gamma\beta)$	86610	0.65
1460	^{40}K	61788	0.77	^{40}K	42430	0.67	^{40}K	29647	0.77
1779	$^{28}\text{Si}(n,n'\gamma)$ $^{28}\text{Si}(n,p\beta\Box)$ $^{27}\text{Al}(n,\gamma\beta)$	81116	0.68	$^{28}\text{Si}(n,p\beta\Box)$ $^{27}\text{Al}(n,\gamma\beta)$	34659	0.75	$^{28}\text{Si}(n,p\beta\Box)$ $^{27}\text{Al}(n,\gamma\beta)$	24152	0.84
1811	$^{56}\text{Fe}(n,n'\gamma)$ $^{56}\text{Fe}(n,p\beta)$ $^{55}\text{Mn}(n,\gamma\beta)$	7947	4.89	$^{56}\text{Fe}(n,p\beta)$ $^{55}\text{Mn}(n,\gamma\beta)$	1562	7.20	$^{56}\text{Fe}(n,p\beta)$ $^{55}\text{Mn}(n,\gamma\beta)$	1018	5.64
1942	$^{40}\text{Ca}(n,n'\gamma)$	492	9.16	$^{40}\text{Ca}(n,\gamma)$	3258	3.80	$^{40}\text{Ca}(n,\gamma)$	7726	4.98
2203		65796	0.86	$^{238}\text{U}-^{214}\text{Bi}$	762	12.6	$^{238}\text{U}-^{214}\text{Bi}$	3987	2.27
2211	$^{27}\text{Al}(n,n'\gamma)$	59979	0.84						
2223	$^1\text{H}(n,\gamma)$	751	33.8	$^1\text{H}(n,\gamma)$	68453	0.50		4957	2.00
2614	$^{228}\text{Th}-^{208}\text{Tl}$	74967	0.93	$^{228}\text{Th}-^{208}\text{Tl}$	5226	2.25	$^{228}\text{Th}-^{208}\text{Tl}$	18979	0.92
4438	$^{12}\text{C}(n,n'\gamma)$ $^{16}\text{O}(n,n'\alpha)$	26327	1.00						
6129	$^{16}\text{O}(n,n'\gamma)$ $^{16}\text{O}(n,p\beta)$	9344	5.16	$^{16}\text{O}(n,p\beta)$	5428	1.97	$^{16}\text{O}(n,p\beta)$	3716	2.16

Once the gamma ray lines have been fit during different time windows during the PNG pulse period, the next step is to subtract out any contributions due to different processes on multiple elements so that one is left with a gamma ray line due to a single process on a single element. Tables 10, 11, and 12 show the results and uncertainties for

the line “cleaning” of the elements listed for the granite monument, the basalt monument, and the asteroid simulant configuration. The elements that were selected were based upon the MCNPX model results for the inelastic window. Each of these tables lists the gamma-ray line energy (E) in units of keV, the gamma-ray line identification (ID), the gamma-ray line intensity (Ig) in units of cts, and the relative uncertainty (σ) in units of % in a time window over the total live time acquisition of 16.21 hrs for the granite monument, 15.23 hrs for the basalt monument, and 46.15 hrs for the asteroid simulant, where the inelastic window for the (n,n' γ) gamma-ray reactions is 10-100 μ s, the capture window for the (n, γ) gamma-ray reactions is 150-650 μ s, and the delayed activation and natural activity window is 650-1000 μ s.

Table 10. Gamma-ray line cleaning results and uncertainties for the granite monument.

E (keV)	ID	Ig (cts)	σ (%)
440	$^{23}\text{Na}(n,n'\gamma)$	17144	19.04
1779	$^{28}\text{Si}(n,n'\gamma)$	73439	0.62
1811	$^{56}\text{Fe}(n,n'\gamma)$	41214	0.97
2211	$^{27}\text{Al}(n,n'\gamma)$	54186	0.96
4438	$^{16}\text{O}(n,\alpha\gamma)^{12}\text{C}$	13265	3.77
6129	$^{16}\text{O}(n,n'\gamma)$	22583	1.02

Table 11. Gamma-ray line cleaning results and uncertainties for the basalt monument.

E (keV)	ID	Ig (cts)	σ (%)
440	$^{23}\text{Na}(n,n'\gamma)$	18086	5.63
1779	$^{28}\text{Si}(n,n'\gamma)$	53124	0.75
1811	$^{56}\text{Fe}(n,n'\gamma)$	484	4.00
2211	$^{27}\text{Al}(n,n'\gamma)$	53265	0.95
4438	$^{16}\text{O}(n,\alpha\gamma)^{12}\text{C}$	11089	4.15
6129	$^{16}\text{O}(n,n'\gamma)$	22465	0.99

Table 12. Gamma-ray line cleaning results and uncertainties for the asteroid simulant.

E (keV)	ID	I_g (cts)	σ (%)
440	²³ Na(n,n'γ)	9792	5.81
1779	²⁸ Si(n,n'γ)	55577	0.86
1811	⁵⁶ Fe(n,n'γ)	80854	0.68
2211	²⁷ Al(n,n'γ)	65796	0.86
4438	¹² C(n,n'γ) ¹⁶ O(n,αγ) ¹² C	74967	0.93
6129	¹⁶ O(n,n'γ)	25371	1.04

Next, determining elemental ratios is an interim step to calculating elemental weight percent values from the data. This is done by normalizing all elements to Si so that one can compare them to the MCNPX inelastic window ratios. Tables 13, 14, and 15 list the gamma-ray experimental and MCNPX ratios for the granite, basalt and asteroid simulant. Each table consists of 5 columns showing the isotopic ratio identifications (Ratio), the experimental ratio (Exp. Ratio) between each gamma-ray line/Si gamma-ray line for all gamma rays listed in Tables 10-12, the uncertainty of the experimental ratio with relative uncertainty (σ) in units of %, the MCNPX gamma-ray line ratios (MCNPX Ratio) corresponding to the same gamma-ray lines in Tables 10-12, and the relative uncertainty of the MCNPX ratio (σ) in units of %.

As seen in Table 13 for the PING granite experiment, the Na/Si experimental isotopic ratio and uncertainty is $0.233 \pm 5.67\%$ as compared to the MCNPX ratio and uncertainty that is $0.026 \pm 37.79\%$. Even with the large uncertainty associated with the MCNPX ratio, the two ratios differ approximately by a factor of 10. The Al/Si experimental ratio as compared to the MCNPX ratio is $0.738 \pm 1.14\%$ and $0.119 \pm 4.69\%$ differing by approximately a factor of 6. The Fe/Si experimental and MCNPX ratios and

uncertainties are $0.561 \pm 1.15\%$ and $0.043 \pm 7.88\%$ differing approximately by a factor of 10. The C/Si experimental and MCNPX ratios and uncertainties are $0.181 \pm 3.82\%$ and $0.100 \pm 3.12\%$ differing approximately by a factor of 1.8. The O/Si experimental and MCNPX ratios and uncertainties are $0.548 \pm 0.70\%$ and $0.473 \pm 1.38\%$ differing approximately by a factor of 1.2.

Table 13. Gamma-ray element/Si experimental and MCNPX ratios for the granite.

Ratio	Exp. Ratio	σ (%)	MCNPX Ratio	σ (%)
Na/Si	0.233	5.67	0.026	37.79
Al/Si	0.738	1.14	0.119	4.69
Fe/Si	0.561	1.15	0.043	7.88
O/Si	0.181	3.82	0.100	3.12
O/Si	0.548	0.70	0.473	1.38

In general, all of MCNPX ratios are less than their corresponding experimental ratios by an average factor of 8.7, with the exception of the O/Si ratios that differ by an average factor of 1.5, which puts the O/Si experimental and MCNPX ratios in fairly good agreement with one another. However, the Na/Si, Al/Si, and Fe/Si experimental and MCNPX ratios are in poor agreement. This poor agreement can be due to the fact that the experimental ratios take into account everything in the experiment, while the MCNPX model was constructed using only a point neutron source for the PNG and an isolated HPGe crystal for the HPGe detector located at approximately the correct distance and location from the PNG. The model did not include the HPGe detector housing and dewar, the PNG housing or either of the neutron detectors. The locations of the detectors and PNG were at the same approximate locations as on the granite monument. The absence of these pieces of equipment could explain the low value of the Al/Si and Fe/Si ratios since the PNG housing and the HPGe housing and dewar contain a great deal of Al

and some steel (which contains Fe). The low value of the MCNPX Na/Si ratio as compared to the experimental ratio could be explained by the contribution of another element present in addition to Na that produces a gamma-ray line that overlaps in energy with the 440 keV gamma-ray line.

As seen in Table 14 for the PING basalt monument experiment, the Na/Si experimental isotopic ratio and uncertainty is $0.340 \pm 19.05\%$ as compared to the MCNPX ratio and uncertainty that is $0.050 \pm 13.97\%$. Even with the large uncertainty associated with the each ratio, the two ratios differ approximately by a factor of 6.8. The Al/Si experimental ratio as compared to the MCNPX ratio is $0.171 \pm 14.82\%$ and $0.068 \pm 3.84\%$ and they differ approximately by a factor of 2.5. The Fe/Si experimental and MCNPX ratios and uncertainties are $0.820 \pm 1.17\%$ and $0.010 \pm 40.29\%$, even with the large uncertainty on the MCNPX ratio, both ratios differ approximately by a factor of 82. The first O/Si experimental and MCNPX ratios and uncertainties are $0.209 \pm 4.22\%$ and $0.113 \pm 3.28\%$ and they differ approximately by a factor of 1.8. The second O/Si experimental and MCNPX ratios and uncertainties are $0.408 \pm 1.27\%$ and $0.536 \pm 1.51\%$ and differ approximately by a factor of 0.8.

Table 14. Gamma-ray Element/Si experimental and MCNPX ratios for the basalt.

Ratio	Exp. Ratio	σ (%)	MCNPX Ratio	σ (%)
Na/Si	0.340	19.05	0.050	13.97
Al/Si	0.171	14.82	0.068	3.84
Fe/Si	0.820	1.17	0.010	40.29
O/Si	0.209	4.22	0.113	3.28
O/Si	0.408	1.27	0.536	1.51

In general, all of MCNPX ratios are less than their corresponding experimental ratios, with the exception of the second O/Si ratio that is in more agreement with the

experimental ratio. The Al/Si experimental ratio as compared to the MCNPX ratio differs by an approximate average factor of 2.5 and this difference is most likely due to the lack of Al in the model as mentioned in the discussion about Table 13. The lower value of the MCNPX Na/Si ratio could be explained by the distance and location of the PNG and HPGe detector on the basalt monument as mentioned in the Table 13. Both O/Si experimental and MCNPX ratios are in fairly good agreement with one another and differ on average by a factor approximately 0.9. However, Fe/Si experimental and MCNPX ratios are in very poor agreement with each other and differ by a factor of 82. The poor agreement can be due to the fact that the experimental ratios take into account everything in the experiment, while the MCNPX model was constructed with only a point source for the PNG and a HPGe crystal for the HPGe detector at approximately the correct distance and location from the PNG. As previously discussed, the model didn't include the HPGe detector housing and dewar, the PNG housing or either of the neutron detectors and the locations of the detectors and PNG were at the same approximate locations as on the granite monument. The absence of these pieces of equipment could explain the low value of the Fe/Si ratios, since the PNG and HPGe housing and dewar contained a great deal of Al and some steel (which contains Fe).

As seen in Table 15 for the PING asteroid simulant experiment, the Na/Si experimental isotopic ratio and uncertainty is $0.176 \pm 5.97\%$ as compared to the MCNPX ratio and uncertainty that is $0.087 \pm 17.35\%$. Even with the large uncertainty associated with the MCNPX ratio, the two ratios differ approximately by a factor of 2. The Al/Si experimental ratio as compared to the MCNPX ratio is $1.184 \pm 1.27\%$ and $0.134 \pm 5.43\%$ and they differ approximately by a factor of 8.8. The Fe/Si experimental and MCNPX

ratios and uncertainties are $1.455 \pm 0.86\%$ and $0.019 \pm 19.27\%$, even with the large uncertainty on the MCNPX ratio, both ratios differ approximately by a factor of 76.6. The C/Si experimental and MCNPX ratios and uncertainties are $1.349 \pm 1.27\%$ and $2.208 \pm 1.55\%$ and they differ approximately by a factor of 0.6. The O/Si experimental and MCNPX ratios and uncertainties are $0.457 \pm 1.35\%$ and $0.675 \pm 1.95\%$ and differ approximately by a factor of 0.7.

Table 15. Gamma-ray Element/Si experimental and MCNPX ratios for the asteroid simulant.

Ratio	Exp. Ratio	σ (%)	MCNPX Ratio	σ (%)
Na/Si	0.176	5.87	0.087	17.35
Al/Si	1.184	1.27	0.134	5.43
Fe/Si	1.455	0.86	0.019	19.27
C/Si	1.349	1.27	2.208	1.55
O/Si	0.457	1.35	0.675	1.95

In general, all of MCNPX ratios are less than their corresponding experimental ratios, with the exception of the C/Si and the O/Si ratios that are larger than its corresponding experimental ratios and are in fairly good agreement. The Al/Si experimental ratio as compared to the MCNPX ratio differs by an approximate average factor of 8.8 and this difference could be due to the lack of Al in the model as mentioned in the discussion about Table 13. The Na/Si ratios differ by a factor of 2. The lower value of the MCNPX Na/Si ratio could be explained by the distance from the PNG to the HPGe detector as mentioned in the Table 13 discussion. The C/Si and O/Si experimental and MCNPX ratios are in fairly good agreement with one another and differ on average by a factor approximately 0.6. However, Fe/Si experimental and MCNPX ratios are in very poor agreement with each other and differ by a factor of 76.6. The poor agreement

can be due to the fact that the experimental ratios take into account everything in the experiment, while the MCNPX model was constructed with only a point source for the PNG and a HPGe crystal for the HPGe detector at approximately the correct distance and location from the PNG. The model did not include the HPGe detector housing and dewar, the PNG housing or either of the neutron detectors and the locations of the detectors and PNG where at the approximate locations on the granite monument. The absence of these pieces of equipment could explain the low value of the Fe/Si ratios, since the PNG housing and HPGe housing and dewar contained a great deal of Al and some steel (contains Fe).

It is important to note overall that there is essentially no C present in the pure granite and basalt monuments, therefore the experimental and MCNPX ratios are really due to the $^{16}\text{O}(n,n'\alpha)$ reaction. Since the same amount, or somewhat less (because of no O in the high-density polyethylene) amount of oxygen should come from the asteroid simulant, the significant increase in the experimental value is due to the real presence of carbon and not the carbon counts coming from the element O. Further work on refining the Monte Carlo model, to account for the counts due to the equipment especially in the Al and Fe peaks, will be pursued in the near future.

Neutron

The thermal neutron dieaway data was analyzed for the granite, basalt and asteroid layering configurations and compared to their elemental assays to determine the thermal macroscopic neutron absorption cross-sections of each configuration. The dieaway curves were each fit with a double exponential due to the fact that there are

competing neutron processes shown during different time intervals as indicated by fast neutron, epithermal and thermal neutron, thermal neutron and neutron diffusion. The 14 MeV fast neutrons slow down through the process of elastic scattering, off of elements in the regolith, producing epithermal neutrons that are further slowed down through inelastic scattering that then results in thermal neutrons that can be captured by other elements and final neutron diffusion occurs since not all neutrons that interact in the regolith are absorbed. Figures 44, 45, and 46 show the fitted thermal neutron dieaway for the granite monument, the basalt monument and the asteroid simulant displayed as a function of time during the PNG pulse period (x-axis) and number of neutrons detector in counts (y-axis). The thermal neutron region of the exponential fit is different for Figures 44, 45 and 46, due to the difference in the way each material moderates neutrons. Tables 16, 17, and 18 show the calculated macroscopic thermal neutron absorption cross-section calculation spreadsheet for the granite monument, the basalt monument, and the asteroid simulant based upon an independent elemental assay.

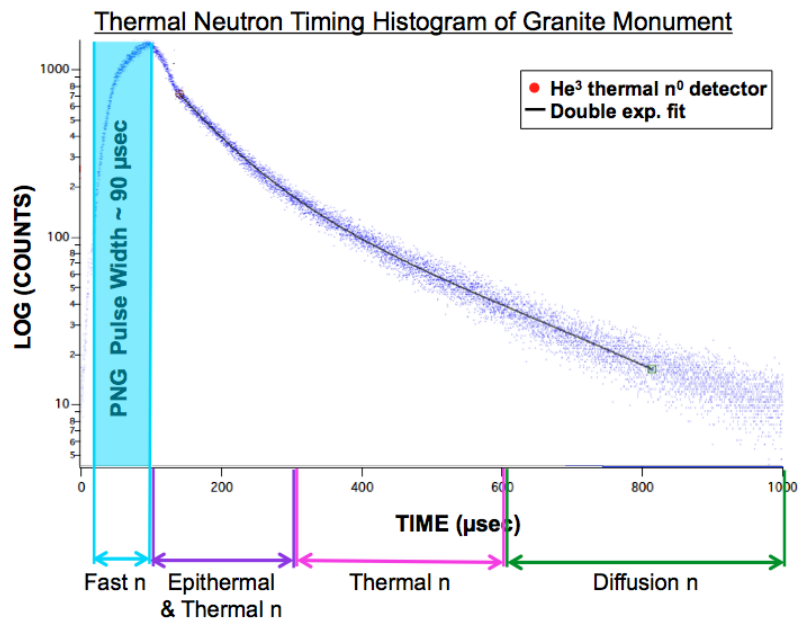


Figure 44. Experimental thermal neutron dieaway results and fit for the granite.

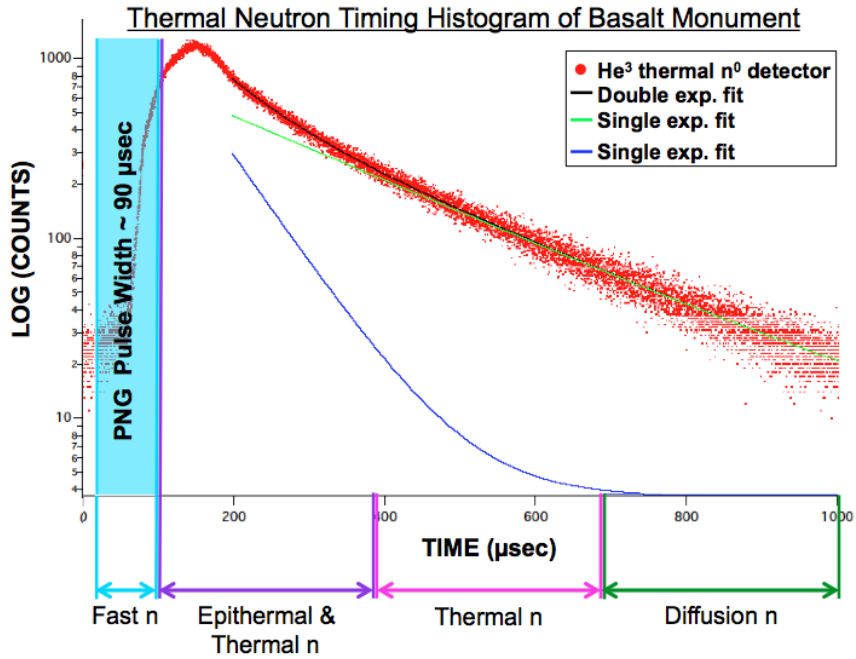


Figure 45. Experimental thermal neutron dieaway results and fit for the basalt.

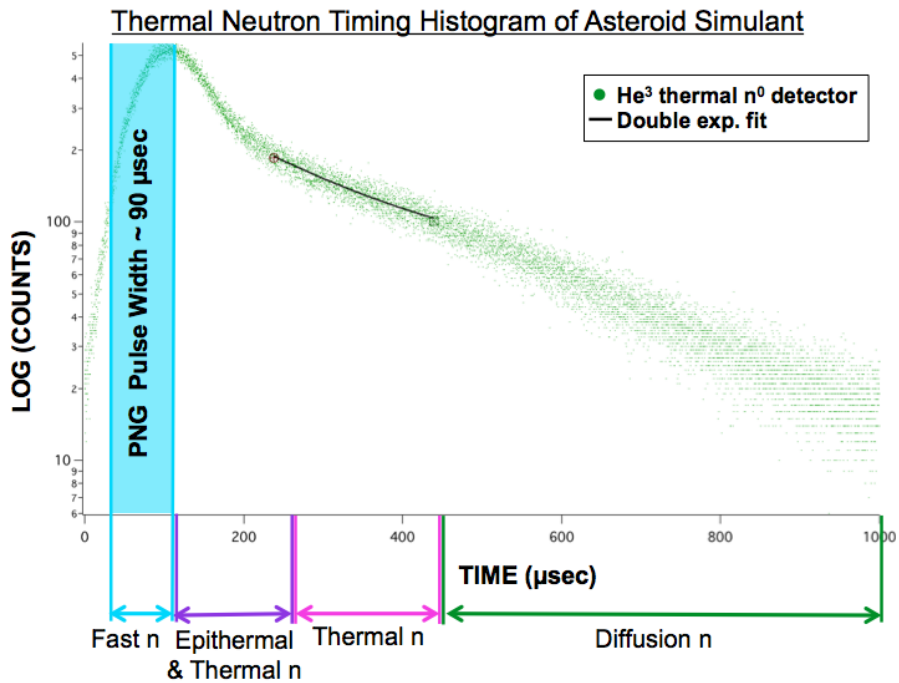


Figure 46. Experimental thermal neutron dieaway results and fit for the asteroid simulant.

Table 19 lists the comparison of the thermal neutron absorption cross-section obtained from the fitted experimental thermal neutron dieaway data and the calculated macroscopic thermal neutron absorption cross-section, calculation spreadsheets shown in Tables 16-18, for all three configurations. It is important to note that the calculated macroscopic thermal neutron absorption cross-section for the layered asteroid simulant is based on CII carbonaceous chondrite calculations and the macroscopic thermal neutron absorption cross-section (Σ_a) was obtained from the layered asteroid fitted experimental thermal neutron dieaway data. There is good agreement between the calculated and experimental Σ_a values.

Table 19. Granite, basalt and asteroid simulant calculated and experimental macroscopic thermal neutron absorption comparison. Note: the asteroid simulant calculated value is based upon CII carbonaceous chondrite calculations.

Σ_a (cm)	Homogeneous Granite Monument	Homogeneous Basalt Monument	Layered Asteroid Simulant
Calc.	0.0114	0.0179	0.0264
Exp.	$0.0119 \pm 2.13\%$	$0.0189 \pm 2.43\%$	$0.0246 \pm 8.09\%$

CHAPTER V

CONCLUSIONS

Asteroids are the remains of the formation of the Solar System. They provide us with a glimpse into the past and insight into how our solar system formed, evolved and how life may have begun. Unfortunately there is still a lot we do not understand about asteroids including which meteorites belong to which asteroid classes and types and what asteroid bulk geochemistry traits differentiate one type from another. In order to find the answers to what we don't know about asteroids, we must collect information on a wide variety of wavelengths and spatial resolutions. One way to determine the bulk elemental composition of asteroids is through the development and testing of the Probing *In situ* with Neutrons and Gamma rays (PING) instrument on well-characterized granite, basalt, and asteroid simulant monuments.

The asteroid simulant monument was designed, with the help of a Monte Carlo model, to have the same bulk elemental concentration as a typical CI1 asteroid and to have the same neutron response as a homogeneous asteroid. The latter criterion ensures that experimental measurements on the asteroid simulant monument will have the same relationship between gamma-ray peak count rates and elemental concentrations as would occur for measurements on the surface of a homogeneous asteroid.

The monuments are located at a unique facility implemented at Goddard Space Flight Center. PING utilizes fast neutrons, generated by a 14 MeV pulsed neutron generator, to probe a meter radius area and down up to a meter into the subsurface

regolith. PING's neutron and gamma-ray spectrometers detect the resultant moderated neutrons and gamma rays that reach the surface. The data collected are then analyzed and used to determine the bulk properties and composition of the regolith material probed.

A Monte Carlo model has also been established and benchmarked to be able to calculate the detector responses under a wide range of conditions. Comparisons of PING experimental results to the Monte Carlo computer simulations and independently verified monument element assays show that more comprehensive MCNPX models are needed to properly model PING experiments in detail. However, we have shown that PING is capable of quantitatively determining the bulk properties of asteroids, aiding in differentiating between different types of asteroids and strengthening their connection to meteorites. The current MCNPX model is in excellent agreement with the experimental neutron responses, but the detailed gamma-ray count rates for a number of elements need more accurate modeling of the experimental instrumentation. In one or two cases, further investigation of possible sources of the production of specific gamma rays from competing elements and reactions will be necessary to get agreement between measured concentrations from specific gamma rays and the concentrations obtained from the laboratory determined assays of the rocks. Once this is achieved, we have already demonstrated that a landed PING will provide very good precision in a reasonable time frame for typical mission parameters. Of particular interest is the clarity with which elemental concentrations of carbon, that are typical of carbonaceous asteroids, can be readily obtained.

The work reported here has firmly established that important geochemical information on asteroids, based on elemental analysis and neutron transport, can be obtained with instrumentation such as PING. Thus a future mission to one or more asteroids can have substantially increased science return providing a direct description of the asteroid subsurface, without drilling or otherwise disrupting the surface. This will help provide information that can improve our understanding of the relation between meteorites and specific asteroid types. Furthermore, we have shown that asteroid composition can be fabricated in large volume structures on Earth, which can also be modeled with MCNPX, to allow direct experimental tests of specific asteroid types. These asteroid simulant structures can be used, together with a benchmarked Monte Carlo program, to predict mission responses to optimize the science return before launch.

REFERENCES

- [1] Jenniskens, P., *et al.*, (2009), “The impact and recovery of asteroid 2008 TC3”, *Nature*, 458: 485-488.
- [2] Nesvorny, D., *et al.*, (2009), “Asteroidal source of Lchondrite meteorites”, *Icarus*, 200:698-701.
- [3] From "An Introduction to Asteroids" a Fact Sheet accompanying "Asteroid Sample Return – A Many Layered, High-Payoff, Multiple Choice Problem" by Dante Lauretta, Joe Nuth, Carl Hergenrother, Bashar Rizk, John Oberright, John Galloway, John Marshall, Jason Dworkin, Dave Folta, Frank Vaughn, Vladimir Lumelsky, Bob Jenkens, Bill Cutlip, and Laura Via presented to NASA Headquarters Science Mission Directorate October 7, 2008.
- [4] Illustration created by Sarah Noble at NASA/GSFC:
<http://www.interplanetsarah.com/SpaceWeathering.html>
- [5] Nuth, J. A. (2008), *Earth Moon Planet*, 102, 435-445.
- [6] Morbidelli, A., Chambers, J., Lunine, J. I., Petit, J. M., Robert, F., Valsecchi, G. B., and Cry, K. E., (2000), “Source regions and time scales for the delivery of water to Earth”, *Meteoritics & Planetary Science*, 35, 1309-1320.
- [7] Burbine, T. H., McCoy, T. J., Meibom, A., Gladman, B., and Keil, K., (2002), “Meteoritic parent bodies: Their number and identification.” *Asteroids III*, 653-667.
- [8] Clark, B. E., Ziffer, J., Nesvorny, D., Campins, H., Rivikin, A. S., Hiroi, T., Barucci, M. A., Fulchignoni, M., Binzel, R. P., Fornasier, S., DeMeo F., Ockert-Bell, M. E., Licandro, J., and Mothé-Diniz, T., (2010), “Spectroscopy of B-type asteroids: Subgroups and meteorite analogs”, *Journal of Geophysical Research (Planets)*, 115(E14).
- [9] Bus, S. J. and Binzel, R. P., (2002), “Phase II of the small main-belt asteroid spectroscopic survey: A feature-based taxonomy”, *Icarus*, 158:146-177.
- [10] DeMeo, F. E., Binzel, R. P., Slivan, S. M. and Bus, S. J., (2009), “An extension of the Bus asteroid taxonomy in the near-infrared”, *Icarus*, 202:160-180.
- [11] Jones, T. D., Lebofsky, L. A., Lewis, J. S., and Marley, M. S., (1990), “The composition and origin of the C, P, and D asteroids – Water is a tracer of thermal evolution in the outer belt”, *Icarus*, 88, 172-192.
- [12] Hiroi, T., Zolensky, M. E., Pieters, C. M., and Lipshutz, M. E., (1996), “Thermal metamorphism of the C, G, B, and F asteroids seen from the 0.7 micron, 3 micron and

- UV absorption strengths in comparison with carbonaceous chondrites”, *Meteoritics and Planetary Science*, 31, 321-327.
- [13] Rivkin, A. S., Davies, J. K., Johnson, J. R., Ellison, S. L., Trilling, D. E., Brown, R. H., and Lebofsky, L. A., (2003), “Hydrogen concentrations on C-class asteroids derived from remote sensing”, *Meteoritics and Planetary Science*, 38, 1383-1398.
- [14] Campins, H., *et al.*, (2010), *Nature*, 464, 1320-1321.
- [15] Rivkin, A. S. and Emery, J. P., (2010), *Nature*, 464, 1322-1323.
- [16] Schörghofer, N., (2008), *Ap. J.*, 682, 697-705.
- [17] Prialnik, D. and Rosenberg, E. D., (2009), *Mon. Not. R. Astron. Soc.*, 399, L79-L-83.
- [18] Gaffey M. J., Cloutis E. A., Kelley M. S., and Reed K. L., (2002), “Mineralogy of asteroids.” *Asteroids III*, 183–204.
- [19] McCoy, T. J., *et al.*, (2001), “The composition of 433 Eros: A mineralogical-chemical synthesis”, *Meteoritics and Planetary Science*, 36, 1661-1672.
- [20] Feldman, W. C., *et al.*, (2004), *J. Geophys. Res.*, 109, E07S06.
- [21] Boynton, W. V., *et al.*, (2004), *Space Sci. Rev.*, 110, 37.
- [22] Boynton, W. V., *et al.*, (2002), *Science*, 297, 81.
- [23] Prettyman, T. H., *et al.*, (2003), *IEEE Trans. Nucl. Sci.*, N50, 1190.
- [24] Goldsten, J. O., *et al.*, (2007), *Space Sci. Rev.*, 131, 339.
- [25] Evans, L. G., *et al.*, (2001), *MAPS*, 36, 1639.
- [26] Mitrofanov, I. G., *et al.*, (2010), *Space Sci. Rev.*, 150, 183.
- [27] Mitrofanov, I. G., *et al.*, (2008), *Astrobiology*, 8, 793.
- [28] Akkurat, *et al.*, (2005), *Nucl. Inst. Meth. B*, 241, 232.
- [29] Schweitzer, J. S., (1993), “Subsurface Nuclear Measurements for Geochemical Analysis”, 1993, Chap. 23 in *Remote Geochemical Analysis: Elemental and Mineralogical Composition, Topics in Remote Sensing 4*, Carle M. Pieters and Peter A. J. Englert Eds., Cambridge University Press.
- [30] McCoy, T J, T H Burbine, L A McFadden, R D Starr, M J Gaffey, L R Nittler, and others, (2001), ‘The Composition of 433 Eros: a Mineralogical-Chemical Synthesis’, *Meteoritics and Planetary Science*, 36:1661.

- [31] Grau, J. A., *et al.*, IRRMA '92, Raleigh, NC, 8-11 Sept., 1992; (1993), *Int. J. Rad. Appl. Instr. Part E*, 7, 173.
- [32] Parsons, A., *et al.*, (2011), *Nucl. Instr. and Meth. A*, 652, 674.
- [33] Schweitzer, J. S., (1993), "Subsurface Nuclear Measurements for Geochemical Analysis", 1993, Chap. 23 in *Remote Geochemical Analysis: Elemental and Mineralogical Composition, Topics in Remote Sensing 4*, Carle M. Pieters and Peter A. J. Englert Eds., Cambridge University Press.
- [34] Herron, S.L. *et al.* (1993) *Remote Geochemical Analysis: Elemental and Mineralogical Composition*, eds. C.M. Pieters and P.A.J. Englert, pp.507-537, Cambridge University press, New York.
- [35] Ellis, D. V., Schweitzer, J. S., Ullo, J. J., (1987), "Nuclear Techniques for Subsurface Geology", *Ann. Rev. Nucl. Part. Sci.*, 37, 213.
- [36] Grau, J. A., Schweitzer, J. S., Ellis, D. V., Hertzog, R. C., (1989), "A Geological Model for Gamma-Ray Spectroscopy Logging Measurements", *Nucl. Geophys.*, 3, 351.
- [37] Grau, J. A., Schweitzer, J. S., Hertzog, R. C., (1990), "Statistical Uncertainties of Elemental Concentrations Extracted from Neutron-Induced Gamma-Ray Measurements", *IEEE Trans. Nucl. Sci.*, 37, 2175.
- [38] Hertzog, R., Colson, L., Seeman, B., O'Brien, M., Scott, H., McKeon, D., Wright, P., Grau, J., Ellis, D., Schweitzer, J., Herron, M., (1989), "Geochemical Logging with Spectrometry Tools", *SPE Formation Evaluation*, 4, 153.
- [39] Schweitzer, J. S., Ellis, D. V., Grau, J. A., Hertzog, R. C., (1988), "Elemental Concentrations from Gamma-Ray Spectroscopy Logs", *Nucl. Geophys.*, 2, 175.
- [40] Schweitzer, J. S., (1991), "Nuclear Techniques in the Oil Industry", *Nucl. Geophys.*, 5, 1/2, 65.
- [41] Mills, Jr., W. R., Givens, W. W., "Neutron Die-Away Experiment for Lunar and Planetary Surface Analysis, Final Report", 26 Jul 1966 – 26 Mar 1967 (Mobile Oil Corp. Field Research Laboratory) 120 p.
- [42] Mills, Jr., W. R., Givens, W. W., "Neutron Die-Away Experiment for Lunar and Planetary Surface Analysis, Progress Report", 3 Jul 1967 – 28 Jun 1969 (Mobile Research and Development Corporation, Field Research Laboratory) 124 p.
- [43] Mills, Jr., W. R., Allen, L. S., "Neutron Die-Away Experiment for Lunar and Planetary Surface Analysis, Final Report", 1 Jun 1970 – 30 Nov 1971 (Mobile Research and Development Corporation, Field Research Laboratory) 110 p.

- [44] Hearst, J. R., "Neutron Logging in Partially Saturated Media," 22 Apr 1974, Preprint for the International Seminar on Instruments and Systems for Measuring and Monitoring Water Quality and Quantity, Chicago, June 4, 1974, 24 p.
- [45] Mandler, J. W., "Continued Development of the Combined pulsed neutron experiment (CPNE) for Lunar and Planetary Surfaces, Final Report," 15 Jun 1971 – 23 Sep 1972 (IIT Research Institute) 65 p.
- [46] Givens, W. W., Mills, W. R., Caldwell, R. L., (1970) "Cyclic Activation Analysis," *Nucl. Inst. and Methods*, v. 80, p. 95-103.
- [47] Caldwell, R. L., Mills, Jr., W. R., Allen, L. S., Bell, P. R., Heath, R. L., (1966) "Combination Neutron Experiment for Remote Analysis," *Science*, vol. 152, no. 3721, p. 457-465.
- [48] Boynton, W. V., Evans, L. G., Reedy, R. C., and Trombka, J. I., (1993), "Determination of Planetary Composition by In-situ and Remote Gamma-Ray Spectrometry", in *Remote Geochemical Analysis: Elemental and Mineralogical Composition*, ed. C. Pieters and P. Englert, Cambridge University Press, pp. 395-411.
- [49] Evans, L. G., Reedy, R. C., and Trombka, J. I., 1993, "Introduction to Planetary Remote Sensing," in *Remote Geochemical Analysis: Elemental and Mineralogical Composition*, ed. C. Pieters and P. Englert, Cambridge University Press, pp. 167-198.
- [50] Feldman, W. C., *et al.*, (2000), "Chemical Information Content of Lunar Thermal and Epithermal Neutrons", *J. Geophys. Res.*, 105(E8), 20347-20363.
- [51] Grau, J. A., Schweitzer, J. S., and Hertzog, R. C., (1990), "Statistical Uncertainties of Elemental Concentrations Extracted from Neutron-Induced Gamma-Ray Measurements", *IEEE Trans. Nucl. Sci.*, 37, 2175.
- [52] Evans, *et al.*, (2006), *J. Geophys. Res.* 111 No. E3.
- [53] Evans, *et al.*, (2001), *Meteoritics and Planetary Science*, 36,1639-1660.
- [54] Prettyman, *et al.*, (2006), *J. Geophys. Res.*, 111, E12007.
- [55] D.B. Pelowitz, *et al.*, (2005) MNCPIX User's Manual, Version 2.5.0, LANL, Los Alamos, LA- UR-05-0369.
- [56] Boynton, W. V., *et al.*, (2004), *Space Sci. Rev.*, 110, 37.
- [57] Knoll, G.F. (1989) *Radiation Detection and Measurement*, John Wiley and Sons, New York, Chapter 14.

- [58] Schweitzer, J. S., (1993), "Subsurface Nuclear Measurements for Geochemical Analysis", 1993, Chap. 23 in *Remote Geochemical Analysis: Elemental and Mineralogical Composition, Topics in Remote Sensing 4*, Carle M. Pieters and Peter A. J. Englert Eds., Cambridge University Press.
- [59] Bodnarik, J. G., *et al.*, "PING Gamma Ray and Neutron Measurements of a Meter-Scale Carbonaceous Asteroid Analog Material," 43rd Lunar and Planetary Science Conference, **No. 1544** (2012).
- [60] D.B. Pelowitz, *et al.*, (2005) MNCPIX User's Manual, Version 2.5.0, LANL, Los Alamos, LA- UR-05-0369.
- [61] A. M. Parsons, personal communication, 2009.
- [62] Knoll, G.G. (1999). *Radiation Detection and Measurement, 3rd edition*. Wiley. p 365.
- [63] Knoll, G.G. (1999). *Radiation Detection and Measurement, 3rd edition*. Wiley. p 508.
- [64] CANBERRA Lynx Digital Signal Analyzer application note (2012)
<http://www.canberra.com/literature/438222.asp>.
- [65] D. Burger, personal communication, 2011.
- [66] J. Bodnarik *et al.*, (2013), "Time-Resolved Neutron/Gamma-Ray Data Acquisition for In Situ Subsurface Geochemistry," *Nucl. Inst. and Methods in Phys. Research A*, v. 707, p. 135-142.
- [67] R. J. Radtke, *et al.*, SPWLA 53rd Annual Logging Symposium, Cartagena, Columbia, June 16-20, 2012.
- [68] Thermo Scientific MP320 Neutron Generator Operation Manual.
- [69] Knoll, G.G. (1999). *Radiation Detection and Measurement, 3rd edition*. Wiley. p 56.
- [70] Randy A. Schwarz, Visual Editor Consultants, www.mcnpvised.com

APPENDIX I

ACTIVATION LABORATORIES LTD. ELEMENTAL ASSAYS

Concord Grey Granite Assay

Activation Laboratories Granite Assay Report

Tables 20 and 21 are the results of the independent elemental assay of the Columbia River Basalt and Concord Grey Granite performed by Activation Laboratories Ltd. (ActLabs) in Ancaster, Ontario, Canada.

Table 20. ActLabs Columbia River Basalt Elemental Assay.

Report: A09-1100 Report Date: 7/20/2010 Columbia River Basalt Elemental Assay Activation Laboratories Ltd., Ancaster, Ontario, Canada													
Final Report Activation Laboratories													
Analyte Symbol	B	Mass	Cl	Mass	H-Total	Total N	SiO2	Al2O3	Fe2O3(T)	MnO	MgO	CaO	Na2O
Unit Symbol	ppm	g	%	g	%	%	%	%	%	%	%	%	%
Detection Limit	0.5		0.01		0.01	0.01	0.01	0.01	0.01	0.001	0.01	0.01	0.01
Analysis Method	PGNAA	PGNAA	INAA	INAA	IR	Analyzer	FUS-ICP	FUS-ICP	FUS-ICP	FUS-ICP	FUS-ICP	FUS-ICP	FUS-ICP
COLUMBIA RIVER BASALT	4.4	1.04	0.04	1.07	0.03	< 0.01	49.59	16.32	10.5	0.161	7.95	9.26	3.3
Analyte Symbol	K2O	TiO2	P2O5	LOI	Total	Sc	Be	V	Cr	Co	Ni	Cu	Zn
Unit Symbol	%	%	%	%	%	ppm	ppm	ppm	ppm	ppm	ppm	ppm	ppm
Detection Limit	0.01	0.001	0.01		0.01	1	1	5	20	1	20	10	30
Analysis Method	FUS-ICP	FUS-ICP	FUS-ICP	FUS-ICP	FUS-ICP	FUS-ICP	FUS-ICP	FUS-ICP	FUS-MS	FUS-MS	FUS-MS	FUS-MS	FUS-MS
COLUMBIA RIVER BASALT	1.15	1.499	0.42	-0.08	100.1	26	1	215	350	41	150	70	100
Analyte Symbol	Ga	Ge	As	Rb	Sr	Y	Zr	Nb	Mo	Ag	In	Sn	Sb
Unit Symbol	ppm	ppm	ppm	ppm	ppm	ppm	ppm	ppm	ppm	ppm	ppm	ppm	ppm
Detection Limit	1	0.5	5	1	2	0.5	1	0.2	2	0.5	0.1	1	0.2
Analysis Method	FUS-MS	FUS-MS	FUS-MS	FUS-MS	FUS-ICP	FUS-MS	FUS-MS	FUS-MS	FUS-MS	FUS-MS	FUS-MS	FUS-MS	FUS-MS
COLUMBIA RIVER BASALT	18	1.3	< 5	10	861	21.1	162	17.4	< 2	0.7	< 0.1	1	< 0.2
Analyte Symbol	Cs	Ba	La	Ce	Pr	Nd	Sm	Eu	Gd	Tb	Dy	Ho	Er
Unit Symbol	ppm	ppm	ppm	ppm	ppm	ppm	ppm	ppm	ppm	ppm	ppm	ppm	ppm
Detection Limit	0.1	3	0.05	0.05	0.01	0.05	0.01	0.005	0.01	0.01	0.01	0.01	0.01
Analysis Method	FUS-MS	FUS-ICP	FUS-MS	FUS-MS	FUS-MS	FUS-MS	FUS-MS	FUS-MS	FUS-MS	FUS-MS	FUS-MS	FUS-MS	FUS-MS
COLUMBIA RIVER BASALT	< 0.1	358	25.5	56.1	7.04	28.8	5.65	1.68	4.7	0.72	4.14	0.76	2.13
Analyte Symbol	Tm	Yb	Lu	Hf	Ta	W	Tl	Pb	Bi	Th	U	C-Total	Total S
Unit Symbol	ppm	ppm	ppm	ppm	ppm	ppm	ppm	ppm	ppm	ppm	ppm	%	%
Detection Limit	0.005	0.01	0.002	0.1	0.01	0.5	0.05	5	0.1	0.05	0.01	0.01	0.01
Analysis Method	FUS-MS	FUS-MS	FUS-MS	FUS-MS	FUS-MS	FUS-MS	FUS-MS	FUS-MS	FUS-MS	FUS-MS	FUS-MS	IR	IR
COLUMBIA RIVER BASALT	0.31	1.99	0.312	3.2	0.87	< 0.5	< 0.05	< 5	< 0.1	2.83	0.72	0.03	< 0.01

Table 21. ActLabs Concord Grey Granite Elemental Assay.

Report: A09-1100														Final Report	
Activation Laboratories															
Report Date: 14/04/2009															
Concord Grey Granite Elemental Assay															
Activation Laboratories Ltd., Ancaster, Ontario, Canada															
Analyte Symbol	B	Mass	C-Total	Total S	Cl	Mass	H-Total	Total N	SiO ₂	Al ₂ O ₃	Fe ₂ O ₃ (T)	MnO	MgO		
Unit Symbol	ppm	g	%	%	%	g	%	%	%	%	%	%	%	%	%
Detection Limit	0.5		0.01	0.01	0.01		0.01	0.01	0.01	0.01	0.01	0.001	0.01		
Analysis Method	PGNAA	PGNAA	IR	IR	INAA	INAA	IR	Analyzer	FUS-ICP	FUS-ICP	FUS-ICP	FUS-ICP	FUS-ICP		
EAST SIDE	4	1.04	0.03	< 0.01	0.02	1.07	0.09	0.01	71.63	14.06	2.1	0.056	0.3		
WEST SIDE	10.9	1.02	0.03	< 0.01	0.02	1.05	0.09	< 0.01	72.06	14.31	1.73	0.052	0.3		
PAVER	4.3	1.08	0.03	< 0.01	0.02	1.06	0.08	< 0.01	73.62	13.99	1.7	0.049	0.28		
EAST SIDE (CERAMIC)									74.36	14.2	1.55	0.052	0.3		
WEST SIDE (CERAMIC)									73.45	14.15	1.46	0.05	0.29		
PAVER (CERAMIC)									74.22	13.16	1.26	0.045	0.26		
Analyte Symbol	CaO	Na ₂ O	K ₂ O	TiO ₂	P ₂ O ₅	LOI	Total	Sc	Be	V	Cr	Co	Ni		
Unit Symbol	%	%	%	%	%	%	%	ppm	ppm	ppm	ppm	ppm	ppm	ppm	ppm
Detection Limit	0.01	0.01	0.01	0.001	0.01		0.01	1	1	5	20	1	20		
Analysis Method	FUS-ICP	FUS-ICP	FUS-ICP	FUS-ICP	FUS-ICP	FUS-ICP	FUS-ICP	FUS-ICP	FUS-ICP	FUS-ICP	FUS-MS	FUS-MS	FUS-MS		
EAST SIDE	0.9	3.08	5.22	0.247	0.22	0.6	98.42	3	12	11	50	2	< 20		
WEST SIDE	0.89	3.13	5.38	0.231	0.22	0.74	99.04	3	9	9	30	4	< 20		
PAVER	0.87	3.08	5.19	0.236	0.2	0.76	99.99	3	9	10	< 20	2	< 20		
EAST SIDE (CERAMIC)	0.9	3.06	5.3	0.244	0.22	0.74	100.9	3	16	10	< 20	1	< 20		
WEST SIDE (CERAMIC)	0.88	3.03	5.27	0.239	0.2	0.86	99.89	3	11	10	< 20	1	< 20		
PAVER (CERAMIC)	0.82	2.94	4.89	0.226	0.18	0.79	98.78	2	8	9	< 20	1	< 20		
Analyte Symbol	Cu	Zn	Ga	Ge	As	Rb	Sr	Y	Zr	Nb	Mo	Ag	In		
Unit Symbol	ppm	ppm	ppm	ppm	ppm	ppm	ppm	ppm	ppm	ppm	ppm	ppm	ppm	ppm	ppm
Detection Limit	10	30	1	0.5	5	1	2	0.5	1	0.2	2	0.5	0.1		
Analysis Method	FUS-MS	FUS-MS	FUS-MS	FUS-MS	FUS-MS	FUS-MS	FUS-ICP	FUS-MS	FUS-MS	FUS-MS	FUS-MS	FUS-MS	FUS-MS		
EAST SIDE	< 10	70	25	1.6	< 5	358	68	15.9	147	13.9	4	< 0.5	< 0.1		
WEST SIDE	< 10	70	24	1.5	9	352	67	15.9	146	12.7	< 2	< 0.5	< 0.1		
PAVER	< 10	110	25	1.8	7	349	57	16.9	142	13.1	< 2	< 0.5	< 0.1		
EAST SIDE (CERAMIC)	< 10	80	25	1.7	< 5	355	65	15.7	141	13.3	< 2	< 0.5	< 0.1		
WEST SIDE (CERAMIC)	< 10	60	26	1.4	< 5	357	63	16.3	143	13.9	< 2	< 0.5	< 0.1		
PAVER (CERAMIC)	< 10	80	24	1.6	9	350	53	17.2	140	13.1	< 2	< 0.5	< 0.1		
Analyte Symbol	Sn	Sb	Cs	Ba	La	Ce	Pr	Nd	Sm	Eu	Gd	Tb	Dy		
Unit Symbol	ppm	ppm	ppm	ppm	ppm	ppm	ppm	ppm	ppm	ppm	ppm	ppm	ppm	ppm	ppm
Detection Limit	1	0.2	0.1	3	0.05	0.05	0.01	0.05	0.01	0.005	0.01	0.01	0.01		
Analysis Method	FUS-MS	FUS-MS	FUS-MS	FUS-ICP	FUS-MS	FUS-MS	FUS-MS	FUS-MS	FUS-MS	FUS-MS	FUS-MS	FUS-MS	FUS-MS		
EAST SIDE	12	< 0.2	20.2	287	52.3	116	13	39.9	7.36	0.586	4.79	0.67	2.96		
WEST SIDE	13	< 0.2	17.4	290	52.1	140	11.9	36.6	6.67	0.58	4.14	0.63	2.95		
PAVER	10	< 0.2	14.4	239	47.6	107	12	36.9	6.9	0.505	4.53	0.64	3.03		
EAST SIDE (CERAMIC)	5	< 0.2	21.3	286	48.6	109	12	37.1	7.63	0.636	4.99	0.67	3.01		
WEST SIDE (CERAMIC)	5	< 0.2	18.7	270	45.6	102	11.2	34.5	7.13	0.567	4.85	0.67	3.05		
PAVER (CERAMIC)	10	< 0.2	14.4	227	45.6	99.2	11.3	35.9	6.77	0.499	4	0.61	3.12		
Analyte Symbol	Ho	Er	Tm	Yb	Lu	Hf	Ta	W	Tl	Pb	Bi	Th	U		
Unit Symbol	ppm	ppm	ppm	ppm	ppm	ppm	ppm	ppm	ppm	ppm	ppm	ppm	ppm	ppm	ppm
Detection Limit	0.01	0.01	0.005	0.01	0.002	0.1	0.01	0.5	0.05	5	0.1	0.05	0.01		
Analysis Method	FUS-MS	FUS-MS	FUS-MS	FUS-MS	FUS-MS	FUS-MS	FUS-MS	FUS-MS	FUS-MS	FUS-MS	FUS-MS	FUS-MS	FUS-MS		
EAST SIDE	0.53	1.51	0.206	1.22	0.162	4.3	1.91	1.6	2.61	36	0.1	25.2	11.8		
WEST SIDE	0.52	1.49	0.21	1.22	0.153	4.3	1.85	1.5	2.04	32	4.1	23.3	7.39		
PAVER	0.55	1.54	0.221	1.27	0.17	4.3	1.8	1.6	3	50	0.8	23.4	9.24		
EAST SIDE (CERAMIC)	0.51	1.38	0.196	1.18	0.163	4.2	1.83	1	3.47	31	1.4	26	13.9		
WEST SIDE (CERAMIC)	0.52	1.42	0.201	1.2	0.16	4.4	1.81	1.1	2.15	18	1.4	25	21.2		
PAVER (CERAMIC)	0.56	1.62	0.241	1.39	0.18	4.2	1.77	1.1	2.53	28	6.9	23	20.1		

APPENDIX II

EXPERIMENTAL ROCK CONFIGURATIONS

PING was tested on a total of 10 experimental rock configurations to determine the sensitivity of the instrument to elements necessary for biogenic precursors such as C, O, S, and H and major rock forming elements to help reveal the volatile and organic nature and bulk geochemistry of C-type asteroids and differentiate between different asteroid classes. The 10 experimental rock configuration images, layering grids, PING component spacing measurements, notes, neutron and gamma-ray experimental data logs and post-processed time-sliced data are presented in this appendix. Table 22 lists all of the data acquired using PING on top of the 10 experimental rock configurations.

Table 22. Raw TLIST gamma-ray, thermal and epithermal neutron data collection totals for data acquired with PING on the 10 experimental rock configurations. He1 and He2 refer to the ³He thermal and epithermal neutron detectors. UT stands for the detectors borrowed from the University of Tennessee and Navy stands for the detector borrowed through Stan Hunter from the Navy.

Concord Grey Granite Monument				
Date	HPGe (Bare)	HPGe (Boron Cap)	He1 (UT)	He2 (UT)
10/5/11	4.00hrs	N/A	4.00hrs	4.00hrs
11/1/12	N/A	0.71hrs	N/A	N/A
11/2/12	N/A	8.00hrs	N/A	N/A
11/4/12	N/A	7.50hrs	N/A	N/A
Total (LT):	4.00hrs	16.21hrs	4.00hrs	4.00hrs

Columbia River Basalt Monument				
Date	HPGe (Bare)	HPGe (Boron Cap)	He1 (UT)	He2 (UT)
8/21/11	2.00hrs	N/A	2.02hrs	1.88hrs
8/22/11	5.33hrs	N/A	4.93hrs	5.05hrs
10/9/12	N/A	7.00hrs	N/A	N/A
10/10/12	N/A	8.23hrs	N/A	N/A
Total (LT):	7.33hrs	15.23hrs	6.95hrs	6.93hrs

Asteroid Simulant Configuration				
Date	HPGe (Bare)	HPGe (Boron Cap)	He1 (UT)	He2 (UT)
3/23/12	N/A	6.00hrs	N/A	N/A
3/26/12	N/A	4.30hrs	N/A	N/A
3/29/12	N/A	4.35hrs *	N/A	N/A
3/30/12	N/A	6.00hrs	N/A	N/A
4/6/12	N/A	8.00hrs	N/A	N/A
4/8/12	N/A	2.50hrs	N/A	N/A
4/10/12	N/A	2.00hrs	N/A	N/A
4/11/12	N/A	3.00hrs	N/A	N/A
4/12/12	N/A	N/A	N/A	N/A
8/23/11	2.18hrs	N/A	2.27hrs	2.35hrs
8/24/11	7.90hrs	N/A	7.93hrs	8.17hrs
9/30/11	4.00hrs	N/A	0.67hrs	4.00hrs
Total (LT):	14.08hrs	46.15hrs	10.87hrs	14.52hrs

*Note: Shift in timing data at ~ 83 minutes.

2.1: Basic Configuration for Basalt Substitution with Granite (1"-Poly, 2"-Bas, 1"Poly...) No Granite Substitution, just Basalt and Poly				
Date	HPGe (Bare)	HPGe (Boron Cap)	He1 (UT)	He2 (UT)
2/26/12	N/A	2.50hrs	N/A	N/A
2/27/12	N/A	9.50hrs	N/A	N/A
2/28/12	N/A	9.83hrs	N/A	N/A
3/1/12	N/A	8.83hrs	N/A	N/A
Total (LT):	N/A	30.66hrs	N/A	N/A

2.2: Top Layer of Granite Substituted for Top Layer of Basalt (1"-Poly, 2"-Gran, 1"-Poly, 2"-Bas...)				
Date	HPGe (Bare)	HPGe (Boron Cap)	He1 (UT)	He2 (UT)
3/12/12	N/A	8.00hrs	N/A	N/A
3/13/12	N/A	1.00hrs	N/A	N/A
3/14/12	N/A	8.00hrs	N/A	N/A
3/15/12	N/A	4.00hrs	N/A	N/A
3/21/12	N/A	5.00hrs	N/A	N/A
3/22/12	N/A	10.00hrs	N/A	N/A
Total (LT):	N/A	36.00hrs	N/A	N/A

2.3: Top 2 Layers of Granite Substituted for Top 2 Layers of Basalt (1"-Poly, 2"-Gran, 1"-Poly, 2"-Gran, 1"-Poly, 2"-Bas...)				
Date	HPGe (Bare)	HPGe (Boron Cap)	He1 (UT)	He2 (UT)
2/26/12	N/A	2.50hrs	N/A	N/A
2/27/12	N/A	9.50hrs	N/A	N/A
2/28/12	N/A	9.83hrs	N/A	N/A
3/1/12	N/A	8.83hrs	N/A	N/A
Total (LT):	N/A	30.66hrs	N/A	N/A

Subsurface Ice 1: 1" Layer of Basalt on Top of Asteroid Simulant				
Date	HPGe (Bare)	HPGe (Boron Cap)	He1 (Navy)	He2 (Navy)
4/15/12	N/A	N/A	N/A	4.00hrs
4/16/12	N/A	N/A	N/A	5.98hrs
4/17/12	N/A	5.00hrs	N/A	5.00hrs
4/18/12	N/A	N/A	N/A	1.32hrs
4/19/12	N/A	N/A	5.05hrs	N/A
4/24/12	N/A	3.00hrs	3.00hrs	N/A
4/25/12	N/A	4.10hrs	3.95hrs	N/A
4/30/12	N/A	2.00hrs	N/A	N/A
5/1/12	N/A	0.48hrs	N/A	N/A
5/3/12	N/A	4.00hrs	N/A	N/A
Total:	N/A	18.58hrs	12.00hrs	16.30hrs

Subsurface Ice 2: 2" Layer of Basalt on Top of Asteroid Simulant				
Date	HPGe (Bare)	HPGe (Boron Cap)	He1 (UT)	He2 (UT)
N/A	N/A	N/A	N/A	N/A
Total:	N/A	N/A	N/A	N/A

Subsurface Ice 3: 3" Layer of Basalt on Top of Asteroid Simulant				
Date	HPGe (Bare)	HPGe (Boron Cap)	He1 (Navy)	He2 (Navy)
5/7/12	N/A	4.37hrs	4.47hrs	N/A
5/8/12	N/A	2.82hrs	N/A	N/A
Total:	N/A	7.19hrs	4.47hrs	N/A

The HPGe gamma-ray raw TLIST data logs, and portions of the time-sliced experimental data for inelastic scattering (10-100 μ s), capture (150-650 μ s) and delayed activation and natural radioactivity (650-1000 μ s) for all 10 configurations can be acquired upon request from the author. The raw ".tlist.txt" data log files are in ASCII

format and list the parameters and settings for the gamma ray detector, PNG, Lynx acquisition system settings, and indicate that the master raw data set is in another corresponding “.tlistdata.txt” file. The “.tlistdata.txt” files are in ASCII format and contain two columns listing the channel and time for each recorded event. The “.filtered.txt” files are in ASCII format and contain header information describing the PNG, gamma-ray detector, Lynx acquisition system settings, time slice information, and columns for channel, energy, and counts for either inelastic, capture, or delayed activation and natural activity gamma rays. The thermal and epithermal neutron “.tlistdata.txt” logs are provided in ASCII format. The .PDF filenames provided in the subsections below list the log filenames and first two pages of the time sliced data files for all ten configurations.

Granite

The available data for the Granite configuration is as follows:

- 111005Ge1TLT001.log.pdf
- 121101Ge1TLT001.1.log.pdf, 121101Ge1TLT001.1.capture.filtered.pdf, 121101Ge1TLT001.1.DANA.filtered.pdf, 21101Ge1TLT001.1.inelastic.filtered.pdf
- 121102Ge1TLT001.1.log.pdf, 121102Ge1TLT001.1.capture.filtered.pdf, 121102Ge1TLT001.1.DANA.filtered.pdf, 121102Ge1TLT001.1.inelastic.filtered.pdf
- 121102Ge1TLT001.2.log.pdf, 121102Ge1TLT001.2.capture.filtered.pdf, 121102Ge1TLT001.2.DANA.filtered.pdf, 121102Ge1TLT001.2.inelastic.filtered.pdf
- 121104Ge1TLT001.1.log.pdf, 121104Ge1TLT001.1.capture.filtered.pdf, 121104Ge1TLT001.1.DANA.filtered.pdf, 121104Ge1TLT001.1.inelastic.filtered.pdf
- 121104Ge1TLT001.2.log.pdf, 121104Ge1TLT001.2.capture.filtered.pdf, 121104Ge1TLT001.2.DANA.filtered.pdf, 121104Ge1TLT001.2.inelastic.filtered.pdf

The thermal and epithermal neutron data is listed in the following files:

- 111005He1TLT001.log.pdf
- 111005He2TLT001.log.pdf

Basalt

The available data for the Basalt configuration is as follows:

- 110821Ge1TLT002.log.pdf, 110821Ge1TLT002.1.capture.filtered.pdf, 110821Ge1TLT002.1.DA.filtered.pdf, 110821Ge1TLT002.1.inelastic.filtered.pdf
- 110821Ge1TLT003.log.pdf, 110821Ge1TLT003.1.capture.filtered.pdf, 110821Ge1TLT003.1.DA.filtered.pdf, 110821Ge1TLT003.1.inelastic.filtered.pdf
- 110822Ge1TLT005.log.pdf, 110822Ge1TLT005.1.capture.filtered.pdf, 110822Ge1TLT005.1.DA.filtered.pdf, 110822Ge1TLT005.1.inelastic.filtered.pdf
- 110822Ge1TLT006.log.pdf, 110822Ge1TLT006.1.capture.filtered.pdf, 110822Ge1TLT006.1.DA.filtered.pdf, 110822Ge1TLT006.1.inelastic.filtered.pdf
- 110822Ge1TLT008.log.pdf, 110822Ge1TLT008.1.capture.filtered.pdf, 110822Ge1TLT008.1.DA.filtered.pdf, 110822Ge1TLT008.1.inelastic.filtered.pdf
- 110822Ge1TLT009.log.pdf, 110822Ge1TLT009.1.capture.filtered.pdf, 110822Ge1TLT009.1.DA.filtered.pdf, 110822Ge1TLT009.1.inelastic.filtered.pdf
- 110822Ge1TLT010.log.pdf, 110822Ge1TLT010.1.capture.filtered.pdf, 110822Ge1TLT010.1.DA.filtered.pdf, 110822Ge1TLT010.1.inelastic.filtered.pdf
- 121009Ge1TLT002.log.pdf, 121009Ge1TLT002.capture.filtered.pdf, 121009Ge1TLT002.DANA.filtered.pdf, 121009Ge1TLT002.inelastic.filtered.pdf
- 121009Ge1TLT003.log.pdf, 121009Ge1TLT003.capture.filtered.pdf, 121009Ge1TLT003.DANA.filtered.pdf, 121009Ge1TLT003.inelastic.filtered.pdf
- 121010Ge1TLT001.log.pdf, 121010Ge1TLT001.capture.filtered.pdf, 121010Ge1TLT001.DANA.filtered.pdf, 121010Ge1TLT001.inelastic.filtered.pdf
- 121010Ge1TLT002.log.pdf, 121010Ge1TLT002.capture.filtered.pdf, 121010Ge1TLT002.DANA.filtered.pdf, 121010Ge1TLT002.inelastic.filtered.pdf
- 121010Ge1TLT003.log.pdf, 121010Ge1TLT003.capture.filtered.pdf, 121010Ge1TLT003.DANA.filtered.pdf, 121010Ge1TLT003.inelastic.filtered.pdf

- 121010Ge1TLT004.log.pdf, 121010Ge1TLT004.capture.filtered.pdf, 121010Ge1TLT004.DANA.filtered.pdf, 121010Ge1TLT004.inelastic.filtered.pdf
- 121010Ge1TLT005.log.pdf, 121010Ge1TLT005.capture.filtered.pdf, 121010Ge1TLT005.DANA.filtered.pdf, 121010Ge1TLT005.inelastic.filtered.pdf
- 121010Ge1TLT006.log.pdf, 121010Ge1TLT006.capture.filtered.pdf, 121010Ge1TLT006.DANA.filtered.pdf, 121010Ge1TLT006.inelastic.filtered.pdf
- 121010Ge1TLT007.log.pdf, 121010Ge1TLT007.capture.filtered.pdf, 121010Ge1TLT007.DANA.filtered.pdf, 121010Ge1TLT007.inelastic.filtered.pdf
- 121010Ge1TLT009.log.pdf, 121010Ge1TLT009.capture.filtered.pdf, 121010Ge1TLT009.DANA.filtered.pdf, 121010Ge1TLT009.inelastic.filtered.pdf

The thermal and epithermal neutron data is listed in the following files:

- 110821He1TLT002.log.pdf, 110821He1TLT003.log.pdf, 110822He1TLT003.log.pdf, 110822He1TLT005.log.pdf, 110822He1TLT006.log.pdf, 110822He1TLT007.log.pdf,
- 110821He2TLT002.log.pdf, 110821He2TLT003.log.pdf, 110822He2TLT003.log.pdf, 110822He2TLT005.log.pdf, 110822He2TLT006.log.pdf, 110822He2TLT007.log.pdf.

Asteroid

The available data for the Asteroid configuration is as follows:

- 110823Ge1TLT001.log.pdf, 110823Ge1TLT001.Capture.filtered.pdf, 110823Ge1TLT001.DANA.filtered.pdf, 110823Ge1TLT001.Inelastic.filtered.pdf
- 110823Ge1TLT002.log.pdf, 110823Ge1TLT002.Capture.filtered.pdf, 110823Ge1TLT002.DANA.filtered.pdf, 110823Ge1TLT002.Inelastic.filtered.pdf
- 110824Ge1TLT001.log.pdf, 110824Ge1TLT001.Capture.filtered.pdf, 110824Ge1TLT001.DANA.filtered.pdf, 110824Ge1TLT001.Inelastic.filtered.pdf
- 110824Ge1TLT002.log.pdf, 110824Ge1TLT002.Capture.filtered.pdf, 110824Ge1TLT002.DANA.filtered.pdf, 110824Ge1TLT002.Inelastic.filtered.pdf
- 110824Ge1TLT003.log.pdf, 110824Ge1TLT003.Capture.filtered.pdf, 110824Ge1TLT003.DANA.filtered.pdf, 110824Ge1TLT003.Inelastic.filtered.pdf
- 110824Ge1TLT004.log.pdf, 110824Ge1TLT004.Capture.filtered.pdf, 110824Ge1TLT004.DANA.filtered.pdf, 110824Ge1TLT004.Inelastic.filtered.pdf

- 110824Ge1TLT005.log.pdf, 110824Ge1TLT005.Capture.filtered.pdf, 110824Ge1TLT005.DANA.filtered.pdf, 110824Ge1TLT005.Inelastic.filtered.pdf
- 110824Ge1TLT006.1.log.pdf, 110824Ge1TLT006.1.Capture.filtered.pdf, 110824Ge1TLT006.1.DANA.filtered.pdf, 110824Ge1TLT006.1.Inelastic.filtered.pdf
- 110824Ge1TLT006.log.pdf, 110824Ge1TLT006.Capture.filtered.pdf, 110824Ge1TLT006.DANA.filtered.pdf, 110824Ge1TLT006.Inelastic.filtered.pdf
- 110824Ge1TLT007.log.pdf, 110824Ge1TLT007.Capture.filtered.pdf, 110824Ge1TLT007.DANA.filtered.pdf, 110824Ge1TLT007.Inelastic.filtered.pdf
- 110824Ge1TLT008.log.pdf
- 110930Ge1TLT001.log.pdf, 110930Ge1TLT001.Capture.filtered.pdf, 110930Ge1TLT001.DANA.filtered.pdf, 110930Ge1TLT001.Inelastic.filtered.pdf
- 120323Ge1TLT001.log.pdf, 120323Ge1TLT001.capture.filtered.pdf, 120323Ge1TLT001.DANA.filtered.pdf, 120323Ge1TLT001.inelastic.filtered.pdf
- 120323Ge1TLT002.log.pdf, 120323Ge1TLT002.capture.filtered.pdf, 120323Ge1TLT002.DANA.filtered.pdf, 120323Ge1TLT002.inelastic.filtered.pdf
- 120326Ge1TLT001.1.log.pdf, 120326Ge1TLT001.1.capture.filtered.pdf, 120326Ge1TLT001.1.DANA.filtered.pdf, 120326Ge1TLT001.1.inelastic.filtered.pdf
- 120326Ge1TLT001.2.log.pdf, 120326Ge1TLT001.2.capture.filtered.pdf, 120326Ge1TLT001.2.DANA.filtered.pdf, 120326Ge1TLT001.2.inelastic.filtered.pdf
- 120329Ge1TLT001.1.log.pdf, 120329Ge1TLT001.1.capture.filtered.pdf, 120329Ge1TLT001.1.DANA.filtered.pdf, 120329Ge1TLT001.1.inelastic.filtered.pdf
- 120329Ge1TLT001.2.log.pdf, 120329Ge1TLT001.2.capture.filtered.pdf, 120329Ge1TLT001.2.DANA.filtered.pdf, 120329Ge1TLT001.2.inelastic.filtered.pdf
- 120330Ge1TLT001.1.log.pdf, 120330Ge1TLT001.1.capture.filtered.pdf, 120330Ge1TLT001.1.DANA.filtered.pdf, 120330Ge1TLT001.1.inelastic.filtered.pdf
- 120330Ge1TLT001.2.log.pdf, 120330Ge1TLT001.2.capture.filtered.pdf, 120330Ge1TLT001.2.DANA.filtered.pdf, 120330Ge1TLT001.2.inelastic.filtered.pdf
- 120406Ge1TLT001.1.log.pdf, 120406Ge1TLT001.1.capture.filtered.pdf, 120406Ge1TLT001.1.DANA.filtered.pdf, 120406Ge1TLT001.1.inelastic.filtered.pdf

- 120406Ge1TLT001.2.log.pdf, 120406Ge1TLT001.2.capture.filtered.pdf, 120406Ge1TLT001.2.DANA.filtered.pdf, 120406Ge1TLT001.2.inelastic.filtered.pdf
- 120408Ge1TLT001.log.pdf, 120408Ge1TLT001.capture.filtered.pdf, 120408Ge1TLT001.DANA.filtered.pdf, 120408Ge1TLT001.inelastic.filtered.pdf
- 120410Ge1TLT001.log.pdf, 120410Ge1TLT001.capture.filtered.pdf, 120410Ge1TLT001.DANA.filtered.pdf, 120410Ge1TLT001.inelastic.filtered.pdf
- 120411Ge1TLT001.log.pdf, 120411Ge1TLT001.capture.filtered.pdf, 120411Ge1TLT001.DANA.filtered.pdf, 120411Ge1TLT001.inelastic.filtered.pdf
- 120412Ge1TLT001.1.log.pdf

- 120412Ge1TLT002.log.pdf

The thermal and epithermal neutron data is listed in the following files:

- 110823He1TLT001.log.pdf, 110823He1TLT002.log.pdf, 110824He1TLT001.log.pdf, 110824He1TLT002.log.pdf, 110824He1TLT003.log.pdf, 110824He1TLT004.log.pdf, 110824He1TLT005.log.pdf, 110824He1TLT006.1.log.pdf, 110824He1TLT006.log.pdf, 110824He1TLT007.log.pdf, 110824He1TLT008.log.pdf, 110930He1TLT002.log.pdf, 110930He1TLT003.log.pdf, 110930He1TLT005.log.pdf, 110930He1TLT006.log.pdf, 120406He1TLT001.1.log.pdf, 120406He1TLT001.2.log.pdf
- 110823He2TLT001.log.pdf, 110823He2TLT002.log.pdf, 110824He2TLT001.log.pdf, 110824He2TLT002.log.pdf, 110824He2TLT003.log.pdf, 110824He2TLT004.log.pdf, 110824He2TLT005.log.pdf, 110824He2TLT006.1.log.pdf, 110824He2TLT006.log.pdf, 110824He2TLT007.log.pdf, 110824He2TLT008.log.pdf, 110930He2TLT001.log.pdf, 120410He2TLT001.log.pdf, 120411He2TLT001.log.pdf, 120412He2TLT001.1.log.pdf, 120412He2TLT004.log.pdf

2.1

The available data for the 2.1 configuration is as follows:

- 120226Ge1TLT001.log.pdf, 120226Ge1TLT001.capture.filtered.pdf, 120226Ge1TLT001.DANA.filtered.pdf, 120226Ge1TLT001.inelastic.filtered.pdf
- 120227Ge1TLT001.1.log.pdf, 120227Ge1TLT001.1.capture.filtered.pdf, 120227Ge1TLT001.1.DANA.filtered.pdf, 120227Ge1TLT001.1.inelastic.filtered.pdf

- 120227Ge1TLT001.2.log.pdf, 120227Ge1TLT001.2.capture.filtered.pdf, 120227Ge1TLT001.2.DANA.filtered.pdf, 120227Ge1TLT001.2.inelastic.filtered.pdf
- 120227Ge1TLT002.log.pdf, 120227Ge1TLT002.capture.filtered.pdf, 120227Ge1TLT002.DANA.filtered.pdf, 120227Ge1TLT002.inelastic.filtered.pdf
- 120227Ge1TLT003.log.pdf, 120227Ge1TLT003.capture.filtered.pdf, 120227Ge1TLT003.DANA.filtered.pdf, 120227Ge1TLT003.inelastic.filtered.pdf
- 120228Ge1TLT001.1.log.pdf, 120228Ge1TLT001.1.capture.filtered.pdf, 120228Ge1TLT001.1.DANA.filtered.pdf, 120228Ge1TLT001.1.inelastic.filtered.pdf
- 120228Ge1TLT001.2.log.pdf, 120228Ge1TLT001.2.capture.filtered.pdf, 120228Ge1TLT001.2.DANA.filtered.pdf, 120228Ge1TLT001.2.inelastic.filtered.pdf
- 120228Ge1TLT002.log.pdf, 120228Ge1TLT002.capture.filtered.pdf, 120228Ge1TLT002.DANA.filtered.pdf, 120228Ge1TLT002.inelastic.filtered.pdf
- 120228Ge1TLT003.log.pdf, 120228Ge1TLT003.capture.filtered.pdf, 120228Ge1TLT003.DANA.filtered.pdf, 120228Ge1TLT003.inelastic.filtered.pdf
- 120301Ge1TLT001.1.log.pdf, 120301Ge1TLT001.1.capture.filtered.pdf, 120301Ge1TLT001.1.DANA.filtered.pdf, 120301Ge1TLT001.1.inelastic.filtered.pdf
- 120301Ge1TLT001.log.pdf, 120301Ge1TLT001.capture.filtered.pdf, 120301Ge1TLT001.DANA.filtered.pdf, 120301Ge1TLT001.inelastic.filtered.pdf
- 120301Ge1TLT003.log.pdf, 120301Ge1TLT003.capture.filtered.pdf, 120301Ge1TLT003.DANA.filtered.pdf, 120301Ge1TLT003.inelastic.filtered.pdf

2.2

The available data for the 2.2 configuration is as follows:

- 120312Ge1TLT001.1.log.pdf, 120312Ge1TLT001.1.capture.17.150-650us.filtered.pdf, 120312Ge1TLT001.1.inelastic.filtered.pdf, 120312Ge1TLT001.2.capture.17.150-650us.filtered.pdf
- 120312Ge1TLT001.2.log.pdf, 120312Ge1TLT001.2.DA+NA.17.650.1-999.9us.filtered.pdf, 120312Ge1TLT001.2.inelastic.filtered.pdf, 120312Ge1TLT001.1.DA+NA.17.650.1-999.9us.filtered.pdf
- 120313Ge1TLT001.log.pdf, 120313Ge1TLT001.capture.16.2.150-650us.filtered.pdf, 120313Ge1TLT001.DA+NA.16.2.650.1-999.9us.filtered.pdf, 120313Ge1TLT001.inelastic.filtered.pdf

- 120314Ge1TLT001.1.log.pdf, 120314Ge1TLT001.1.DA+NA.17.9.650.1-999.9us.filtered.pdf, 120314Ge1TLT001.1.inelastic.filtered.pdf, 120314Ge1TLT001.2.capture.17.9.150-650us.filtered.pdf
- 120314Ge1TLT001.2.log.pdf, 120314Ge1TLT001.2.DA+NA.17.9.650.1-999.9us.filtered.pdf, 120314Ge1TLT001.2.inelastic.filtered.pdf, 120314Ge1TLT001.capture.17.9.150-650us.filtered.pdf
- 120315Ge1TLT001.1.log.pdf, 120315Ge1TLT001.1.capture.18.150-650us.filtered.pdf, 120315Ge1TLT001.1.DA+NA.18.650.1-999.9us.filtered.pdf, 120315Ge1TLT001.1.inelastic.filtered.pdf
- 120321Ge1TLT001.1.log.pdf, 120321Ge1TLT001.1.capture.17.150-650us.filtered.pdf, 120321Ge1TLT001.1.DA+NA.17.650.1-999.9us.filtered.pdf, 120321Ge1TLT001.1.inelastic.filtered.pdf
- 120321Ge1TLT001.2.log.pdf, 120321Ge1TLT001.2.capture.17.150-650us.filtered.pdf, 120321Ge1TLT001.2.DA+NA.17.650.1-999.9us.filtered.pdf, 120321Ge1TLT001.2.inelastic.filtered.pdf
- 120322Ge1TLT001.1.log.pdf, 120322Ge1TLT001.1.capture.18.150-650us.filtered.pdf, 120322Ge1TLT001.1.DA+NA.18.650.1-999.9us.filtered.pdf, 120322Ge1TLT001.1.inelastic.filtered.pdf
- 120322Ge1TLT001.2.log.pdf, 120322Ge1TLT001.2.capture.18.3.150-650us.filtered.pdf, 120322Ge1TLT001.2.DA+NA.18.3.650.1-999.9us.filtered.pdf, 120322Ge1TLT001.2.inelastic.filtered.pdf
- 120322Ge1TLT002.log.pdf, 120322Ge1TLT002.capture.18.3.150-650us.filtered.pdf, 120322Ge1TLT002.DA+NA.18.3.650.1-999.9us.filtered.pdf, 120322Ge1TLT002.inelastic.filtered.pdf

2.3

The available data for the 2.3 configuration is as follows:

- 120302Ge1TLT001.log.pdf, 120302Ge1TLT001.capture.16.150-650us.filtered.pdf, 120302Ge1TLT001.DANA.16.650.1-999.9us.filtered.pdf, 120302Ge1TLT001.inelastic.filtered.pdf
- 120305Ge1TLT003.log.pdf, 120305Ge1TLT003.capture.17.3.150-650us.filtered.pdf, 120305Ge1TLT003.DANA.17.3.650.1-999.9us.filtered.pdf, 120305Ge1TLT003.inelastic.filtered.pdf
- 120305Ge1TLT004.log.pdf, 120305Ge1TLT004.capture.17.3.150-650us.filtered.pdf, 120305Ge1TLT004.DANA.17.3.650.1-999.9us.filtered.pdf, 120305Ge1TLT004.inelastic.filtered.pdf

- 120306Ge1TLT001.1.log.pdf, 120306Ge1TLT001.1.capture.17.1.150-650us.filtered.pdf, 120306Ge1TLT001.1.DANA.17.1.650.1-999.9us.filtered.pdf, 120306Ge1TLT001.1.inelastic.filtered.pdf
- 120306Ge1TLT001.2.log.pdf, 120306Ge1TLT001.2.capture.17.1.150-650us.filtered.pdf, 120306Ge1TLT001.2.DANA.17.1.650.1-999.9us.filtered.pdf, 120306Ge1TLT001.2.inelastic.filtered.pdf
- 120306Ge1TLT002.log.pdf, 120306Ge1TLT002.capture.17.1.150-650us.filtered.pdf, 120306Ge1TLT002.DANA.17.1.650.1-999.9us.filtered.pdf, 120306Ge1TLT002.inelastic.filtered.pdf
- 120307Ge1TLT001.1.log.pdf, 120307Ge1TLT001.1.capture.17.4.150-650us.filtered.pdf, 120307Ge1TLT001.1.DANA.17.4.650.1-999.9us.filtered.pdf, 120307Ge1TLT001.inelastic.filtered.pdf
- 120307Ge1TLT003.log.pdf, 120307Ge1TLT003.capture.17.1.150-650us.filtered.pdf, 120307Ge1TLT003.DANA.17.1.650.1-999.9us.filtered.pdf, 120307Ge1TLT003.inelastic.filtered.pdf
- 120309Ge1TLT001.1.log.pdf, 120309Ge1TLT001.1.capture.15.9.150-650us.filtered.pdf, 120309Ge1TLT001.1.DANA.15.9.650.1-999.9us.filtered.pdf, 120309Ge1TLT001.1.inelastic.filtered.pdf
- 120309Ge1TLT002.1.log.pdf, 120309Ge1TLT002.1.capture.17.2.150-650us.filtered.pdf, 120309Ge1TLT002.1.DANA.17.2.650.1-999.9us.filtered.pdf, 120309Ge1TLT002.1.inelastic.filtered.pdf
- 120309Ge1TLT002.2.log.pdf, 120309Ge1TLT002.2.capture.17.1.150-650us.filtered.pdf, 120309Ge1TLT002.2.DANA.17.1.650.1-999.9us.filtered.pdf, 120309Ge1TLT002.2.inelastic.filtered.pdf
- 120309Ge1TLT003.log.pdf, 120309Ge1TLT003.capture.17.6.150-650us.filtered.pdf, 120309Ge1TLT003.DANA.17.6.650.1-999.9us.filtered.pdf, 120309Ge1TLT003.inelastic.filtered.pdf
- 120305LB1TLT001.log.pdf, 120305LB1TLT003.log.pdf, 120305LB1TLT005.log.pdf

The thermal and epithermal neutron data is listed in the following files:

- 120305He1TLT002.log.pdf, 120305He1TLT003.log.pdf, 120305He1TLT006.log.pdf

Ice 1

The available data for the Ice 1 configuration is as follows:

- 120416Ge1TLT001.log.pdf
- 120417Ge1TLT001.log.pdf, 120417Ge1TLT001.capture.filtered.pdf, 120417Ge1TLT001.DANA.filtered.pdf, 120417Ge1TLT001.inelastic.filtered.pdf
- 120417Ge1TLT002.log.pdf, 120417Ge1TLT002.capture.filtered.pdf, 120417Ge1TLT002.DANA.filtered.pdf, 120417Ge1TLT002.inelastic.filtered.pdf
- 120418Ge1TLT001.log.pdf
- 120419Ge1TLT001.log.pdf
- 120419Ge1TLT002.log.pdf
- 120424Ge1TLT001.log.pdf, 120424Ge1TLT001.capture.filtered.pdf, 120424Ge1TLT001.DANA.filtered.pdf, 120424Ge1TLT001.inelastic.filtered.pdf
- 120425Ge1TLT002.log.pdf, 120425Ge1TLT002.capture.filtered.pdf, 120425Ge1TLT002.DANA.filtered.pdf, 120425Ge1TLT002.inelastic.filtered.pdf
- 120425Ge1TLT005.log.pdf, 120425Ge1TLT005.capture.filtered.pdf, 120425Ge1TLT005.DANA.filtered.pdf, 120425Ge1TLT005.inelastic.filtered.pdf
- 120429Ge1TLT001.log.pdf
- 120430Ge1TLT001.log.pdf, 120430Ge1TLT001.capture.filtered.pdf, 120430Ge1TLT001.DANA.filtered.pdf, 120430Ge1TLT001.inelastic.filtered.pdf
- 120501Ge1TLT001.1.log.pdf, 120501Ge1TLT001.1.capture.filtered.pdf, 120501Ge1TLT001.1.DANA.filtered.pdf, 120501Ge1TLT001.1.inelastic.filtered.pdf
- 120503Ge1TLT001.log.pdf, 120503Ge1TLT001.capture.filtered.pdf, 120503Ge1TLT001.DANA.filtered.pdf, 120503Ge1TLT001.inelastic.filtered.pdf

The thermal and epithermal neutron data is listed in the following files:

- 120419He1TLT001.log.pdf, 120419He1TLT002.log.pdf, 120424He1TLT001.log.pdf, 120425He1TLT002.log.pdf, 120425He1TLT005.log.pdf, 120425He1TLT007.log.pdf, 120429He1TLT001.log.pdf, 120429He1TLT002.log.pdf

- 120415He2TLT001.log.pdf, 120416He2TLT001.log.pdf, 120416He2TLT002.log.pdf, 120417He2TLT001.log.pdf, 120417He2TLT002.log.pdf, 120418He2TLT001.log.pdf

Ice 2

The experimental configuration was constructed; however, due to time constraints, no data was collected. Data will be collected in the future for this configuration.

Ice 3

The available data for the Ice 3 configuration is as follows:

- 120507Ge1TLT001.1.log.pdf, 120507Ge1TLT001.1.capture.filtered.pdf, 120507Ge1TLT001.1.DANA.filtered.pdf, 120507Ge1TLT001.1.inelastic.filtered.pdf,
- 120507Ge1TLT001.2.log.pdf, 120507Ge1TLT001.2.capture.filtered.pdf, 120507Ge1TLT001.2.DANA.filtered.pdf, 120507Ge1TLT001.2.inelastic.filtered.pdf,
- 120508Ge1TLT001.1.log.pdf, 120508Ge1TLT001.1.capture.filtered.pdf, 120508Ge1TLT001.1.DANA.filtered.pdf, 120508Ge1TLT001.1.inelastic.filtered.pdf,

The thermal and epithermal neutron data is listed in the following files:

- 120507He1TLT001.1.log.pdf
- 120507He1TLT001.2.log.pdf

Concord Grey Granite Monument

Concord Grey Granite PING Experimental Configuration

Figure 47 shows a picture of the PING instrument set-up on top of the Concord Grey granite monument. The PNG is on the left hand side of the granite monument, followed by the epithermal and thermal He-3 neutron detectors in the center, and the HPGe detector on the right hand side of the granite. See Figure 50 for PING equipment dimensions and spacing.



Figure 47. Image of the PING instrument prototype on top of the Concord Grey Granite monument.

Columbia River Basalt Monument

Columbia River Basalt PING Experimental Configuration

Figure 48 shows an image of the PING instrument set-up on top of the Columbia River Basalt monument. The PNG is on the left hand side of the basalt monument, followed by the epithermal and thermal He-3 neutron detectors in the center, and the HPGe detector on the righthand side of the basalt. Figure 49 is a schematic of the dimensions of the Columbia River basalt monument. Figure 50 is a sketch of the dimensions, distance, and spacing of the PING components from one another, and Figure 51 are additional notes taken during the experiment.

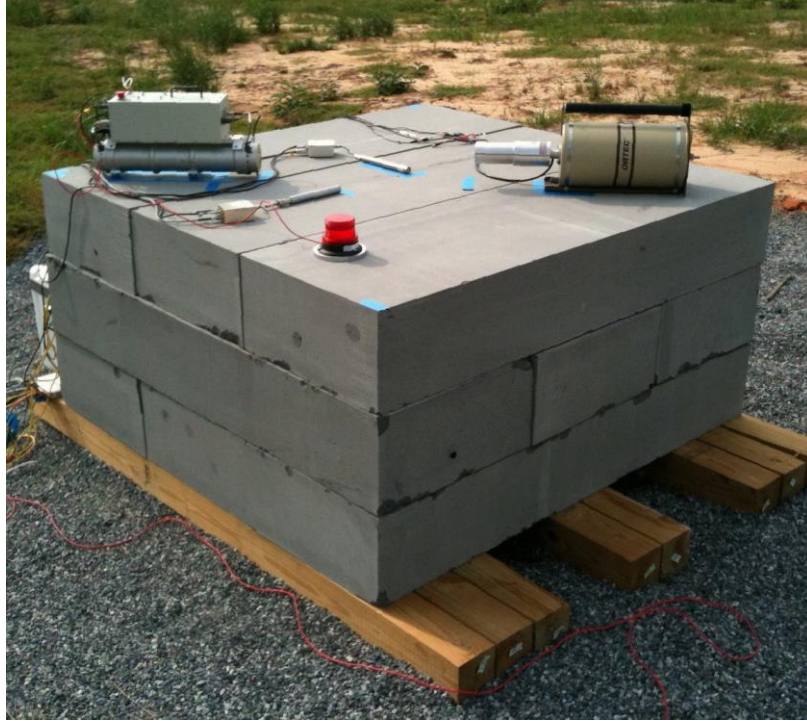


Figure 48. Image of the PING instrument prototype on top of the Columbia River Basalt monuement taken on 08/21/2012.

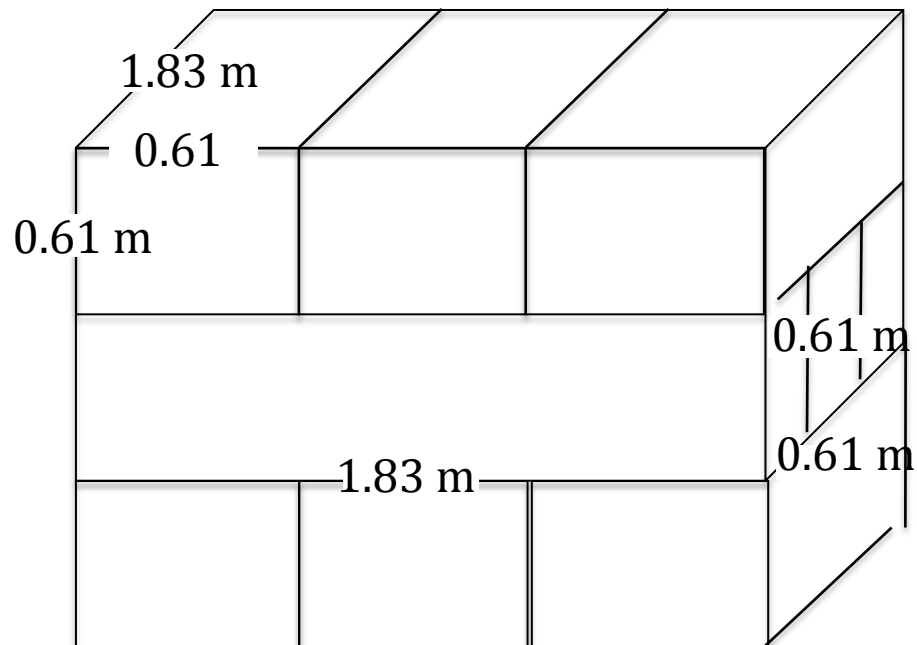


Figure 49. Schematic of the Columbia River Basalt monument dimensions.

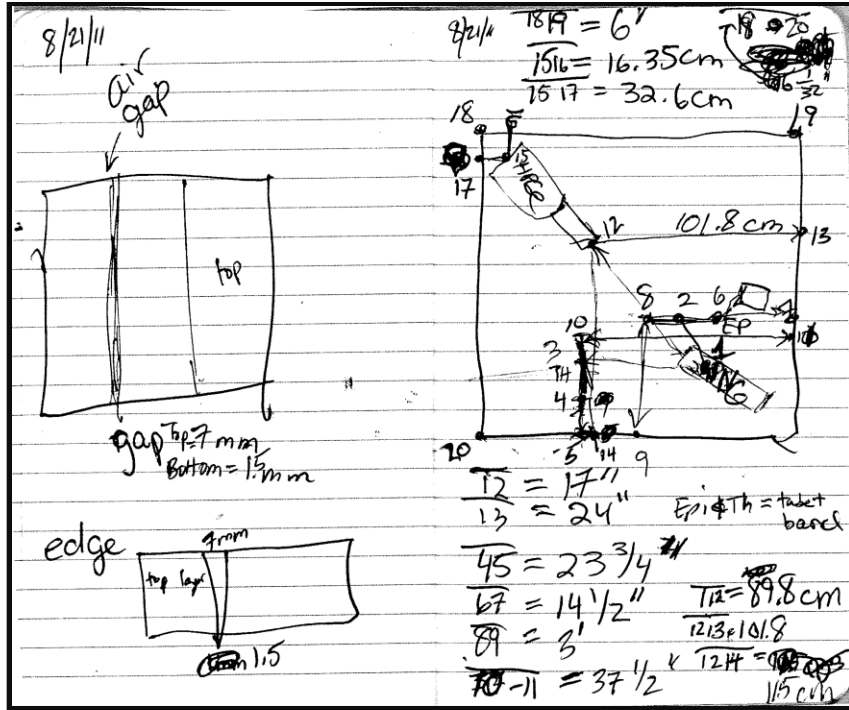


Figure 50. Sketch of the PING equipment spacing used for all experiments.

8/21/11
 n^o ball neutron survey
 Jeff Schweitzer
 path by building 550 nR in 2 min
 Basalt side 256 nR in 2 min
 side near woods 75 nR in 2 min
 side away from basalt + 0 nR in 2 min
 repeat path 550 nR in 2 min
 HPGE
 → TLT 001 002
 bad → used external clock sync & slave
 → PHA test for aliveness

Hel & HeZ
 → TLT 001 002
 bad • HV @ 600
 used external clock
 used slave on should be internal clock
 → PHA 001
 ↳ aliveness test
 of Run time into scan

Def	CPS	DT
HE1 Thord	130-175	20-26%
HE2 Epi	210-302	24-31%
HPGE	6200-64192%	

Figure 51. Notes from the basalt monument PING experiment.

Asteroid Simulant

Asteroid Simulant PING Experimental Configuration

Figure 52 shows a picture of the PING instrument set-up on top of the asteroid simulant. The PING is on the left hand side of the configuration, followed by the epithermal and thermal He-3 neutron detectors in the center, and the HPGe detector on the right hand side of the simulant. See Figure 50 for PING dimensions and spacing.

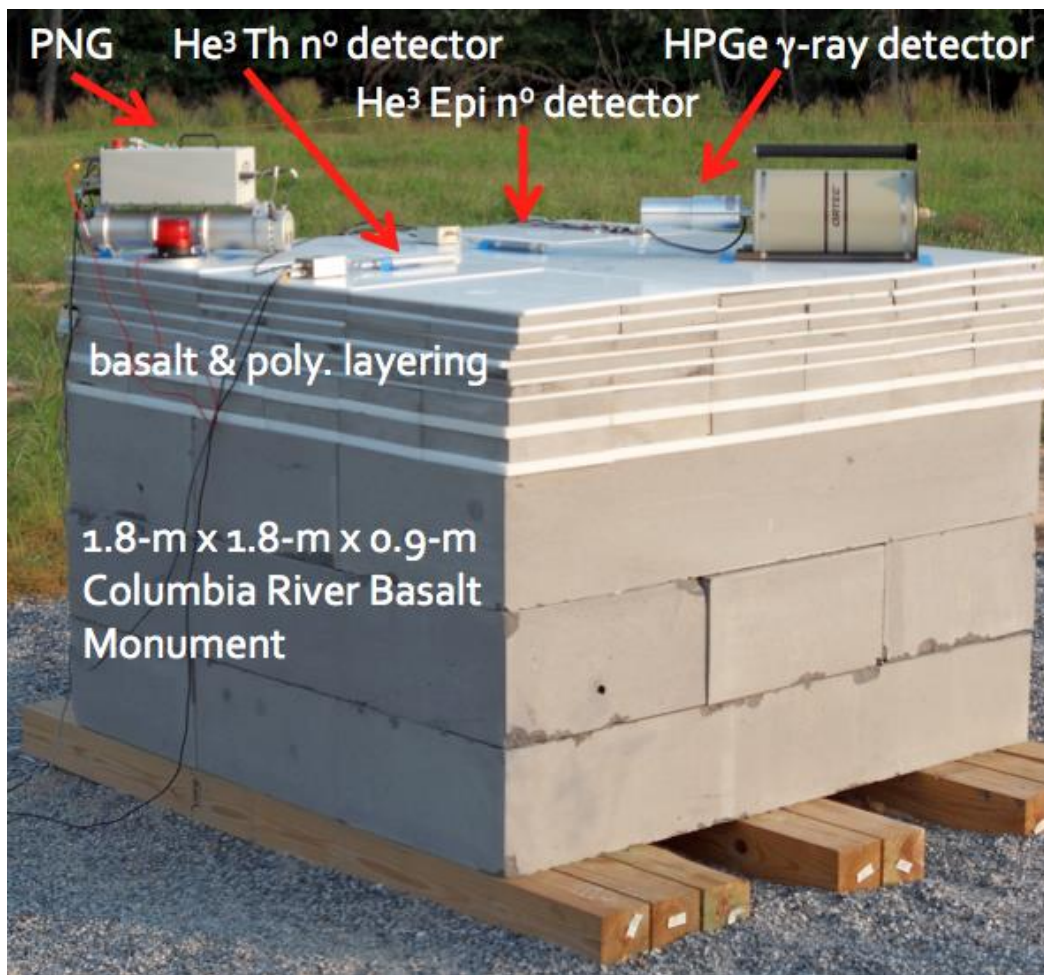


Figure 52. Image of the PING instrument on the layered asteroid simulant.

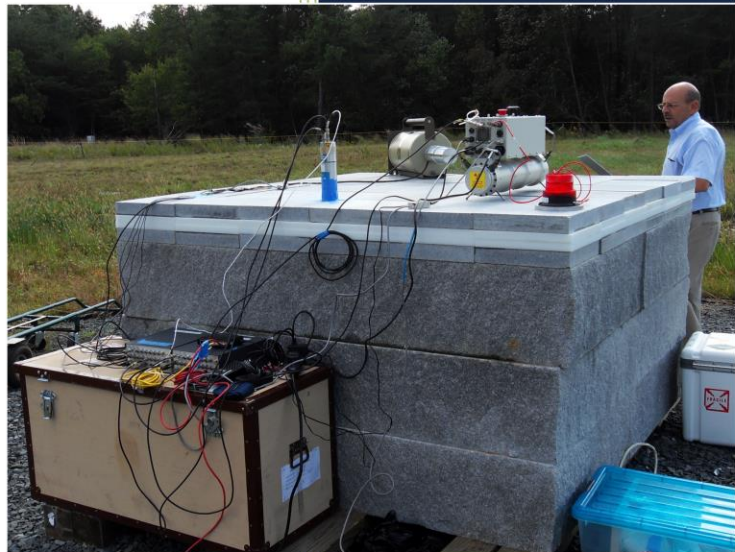
APPENDIX III

PING EXPERIMENT OPERATIONS MANUALS

The following two manuals explain the basic experimental operations for conducting PING experiments at the GGAO test facility.

2011

NASA GGAO Outdoor Test Site Experiment Operations Manual



Julia G. Bodnarik
NASA Goddard Space Flight Center
Code 691
02/04/2011

Table of Contents

Equipment and Monument Preparations	3
Necessary Experiment Equipment.....	3
Uncover the Monument.....	3
Take Equipment to the Monument.....	3
Setup the Power, Communication, and PNG Interlock Cables	4
Equipment Setup for PNG Experiments.....	4
Open the PNG GUI	8
Set the Beam Current and HV	9
Setup the Pulser.....	9
Start the PNG.....	10
Standby the PNG	11
Stop the PNG	11

Equipment and Monument Preparations

The steps to prepare the NASA GGAO Planetary Geochemistry Flight Instruments Test Site equipment and the granite or basalt monument to run experiments are as follows:

- 1) **Insure you have all the necessary equipment for your experiment.** The equipment you may be using includes, but is not limited to the following items:
 - a. **Personnel equipment**
 - i. Work gloves
 - ii. Sun screen
 - iii. 40% Deet bug spray (to avoid getting ticks)
 - b. **Power cables and strips**
 - i. 1 orange power cable
 - ii. 2 power strips
 - c. **2 Ethernet switches**
 - d. **2 red Ethernet cables** located on spools inside Building 206 on the telescope platform near the stairs to the right of the door as you enter the building
 - e. **1 gray interlock cable** for PNG kill switch located on a spool inside Building 206 on the telescope platform near the stairs to the right of the door as you enter the building
 - f. **Lynx Digital Signal Analyzers (DSAs)** with power cords (NOTE: The number of Lynx DSAs needed depends on the experiment requirements)
 - g. **MP320 Pulsed Neutron Generator (PNG)** in a white box located near top of the ramp on the telescope platform (Refer to the [MP320 PNG Quick Start Operations Manual](#))
 - h. **Gamma ray and neutron detectors** (NOTE: Depends on the experiment requirements):
 - i. Ortec HPGe solid state gamma ray detector
 - ii. LaBr₃ gamma ray scintillation detector
 - iii. LaCl₃ gamma ray scintillation detector
 - iv. He³ thermal neutron detectors
 - v. He³ epithermal neutron detectors
 - i. **BNC and HV cables** (NOTE: Depends on detectors being used for the experiment)
- 2) **Uncover the Granite or Basalt monument** by removing the rope and the tarp and placing them next to the granite. You will need to recover the granite with the tarp and secure it with the rope when you are finished doing experiments for the day.
- 3) **Take the Equipment to the monument**
 - i. PNG in the white box
 - ii. Radiation detectors (i.e. gamma ray and/or neutron detectors)
 - iii. Lynx DSA(s)
 - iv. Ethernet switches
 - v. BNC, HV, Ethernet, and power cables necessary for the equipment being used

4) Setup the power, communication, and PNG interlock cables

a. Power cable setup:

- i. Take one orange power cable out to the monument and attach one end of the cable into the power outlet box located near the granite monument
- ii. Take the other end of the power cord and attach the short orange power cord with 3 outlet plugs to the power cord
- iii. Attach two power strips to the short orange power cord with 3 outlet plugs and place them next to the granite.

b. Ethernet communication cable setup:

- i. Locate the two red Ethernet cables located on spools inside Building 206 on the telescope platform near the stairs to the right of the door as you enter the building.
- ii. Insure that one Ethernet cable is connected to the second Ethernet port on the back of the Z series main operations computer and the other Ethernet cable is conneted to the second Ethernet port on the back of the Dell backup operations computer.
- iii. Run these cables from the building out to the monument.
- iv. Connect each long red Ethernet cable into its own separate Ethernet switch, by plugging each long red Ethernet cable into one of the Ethernet switch ports labeled numbers 1 through 7 on the Ethernet switch.
- v. Proved power to the Ethernet switches by attaching the Ethernet power cords between the Ethernet Switches and a power strip.

Equipment Setup for PNG Experiments

The steps to setup the equipment to run PNG experiments on the granite or basalt monument are as follows:

- 1) **Setup the PNG on the monument** (Refer to the [MP320 PNG Quick Start Operations Manual](#)).
- 2) **Setup a platform for the electronics** by placing the closed large white PNG container or the large wooden HPGe container next to the monument on top of its wooden 4' x 4' supports.
- 3) **Setup the Lynx DSA(s)**: The quantity of Lynx DSA(s) and their setup will depend on the experiment.
 - a. **Basic setup for a Lynx DSA**: This section only explains how to setup power and communications to a single Lynx DSA without connecting a detector. Detector and acquisition mode specific connections will be explained in subsequent sections of this manual.
 - i. Place the Lynx DSA, the Ethernet switches, and the power strips on top of the large container next to the monument.



Figure 1. Electronics on top of a large container next to the monument.

- ii. Attach the Lynx DSA power cord between the Lynx 12V/1.0 A power connector and one of the power strips.
 - iii. Attach a yellow Ethernet cable between the Lynx connector and one of the available Ethernet switch ports labeled numbers 1 through 7.
- 4) **Setup the Gamma Ray Detector(s):** This section describes how to setup and connect LaBr₃/LaCl₃ and HPGe gamma ray detectors to a Lynx DSA.

a. **Connect a LaBr₃/LaCl₃ gamma ray scintillation detector to a Lynx DSA:**

i. **Locate the +HV, ENERGY and PREAMP connectors on the Lynx DSA.**

The Lynx DSA, shown in Figure 2, has several rear panel connectors of interest including: a +HV SHV connector, a -HV SHV connector, a 9-pin female PREAMP connector, a 12V DC Power connector for the Lynx' AC power adapter, and an Ethernet connector.

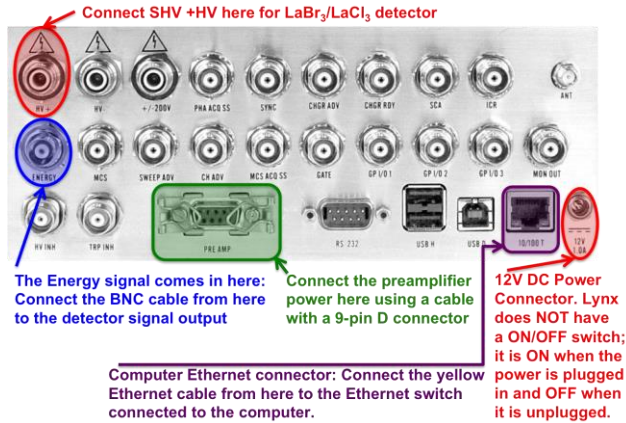


Figure 2. Important Lynx DSA rear panel connectors for the LaBr₃/LaCl₃ detector.

- ii. **Locate the +12V/-12V BR2 preamp female connector, the +HV SHV connector, and a SIGNAL BNC connector on the LaBr₃/LaCl₃ detector preamplifier/voltage divider base, shown in Figure 3.**

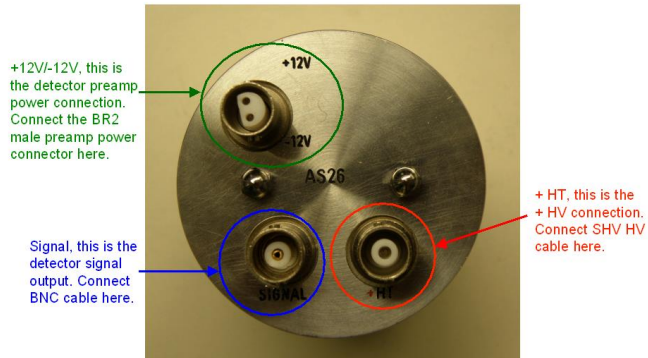


Figure 3: LaBr₃/LaCl preamplifier voltage divider base connection ports.

iii. **Connect the LaBr₃/LaCl₃ detector preamplifier power.**

Connect the cable with the **9-pin male-BR2** connector between the Lynx's **PREAMP** connector and the scintillation detector's preamplifier **+12 V/ -12 V power** connector. The 9-pin male connector end of the cable, shown in Figure 4a, will be connected to the 9-pin female connector labeled PREAMP on the back of the Lynx DSA, shown in Figure 2. The BR2 male connector end of the cable, shown in Figure 4b, will be connected to the +12 V/ -12 V BR2 female connector on the back of the scintillation detector, shown in Figure 3. The **PREAMP** connector on the back of the Lynx includes a bail mechanism that you should use to secure the preamplifier's power cable to the Lynx DSA.



Figure 4. a) Preamp 9-pin male connector, b) Preamp BR2 male connector.

iv. **Connect the LaBr₃/LaCl₃ detector positive (+) HV power.**

The LaBr₃/LaCl₃ detectors require **positive** high voltage power. Connect the SHV cable, shown in Figure 5, between the detector preamp's +HT (a.k.a. +HV) connector, shown in Figure 3, and the Lynx's HV+ connector, shown in Figure 2.

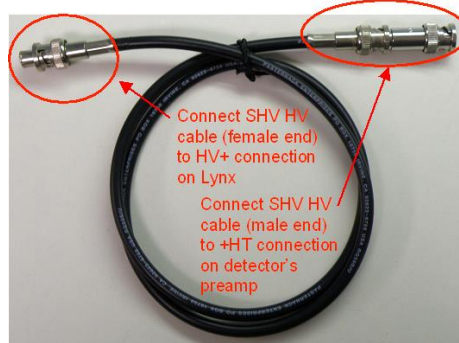


Figure 5: Example of a SHV Cable.

v. **Connect the LaBr₃/LaCl₃ detector BNC gamma ray signal cable to Lynx.**

Connect a BNC cable, shown in Figure 6, from the SIGNAL connector on scintillation detector's preamplifier/voltage divider base, shown in Figure 3, to the ENERGY connector on the back of Lynx, shown in Figure 2.



Figure 6: Example of a BNC cable.

b. Connect a HPGe gamma ray solid state detector to a Lynx DSA:

- i. Locate the **-HV, ENERGY, PREAMP, HV INH, and the TRP INH** connectors on the **Lynx DSA**. The Lynx DSA, shown in Figure 7, has several rear panel connectors of interest including: a + HV SHV connector, a -HV SHV connector, a 9-pin female PREAMP connector, a 12V DC Power connector for the Lynx' AC power adapter, and an Ethernet connector.

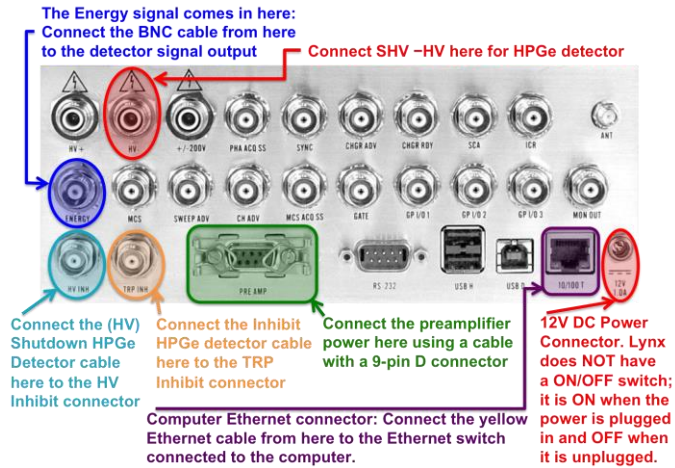


Figure 7. Important Lynx DSA rear panel connectors for the HPGe detector.

- ii. Locate the 9-pin D connector, the -HV SHV connector, the Output 1 BNC connector, the (HV) Shutdown BNC connector, and the Inhibit BNC connector on the HPGe detector.
- iii. Connect the HPGe detector preamplifier power. Connect the HPGe 9-pin D connector cable to the grey 9-pin D extension cable. Connect the grey 9-pin D extension cable to the Lynx's PREAMP connector.
- iv. Connect the HPGe detector negative (-) HV power. Attach a SHV extension cable to the HPGe -HV SHV connector. Connect the other end of the SHV extension cable to the Lynx -HV connector.
- v. Connect the HPGe Output 1, (HV) Shutdown, and the Inhibit BNC connectors to Lynx:
1. Connect a skinny BNC extension cable to **HPGe Output 1 BNC connector**, and connect the other end of the extension cable to the **Energy connector** on Lynx.
 2. Connect a skinny BNC extension cable to **HPGe (HV) Shutdown connector**, and connect the other end of the extension cable to the **HV INH connector** on Lynx.
 3. Connect a skinny BNC extension cable to the **HPGe Inhibit BNC cable**, and connect the other end of the cable to the **TRP INH connector** on Lynx

- 5) **Setup Lynx-to-PNG connections for PNG synchronized data acquisitions.** This section describes the additional connections that to be made between the Lynx DSA and the PNG for PNG synchronized experiments.
- a. **Connect the Lynx DSA to the PNG for PHA Coincidence Acquisitions:**
 - i. **Locate the Lynx GATE and the PNG Source Pulse BNC connectors.** These connectors can be found on the back of a Lynx box and the PNG front electronics.
 - ii. **Connect a BNC cable between the Lynx GATE and the PNG Source Pulse BNC connectors.**
 - b. **Connect the Lynx DSA to the PNG for TLIST Acquisitions:**
 - i. **Locate the Lynx SYNC and the PNG Source Pulse BNC connectors.** These connectors can be found on the back of a Lynx box and the PNG front electronics.
 - ii. **Connect a BNC cable between the Lynx SYNC and the PNG Source Pulse BNC connectors.**
- 6) **Setup for multiple time gate PHA Coincidence Acquisitions.** This section describes how to setup for PNG synchronized Lynx PHA coincidence acquisitions using a HPGe detector and two (2) Lynx boxes.
- a. **Connect the HPGe detector to a Lynx DSA as explained in section 4b on page 7 of this manual.**
 - b. **Connect a BNC cable between the Lynx GATE and the PNG Source Pulse BNC connectors.**
 - c. **Set-up a second Lynx DSA as explained in section 3a on page 4 of this manual.**
 - d. **Connect a skinny BNC extension cable between the HPGe Output 2 cable connector and the Lynx Energy connector on the second Lynx DSA.**
 - e. **Connect a BNC cable between the Lynx GATE on the second Lynx DSA and the PNG Delay Pulse 1 connector.**

2011

MP320 PNG QUICK START OPERATIONS MANUAL



Julia G. Bodnarik
NASA Goddard Space Flight Center
Code 691
02/04/2011

Table of Contents

Pulsed Neutron Generator Setup	3
Connect the Cables to the PNG.....	3
Turn On the Power to the PNG.....	7
Pulsed Neutron Generator Setup	8
Open the PNG GUI.....	8
Set the Beam Current and HV.....	9
Setup the Pulser.....	9
Start the PNG.....	10
Standby the PNG.....	11
Stop the PNG.....	11

Pulsed Neutron Generator Setup

The steps to setup and run the Thermo Scientific MP320 Pulsed Neutron Generator (PNG) are as follows:

- 1) Insure the PNG is setup in a safe area (the GGAO Test Site) consistent with federal regulations and the NASA GSFC Radiation Safety Office approved Radiation Producing Source Operating Procedure (GSFC Form 23-6I, Section 7 for Docket #09-0139). This includes posting radiation hazard signs along the test site 250 foot keep-out perimeter, doing a gamma ray and neutron radiation survey, and having a spotter located outside Building 206 to insure that no one enters the keep-out zone during PNG operations.
- 2) Insure that the PNG controller computer is located a safe distance from the PNG with appropriate shielding. For our purposes the computer is located at GGAO in Building 206 at a safe distance from the PNG when it is being operated on the granite monument at our test facility.
- 3) Insure that you have uncovered the granite or basalt monument, run all necessary cables from Building 206 to the monument, and brought out all necessary equipment for the experiment. Place the PNG on top of the monument.
- 4) Connect the cables to the PNG.
 - a. Insure that the RESERVOIR (J1), SOURCE (J2), HV SIGNAL (J3) and HVPS (J4) cables are connected. All of the PNG connector cables are unique and cannot be inadvertently interchanged.

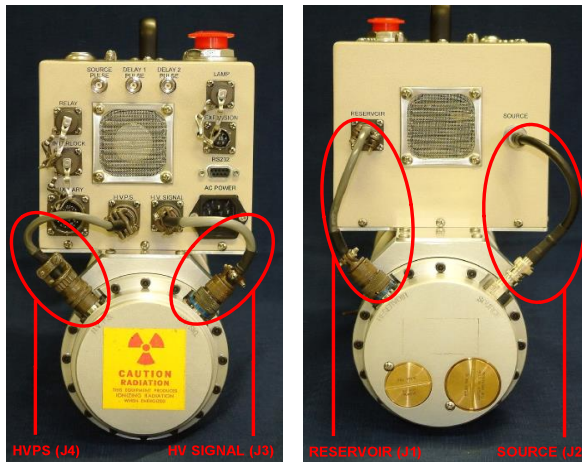


Figure 1. a) Electronics Connector End View

b) Source & Reservoir End View

b. POWER CABLE

Plug the AC power cable into the AC POWER connector on the PNG electronics enclosure.

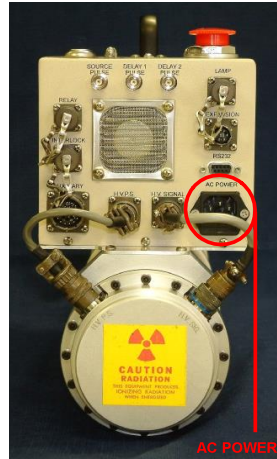


Figure 2. AC Power Connector

c. INTERLOCK CABLE

The ~300 foot gray interlock cable must be connected to the INTERLOCK connector on the PNG electronics enclosure, and the HVPS disable box. Set-up the HVPS disable box inside Building 206 next to the computer. **Insure that the red twist button is pushed down on the HVPS disable box so that neutrons are not inadvertently produce during set-up.** Twist and release the button when you are ready to produce neutrons.

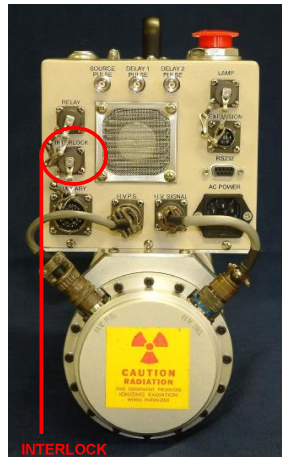
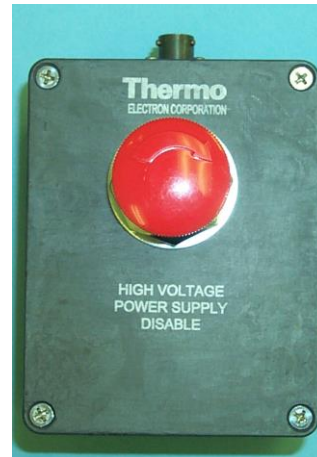


Figure 3. a) Interlock Connector



b) HVPS Disable Box

d. RS232-TO-ETHERNET ADAPTER CABLES

Connect the RS232 end of the RS232-to-Ethernet adapter to the RS232 port on the PNG electronics enclosure. Connect the gray Ethernet cable between the RS232-to-Ethernet adapter and the Ethernet switch to communicate to the host PC.

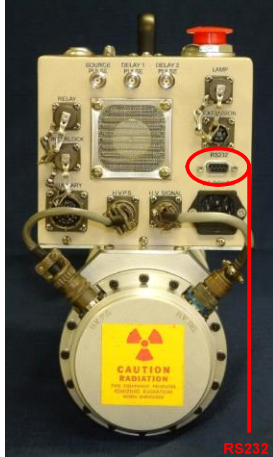


Figure 4. a) RS232 Connector



b) RS232-to-Ethernet Adapter

e. NEUTRON LAMP CABLE

Place the neutron lamp in a visible location on top of the granite or basalt monument at a safe distance from the PNG. The neutron lamp cable must be connected to the LAMP connector on the electronics enclosure for the PNG to run.



Figure 5. a) Lamp connector



b) Neutron Warning Lamp

f. **AUXILIARY JUMPER CABLE**

Insure that the auxiliary jumper cable is attached to the AUXILIARY connector on the electronics enclosure. This must be connected for the PNG to run.

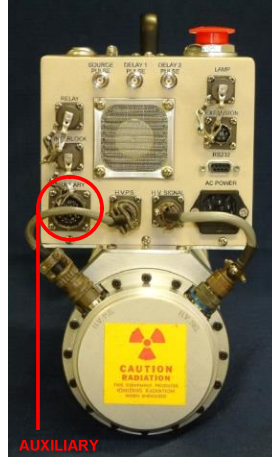


Figure 6. Auxiliary Connector

g. **ADDITIONAL CABLES (SOURCE PULSE & DELAY 1 PULSE CABLES)**

If you are running an experiment that requires synchronization between the PNG pulse and the acquisition electrons, you will want to use the SOURCE PULSE and DELAY 1 PULSE connectors. THE DELAY 2 PULSE connector is not active in our PNG.



Figure 7. Source Pulse and Delay 1 Pulse Connectors

- i. Lynx PHA coincidence acquisition connections: Connect a BNC cable from the SOURCE PULSE or DELAY 1 PULSE connector on the PNG electronics enclosure to the Lynx GATE connector on the back of the Lynx box.

- ii. Lynx PHA synchronization acquisition connections: Connect a BNC cable from the SOURCE PULSE or DELAY 1 PULSE connector on the PNG electronics enclosure to the Lynx SYNC connector on the back of the Lynx box.

5) Turn on the power to the PNG

There is one KEY SWITCH, three LEDs and a locking RED POWER BUTTON located on the top of the PNG electronics enclosure. The steps to turn on power to the PNG are as follows:

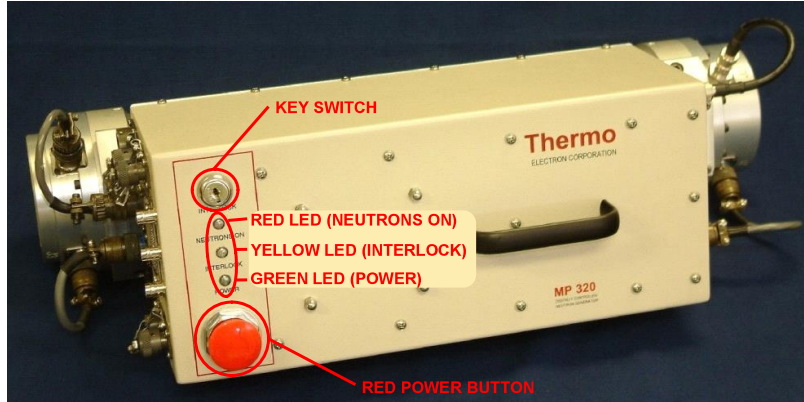


Figure 8. PNG Top View

- a. Turn and release the large red power button to enable power to the PNG. The GREEN LED will light up indicating that the electronics are powered-up and the YELLOW LED will light up indicating the PNG interlocks are all satisfied. The main AC/DC power button will power up the PNG when twisted ¼ turn clockwise and will turn off power to the PNG when depressed.
- b. Insert the bronze key into the key switch and turn the key ¼ turn clockwise. This will energize the PNG putting it into a state where it is ready to produce neutrons. Turn the key back ¼ turn counter-clockwise to disable the system. **Exercise caution as the PNG could produce neutrons with a single command from the PNG software GUI if the HVPS disable box interlock button is not pushed down. It is recommended that the key is in the disable position while personnel are setting-up. If the RED LED is illuminated, than the PNG is most likely making neutrons and no personnel should be near the PNG. If you are near the PNG and the red LED illuminates, immediately push down the large red button to turn off power to the PNG.**

Pulsed Neutron Generator Setup

- 1) Open the PNG Graphical User Interface (GUI)
 - a. Start the GUI by double clicking on the DNCII icon located on the Windows 'Start' tab or the DNCII short cut on the Desktop. If you are having problems finding the DNCII.exe program it should be located on the installation directory C:\DNCII on the computer. At this point the main interface screen, shown in Figure 9, should be displayed.

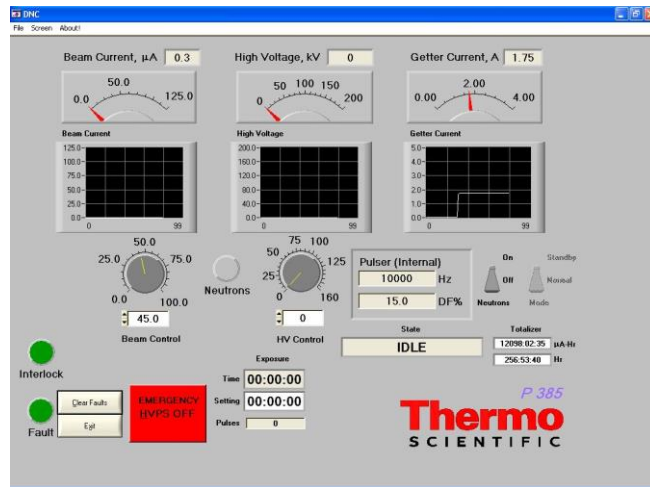


Figure 9. PNG Main GUI Display

- b. The system should be in a fault state, since the HVPS disable box red interlock button is pushed down. Click on 'Fault Analysis' on the 'Screen' pull-down menu tab to view the current system faults.

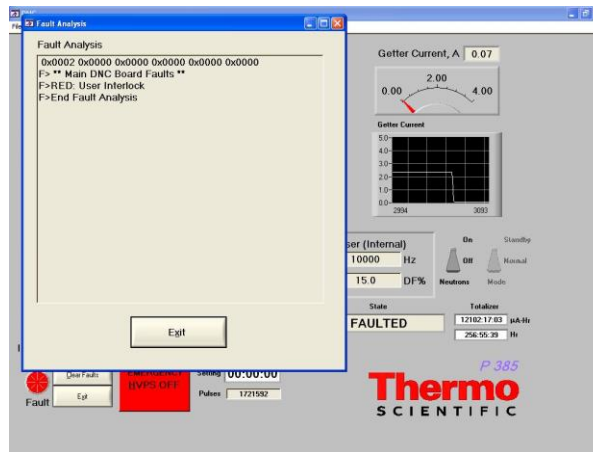


Figure 10. Fault Analysis Window

A window will pop up showing system faults. The example in Figure 10 shows a fault indicating that the user interlock is in the open state (the HVPS disable box red button is pressed down). First, insure that all personnel are clear from PNG and outside of the 250 foot radius radiation keep-out zone. Then, twist and release the red button and click on the 'Clear Faults' button on the GUI interface. This will bring the PNG system into the 'IDLE' state shown in the 'State' display box on the Main GUI interface.

2) Set the Beam Current and High Voltage

- a. Enter in your beam current (mA) and high voltage (kV) settings for the PNG by typing their values into the boxes labeled 'Beam Control' and 'HV Control' on the main GUI interface.

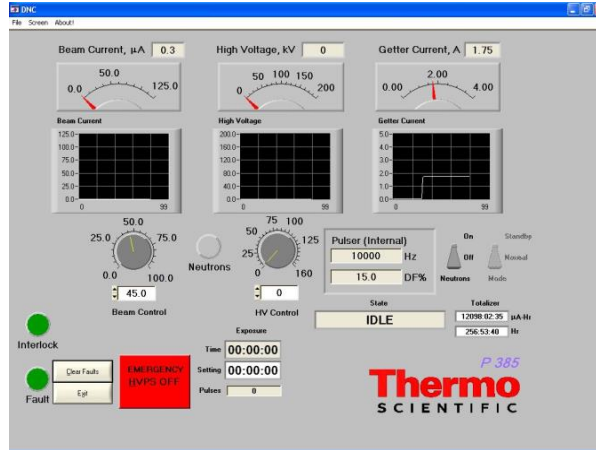


Figure 11. PNG Main GUI Display

- b. The 'Beam Current, mA', 'High Voltage kV', and 'Getter Current, A' status boxes along the top of the main GUI interface will display the current values for the PNG when it is 'Off' or 'On' and producing neutrons.

3) Setup the Pulser

- a. Click on 'Pulser Setup' on the 'Screen' pull-down menu tab and the 'Pulser Setup' window will pop. Enter in the PNG settings for frequency and duty cycle into the boxes for your experiment. Additional options are available in this window including configuring the PNG pulse timing and selecting an external pulse source.
- b. Figure 11 shows an example of the 'Pulser Setup' window with the two buttons that allow you to save the setup "greyed out" and not available. You must first click on the 'File' tab, enter the "TMFP" password, and press the 'Enter' button on your key board to configure the pulse options to prevent the system from being accidentally changed. This will also allow you to set the Pls 1 Delay and Width, and the Pls 2 Delay and Width for the logic pulses from SOURCE and Pulse Delay 1 connectors on the PNG electronics enclosure that you will use when taking PHA coincidence data acquisitions with Lynx.

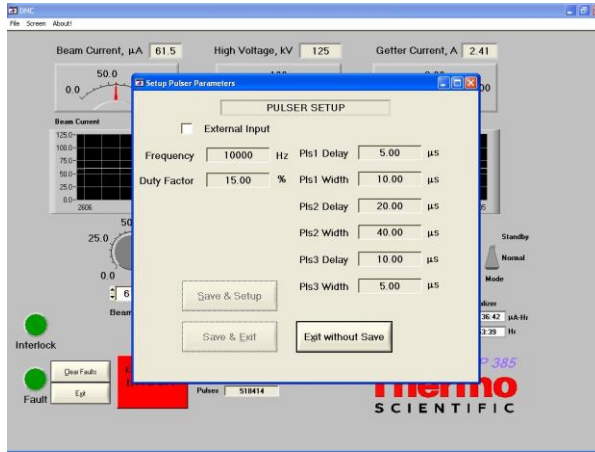


Figure 11. Pulser Setup Window

- 4) Start the PNG
 - a. Toggle the 'Neutron' labeled software switch from the OFF position to the ON position.
 - b. In the ON position, the system will turn on the Lamp, apply the high voltage and bring up the beam current by applying more current to the reservoir.
 - c. You can monitor the progress of the PNG startup by looking at the beam current, high voltage, and getter current values in their current value display boxes and their graphs on the main GUI display. The startup should look like the screen shot in Figure 12.

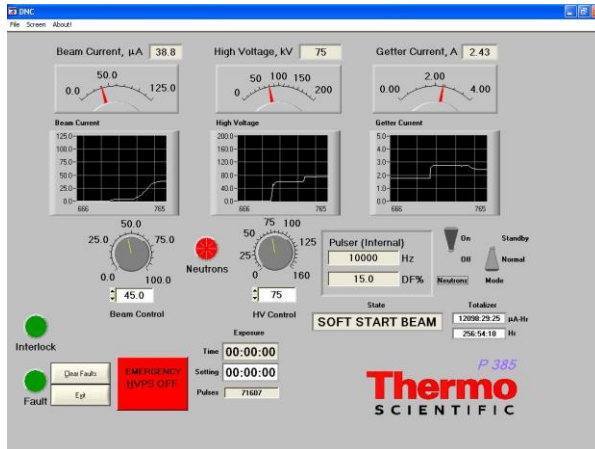


Figure 12. Startup on the Main GUI Display

5) Standby the PNG

- a. Toggle the 'Mode' labeled software switch from the NORMAL position to the STANDBY position.

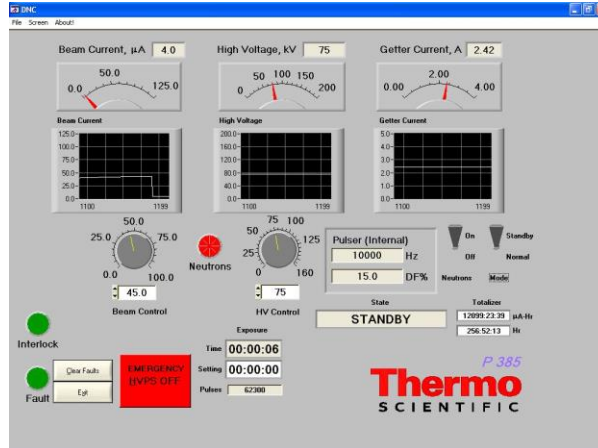


Figure 13. Standby Mode Screenshot

- b. You will want to use the Standby mode when a rapid re-start is required, since it allows you to stop neutron production for short periods of time. The HV will remain at the value that you configured and the reservoir current will stay at the value necessary to maintain your configured beam current. There will be an indication of a small amount of beam current on the main GUI display (inherent in the HVPS measurement circuit), but this is not an indication of target current. The bleed off current is ~1mA for every 20kV of HV. The system will maintain the standby state for up to 15 minutes and then go back to the idle state. The PNG must be producing neutrons to allow you to enter standby.
- c. To exit standby mode and return run mode, toggle the 'Mode' switch from the STANDBY position to the NORMAL position.

USE CAUTION: Although the PNG is not producing neutrons in Standby mode, HV is still applied and the tube has sufficient pressure to make neutrons as soon as the ion voltage is applied. It is not recommended to use this setting for activities that would put personnel in close proximity to the PNG. The system can resume neutron production immediately upon exiting the standby state and returning to the idle state by simply toggling the 'Neutron' switch from the OFF position to the ON position on the main GUI display.

6) Stop the PNG

- a. To stop neutron production and fully turn off the PNG, Toggle the 'Neutron' labeled software switch from the ON position to the OFF position.
- b. Stop the PNG when before you make changes to the PNG settings, when personnel is in close proximity to the PNG or when you are done with your experiments. Wait approximately 20-30 minutes before going out to the granite or basalt monument with a gamma ray detector to avoid exposure to a high flux of delayed gamma rays from the monument.

NOTE: For additional information please consult the Thermo Scientific MP320 PNG Manuals.